Review

Structures of Impurity Defects in Lithium Niobate and Tantalate Derived from Electron Paramagnetic and Electron Nuclear Double Resonance Data

Valentin G. Grachev *[ID] and Galina I. Malovichko *

Physics Department, Montana State University, Bozeman, MT 59717, USA
*   Correspondence: valentin.g.grachev@gmail.com (V.G.G.); galina.i.malovichko@gmail.com (G.I.M.)

Abstract: Point intrinsic and extrinsic defects, especially paramagnetic ions of transition metals and rare-earth elements, have essential influence on properties of lithium niobate, LN and tantalate, LT, and often determine their suitability for numerous applications. Discussions about structures of the defects in LN/LT have lasted for decades. Many experimental methods facilitate progress in determining the structures of impurity centers. This paper gives current bird's eye view on contributions of Electron Paramagnetic Resonance (EPR), and Electron Nuclear Double Resonance (ENDOR) studies to the determination of impurity defect structures in LN and LT crystals for a broad audience of researchers and students. Symmetry and charge compensation considerations restrict a number of possible structures. Comparison of measured angular dependences of ENDOR frequencies with calculated ones for Li and Nb substitution using dipole–dipole approximation allows unambiguously to determine the exact location of paramagnetic impurities. Models with two lithium vacancies explain angular dependencies of EPR spectra for Me^{3+} ions substituting for Li^+ like Cr, Er, Fe, Gd, Nd, and Yb. Self-compensation of excessive charges through equalization of concentrations of $Me^{3+}(Li^+)$ and $Me^{3+}(Nb^{5+})$ and appearance of interstitial Li^+ in the structural vacancy near $Me^{3+}(Nb^{5+})$ take place in stoichiometric LN/LT due to lack of intrinsic defects.

1. Introduction

Point intrinsic and extrinsic defects, especially paramagnetic ions of transition metals and rare-earth elements, belong to the most important defects in lithium niobate (LN, $LiNbO_3$) and tantalate (LT, $LiTaO_3$), because of their essential influence on properties of this material, such as domain structure, electro-optical coefficients, light absorption, refractive indices, birth and evolution of wave-front dislocations ([1,2] and references there), and their consequences for present and potential applications [3–7]. A lot of effort was spent to establish a correlation between the observable data and the crystal composition, and to develop experimentally supported models of the defects: ion charges, identities, and position of the ions in the lattice, their nearest surroundings, ways of charge compensation and recharge mechanisms. Discussions about structures of intrinsic and extrinsic defects in LN/LT have lasted for decades [1]. With time, the proposed structures were evolved and detailed. Some early models were rejected. For instance, after a supposition that effective net charges are about 2.0+ [8], or 1.59+ for Nb and 1.21+ for Ta [9], it was natural to assume that divalent and trivalent impurities should preferably substitute for Nb, but not for Li. Later, numerous investigations have shown that the real picture is more complicated and richer.

In the course of the investigation of defect structures in LN/LT the following difficulties take place:

- high quality conventional samples with crystal composition x_C are usually grown from the congruent melt with the composition $x_m \approx 48.4\%$, for LN and $x_m \approx 48.7\%$ for LT (x = [Li]/([Li] + [Nb/Ta]); this means that the congruent crystals with $x_m = x_C$ contain many intrinsic (non-stoichiometric) defects, causing a broadening of the observable spectral lines and ambiguities in their interpretation;
- the crystal composition x_C of the undoped samples depends on both melt composition and growth conditions;
- the most probable positions for impurity incorporation, the Li and Nb sites as well as the octahedral structural vacancy, have the same local symmetry $\mathbf{C}_3$; this means that they are not distinguishable by many spectroscopic techniques.

Techniques for the defect study can be conditionally divided into two groups: direct (Mössbauer spectroscopy [10], Rutherford Backscattering Spectrometry (RBS) [11], Extended X-ray Absorption Fine Structure Analysis (EXAFS), Particle Induced X-ray Emission (PIXE) combined with channeling, X-ray standing wave (XSW) [12], Electron Paramagnetic Resonance (EPR), and Electron Nuclear Double Resonance (ENDOR) [13]) and indirect (optical absorption and luminescence, measurements of electro-optical coefficients, etc.).

Attempts to determine impurity positions by indirect methods often gave contradicting information. Direct methods also have some shortcomings. For instance,

- Mössbauer spectroscopy demands the presence of special nuclei,
- channeling investigations are more successful in the case of heavy, many-electron ions,
- channeling methods are not sensitive to the charge state of the impurity and do not distinguish centers with $\mathbf{C}_3$ and $\mathbf{C}_1$ symmetry,
- due to the relatively low sensitivity the EXAFS needs high levels of crystal dopants (about 3–5 mol.%), for which clustering and occupation of both Li and Nb positions become very probable,
- EPR/ENDOR techniques are applicable to systems with non-zero spins only.

Investigations of impurity defects were carried out by all direct and indirect techniques in parallel and together, and made invaluable contributions to the problem solution. Let's mention briefly a few of them. The positions of many impurity ions were determined by the EXAFS, PIXE, XSW, and channeling methods. Lithium substitution was found for most elements including Sc, Ti, Mn, Ni, In, Pr, Gd, Ho, Er, Tm, Yb, Lu ([11,14–18], and references there), Nd [19,20], Co, Fe [21–28]. A few ions substitute for Nb in LN (Hf [29], Er [30]) and in LN heavily co-doped by Mg or Zn (Sc, In, Nd, Lu [31]). Some of the ions can occupy both positions (Cr [32], Gd, Nd). Mössbauer spectroscopy [33,34] gave indirect evidence of Fe^{2+} and Fe^{3+} substitution for Li^+. Raman spectroscopy data [35] were interpreted on the base of Fe substitution for Li. Magneto-optical and luminescence studies [36,37] identified non-paramagnetic pairs Cr_{Li}-Cr_{Nb} and established a correlation between optical bands and Cr^{3+} positions.

Convincing arguments of Fe^{3+} substitution for Li^+ were obtained by ENDOR [38–40]: it was shown that spectrum angular dependencies calculated on the base of dipole-dipole interactions of Fe^{3+} electrons with surrounding Li nuclei are qualitatively different for Li and Nb substitution; quantitative agreement calculated and experimental data was achieved for Li substitution.

The huge amount of nonstoichiometric intrinsic defects in congruent LN/LT grown by the conventional Czochralski method [41,42] (we shall call them cLN and cLT) has often undesirable effects on crystal properties. Several techniques were invented in order to reduce the concentration of these defects. Some decrease of their concentration was achieved by using melts with Li excess (with x_m up to 60%) [43,44]. Thin LN/LT samples were enriched with Li by vapor transport equilibrium treatment (VTE [45–50], we shall call them vLN and vLT). Using double crucible growth [51–55] with excess of Li allowed one to obtain nearly stoichiometric samples (nsLN). Crystals grown by the Czochralski method from a melt to which potassium oxide K_2O has been added ([56–67], and references there) have composition $x_C \approx 50\%$ (LN_K, stoichiometric LN, sLN). The method is scientifically called the High Temperature Top Seeded Solution Growth (HTTSSG).

The defect elimination in sLN crystals has led to a tremendous narrowing of the resonance lines and a corresponding increase of spectral resolution, and resulted in improved precision of obtained spectroscopic characteristics. Discovery of new centers substituting for Nb (or Ta in LiTaO$_3$) and a change of charge compensation mechanism in sLN was accompanied by a significant progress in understanding the nature and structures of intrinsic and extrinsic defects [68–76]. Several methods of determination of real crystal composition were developed [68,77–80]. It should be mentioned that even crystals with x_C = 50% are not completely free of intrinsic defects. There is a class of intrinsic defects which break the regular order of the LN lattice without a change of x_C: the permutations Nb$_{Li}$ and Li$_{Nb}$, and cyclical permutation of Nb in Li site, Li in structural vacancy, and vacancy of Nb. Such defects can cause broadening of spectral lines.

EPR is resonance absorption of microwave quanta by electron spins placed in a swept external magnetic field at definite value of magnetic field B_{res}. Depending on measurement conditions it has usual sensitivity about 10^{12}–10^{15} spins/cm^3 or higher. Equipment with wave lengths 3cm (X-band, microwave frequency $\nu \approx 9.5$ GHz) and 8 mm (Q-band, $\nu \approx 34$ GHz) are usually used. EPR lines have typical widths about 1–100 MHz. This defines the resolution ability of the EPR.

Nuclear magnetic resonance (NMR) is resonance absorption of radiofrequency quanta by nuclear spins. It has worse sensitivity due to thousand time smaller magnetic moments of nuclei. However, NMR has significantly higher resolution ability about 1–100 KHz or less. Only nuclei with large natural abundance of magnetic isotopes (like ^{7}Li—92.5%, ^{93}Nb—100%, ^{181}Ta—99.99%) can be studied by NMR. Due to interactions with electron spins, nuclei in the impurity neighborhood have energy levels and resonance frequencies different from those of bulk nuclei. As their concentrations, which are about impurity concentration, are significantly smaller than concentrations of bulk nuclei, their NMR signals are too weak to be registered directly.

ENDOR is the indirect way to register NMR of nuclei in impurity surrounding via a stimulated change of intensity of the EPR signal in magnetic field B_{res}. ENDOR has sensitivity that is worse than EPR (about one-two orders of magnitude), but is better than NMR. Its resolution is comparable with NMR resolution. Characteristics of all nuclei (natural abundance of isotopes, their nuclear spins, magnetic and quadrupole moments) are well known and tabulated. This allows to relate observed ENDOR frequencies to interactions of impurity electrons with own nucleus and surrounding nuclei.

For a paramagnetic impurity these techniques are capable of determining: its element, charge, spin state, nearest surrounding (i.e., its location), and many spectroscopic characteristics. Fortunately, most impurities which are useful for optoelectronic application (including transition and rare-earth elements) enter LN and LT in a paramagnetic state. Li, Nb and Ta nuclei have significant (93–100%) natural abundance of magnetic isotopes. The main isotope ^{16}O has no magnetic moment and is invisible in EPR/ENDOR/NMR experiments.

The aim of this paper is to give current bird's eye view on contributions of EPR/ENDOR studies to the determination of impurity defect structures in LN and LT crystals for a broad audience of researchers and students. The name "center" will be used for a complex consisting of the paramagnetic impurity and its surrounding that can have zero, one or more defects besides regular ions.

2. Materials and Methods

Most of our measurements presented below were carried out on samples grown by E.P.Kokanyan from Li-rich melt or from the melt with the addition of K$_2$O [56,57].

The EPR/ENDOR spectra were measured at microwave frequencies $v \approx 9.4$ GHz (X-band) and $v \approx 34.4$ GHz (Q-band) on the Bruker ELEXSYS EPR/ENDOR spectrometer at temperatures between 4.2 and 300 K at Montana State University (Bozeman, MT, USA).

The treatment and simulation of all spectra and their angular dependencies, as well as the preparation of corresponding figures were carried out with the help of the "Visual EPR" and "Visual ENDOR" program packages [81].

All lattice images were generated using CrystalMaker®program [82] and crystallographic data [83–86]. Sizes of oxygen balls were artificially reduced, since nonmagnetic O^{2-} ions are invisible for EPR/ENDOR. As $LiNbO_3$ and $LiTaO_3$ are isostructural crystals, all figures with lattice and structures of impurity centers are equally applicable to both LN and LT. However, dipole-dipole interactions should be calculated taking into account a difference of their lattice constants.

3. Basics of EPR and ENDOR Spectra Interpretation

3.1. Symmetry Considerations

The ideal lattice of LN and LT crystals (Figure 1, see also [87]) has two molecules in its rhombohedral elementary unit cell and the space group symmetry is R3c (C_{3v}^6, 3m) at room temperature [8,88–90]. If ionic radii are taken into account, the LT/LN lattices look like consisting mainly of planar layers of closely packed oxygen ions with small voids between them, filled by Li and Nb/Ta. There are several electrically non-equivalent positions in the lattice. Some of them—the sites on the **z** (or optical **c**) axis of the crystal, including the sites of Li, Nb/Ta and the octahedral structural void (vacancy), v_{oct}—have the symmetry of the point group C_3. An isolated defect in any of these positions creates a C_3 (in the following also labeled "axial") center. The tetrahedral structural void, oxygen sites and all other off axis positions have the lowest possible symmetry, C_1.

A complex of two defects has C_3 symmetry, if both are located on the crystal **z** axis, and C_1 symmetry in all other cases. If the difference in positions of the nearest oxygen ions is ignored, then each unit cell has the following site sequence along the **z**-axis: Li, Ta, v_{oct}, Li, Ta, v_{oct}. However, oxygen octahedrons and next neighbors for two positions of one type cation are not identical, therefore, the correct assignment of the sequence should be Li_L, Ta_L, $v_{oct,L}$, Li_R, Ta_R, $v_{oct,R}$. The surrounding of the "Right" (R) position can be transformed to the "Left" (L) one by a reflection $x \Leftrightarrow -x$ and a shift by c/2, because **zy** is a glide mirror plane in the R3c lattice (Figure 1b). The same consideration is applicable to C_1 positions also. This means that each axial (C_3) or low-symmetry (C_1) L center has a corresponding R partner. The L and R partners are electrically identical and are not distinguishable by optical or channeling methods, but they are magnetically non-equivalent and can be resolved from each other in favorable cases (high spin value, small line width) by magnetic resonance techniques.

Each C_1 center in the R3c lattice has two additional magnetically nonequivalent partners, which can be transformed into each other by a rotation around the **z**-axis of the crystal by 120° and 240°. They can be distinguished by the EPR at arbitrary orientations of the magnetic field.

As any crystal characteristic, the EPR spectra must reflect the crystal symmetry and symmetry of all present paramagnetic centers. The best way to determine the defect symmetry is to study angular dependence of the spectra in external magnetic field **B** under rotation of the crystal sample around **z**-axis (shortly speaking, in **xy** plane). For a C_3 paramagnetic defect with electron spin $S = 1/2$ the EPR spectrum consists of one resonance at the same position B_{res} at any orientation of **B** with respect to crystallographic axes. A set of up to six lines can be observed at arbitrary orientation of **B** for C_1 centers; however, some of them coincide for directions of **B** along **x**, **y**, or **z**. If two or more centers present in the sample studied, the spectrum has two or more sets of the lines. If a center has electron spin $S > 1/2$ multiplets of 2S lines can be observed for every center.
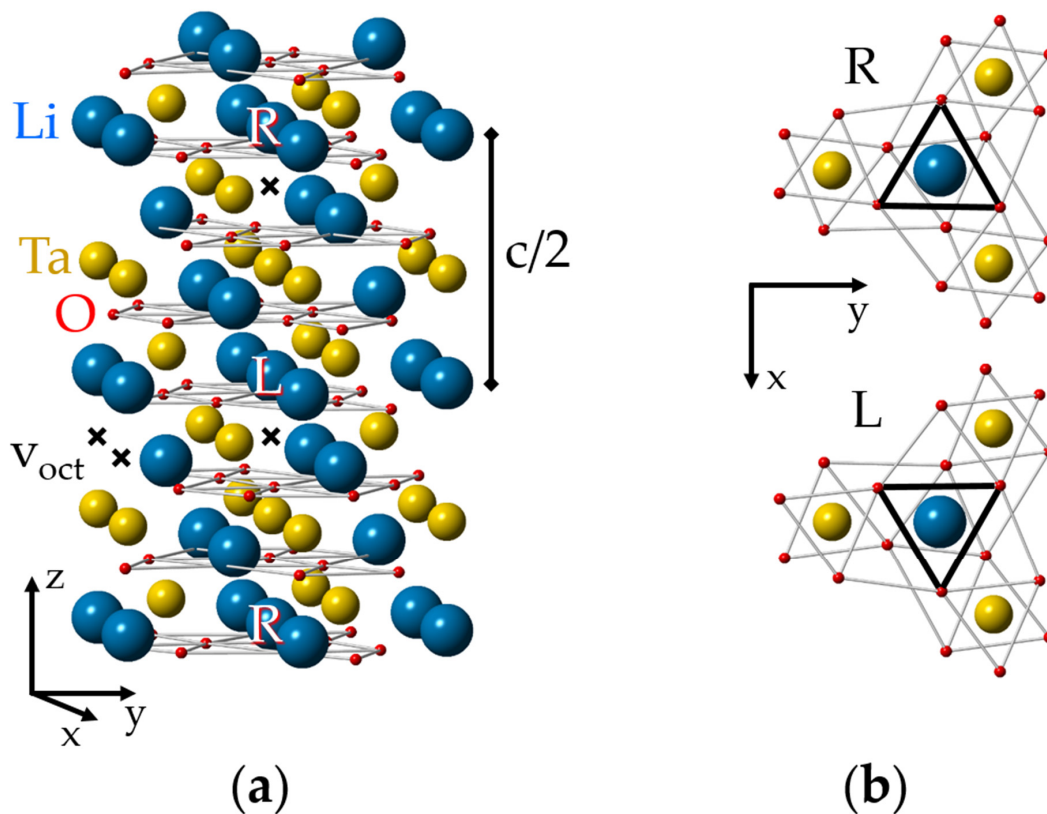
Figure 1. (**a**) Ideal lattice of lithium tantalite (LT). To simplify the representation of the lattice and defect structures in it, the sizes of "balls" imitating ions were made intentionally different. The L (Left) and R (Right) positions are distinguished by their different oxygen surroundings. (**b**) An illustration of local C_3 symmetry for the nearest surroundings of cation sites and glide mirror **zy** plane that transforms the L center to the R partner; a projection of one Li, Ta layer between two oxygen layers on the **xy** plane is shown.

For centers with $S = 1/2$ the resonance line positions can be described using spin-Hamiltonian

$$H = \mu_B \mathbf{B} \mathbf{g} \mathbf{S} \tag{1}$$

Here μ_B is the Bohr magneton, **B** is the vector of static magnetic field, **g** is the tensor of spectroscopic splitting, and **S** is the vector of electron spin.

As an example of the multi-center spectra let's consider ion Nd^{3+} in LN [91–93] (Figure 2). Every spectrum consists of a single dominant line labeled with the number 1 and many satellite lines of smaller intensities. The positions of the dominant line have the same value of the resonance field for **B**||**x** and **B**||**y** ($\varphi = 90$ deg), whereas positions of other lines do not coincide. We have to suppose that the single line #1 belongs to the axial C_3 symmetry center, Nd_1.

To make correct labeling of all observed lines a detailed study of angular dependence of EPR line positions is required. For instance, we can rotate magnetic field in **xy** crystallographic plane, changing azimuthal angle φ between **x**-axis and **B**. Circular diagram of measured spectra (Figure 3) show that dominant line draw a circle, i.e., has no dependence of $B_{res}(1)$ on φ. Angular patterns of other lines demonstrate the presence of all elements of the 3m group, namely, C_3 symmetry and the mirror with respect to **y**-axis at $\varphi = 90$ deg. Measurement of such a diagram is redundant, since **xy** plane angular patterns simply repeat themselves with a period 60 deg. Due to the glide mirror plane, the 30 degree dependence measured from **x** axis contains all information.

Usually, 90 deg of the measured dependence is plotted (Figure 4). If spectra are measured with small angular steps (said 1 deg), it is easy to trace every line. The line tracing allows to put labels on every resonance line on Figure 2. Without doubt, at least four groups of angular branches are clearly distinguished on Figure 4: one straight branch of axial Nd_1 and three sets of curved branches, which correspond to low-symmetry centers Nd_2, Nd_3, and Nd_4. Therefore, we can conclude that Nd^{3+} in Nd_1 center occupies one of three possible positions on the **z**-axis. If Nd^{3+} has additional defect or defects (charge compensators) in its neighborhood, the defect is located on the same axis. In the case of Nd_2, Nd_3, and Nd_4 centers with the C_1 symmetry, the additional defects are located off the **z**-axis. It is unlikely that Nd^{3+} ions occupy sites with C_1 symmetry (tetrahedral void or O^{2-}) due to large charge misfit.
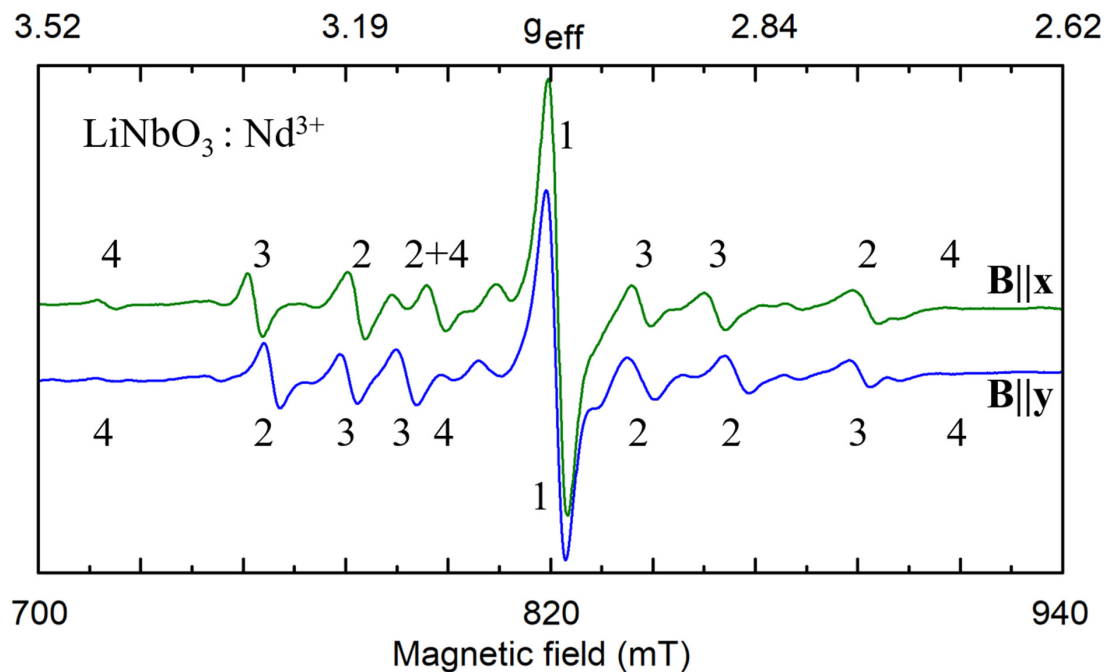

Figure 2. Fragments of electron paramagnetic resonance (EPR) spectra of Nd^{3+} impurity ions in nearly stoichiometric lithium niobate (LN) for microwave frequency ν = 34.445 GHz, T = 19 K. The numbers 1–4 correspond to four different electrically non-equivalent defects. Lines of magnetically nonequivalent partners have the same number.

Symmetry of any center reflects the symmetry of lattice sites occupied by impurity and charge compensators (if any) and their relative locations. To distinguish the C_3 and C_1 symmetries the measurement of angular dependence in **xy** plane is sufficient. However, to obtain a full set of spectroscopic characteristics of the center (like six components of **g**-tensor) by fitting measured angular dependence a study of spectra under three rotations in perpendicular planes (road map) is required.
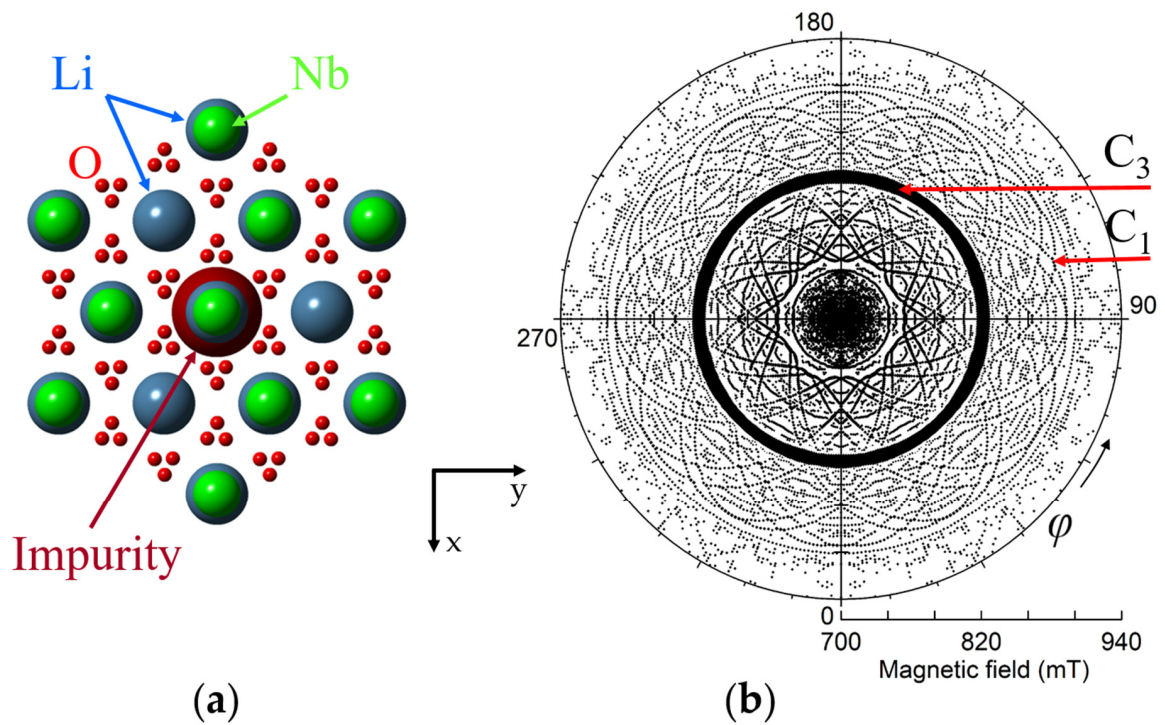
Figure 3. (**a**) Projection of ideal lithium niobate lattice with Nd^{3+} impurity ion on **xy** plane (artificial sizes of balls are used). (**b**) Circular diagram of measured angular dependence of electron paramagnetic resonance (EPR) lines of Nd^{3+} ions in Figure 3. Magnetic field was rotated in **xy** plane from 0 to 360 deg. $\nu = 34.445$ GHz, $T = 19$ K. Symbol sizes reflect line intensities.
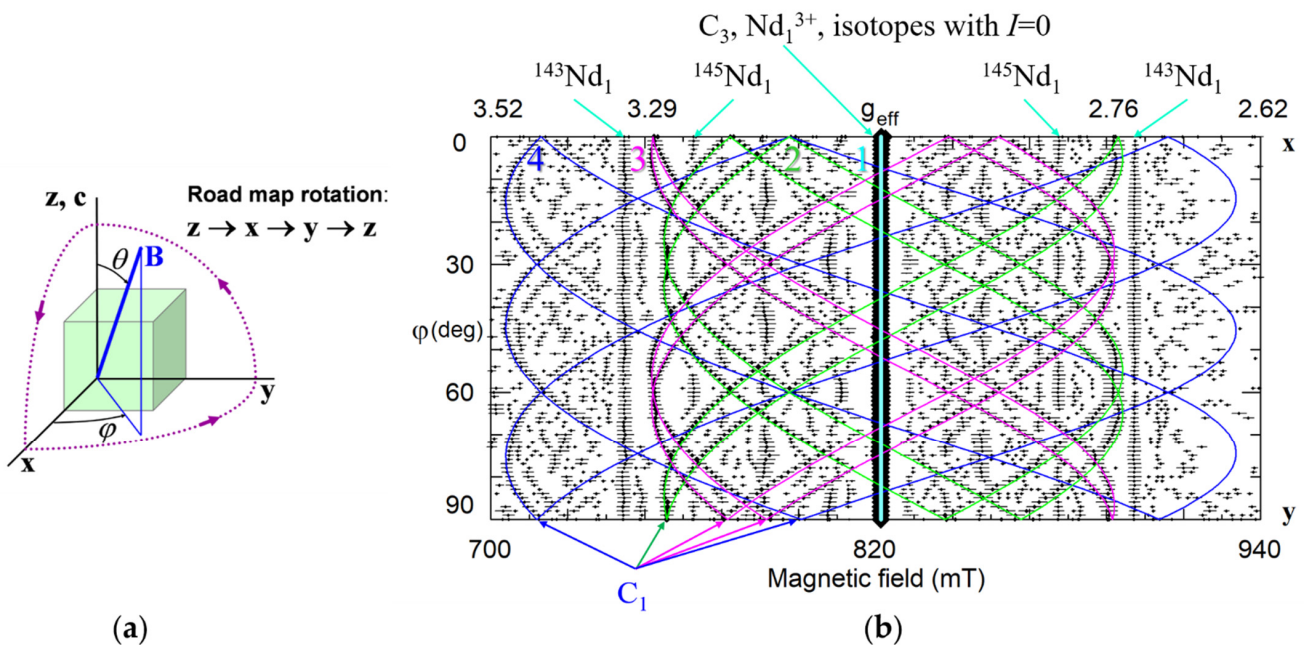
Figure 4. (**a**) The road map rotation corresponds to the following changes of the θ, ϕ angles: $\theta = 0$–$90°$ at $\phi = 0°$; $\theta = 90°$, $\phi = 0$–$90°$; $\theta = 0$–$90°$ at $\phi = 90°$. (**b**) Angular dependence of the EPR spectra in **xy** plane for nearly stoichiometric LN:Nd^{3+}. Rhombs represent experimental line positions for Q-band measurements ($\nu = 34.445$ GHz), their sizes reflect line intensities. Horizontal whiskers near rhombs represent line widths. Cyan, lime, fuchsia, and blue curves represent simulated dependencies for axial Nd_1, and low-symmetry Nd_2, Nd_3, and Nd_4 centers, respectively. Curves for isotopes with nuclear spin $I \neq 0$ are not shown.

3.2. Isotropic and Dipole-Dipole Interactions

Calculations of the ENDOR frequencies and transition probabilities (i.e., ENDOR line positions and relative intensities) for *i*-th nucleus is usually based on nuclear spin-Hamiltonians H_i

$$H_i = -\mu_n g_n^{(i)} \mathbf{B} \mathbf{I}^{(i)} + \mathbf{S} \mathbf{A}^{(i)} \mathbf{I}^{(i)} + \mathbf{I}^{(i)} \mathbf{Q}^{(i)} \mathbf{I}^{(i)} \tag{2}$$

where μ_n—nuclear magneton, $g_n^{(i)}$—nuclear g-factor; $\mathbf{A}^{(i)}$, $\mathbf{Q}^{(i)}$—tensors of hyperfine and quadrupole interactions.

In many cases there are two dominant contributions to the hyperfine tensor $\mathbf{A}^{(i)}$: isotropic (contact) hyperfine interaction, $a^{(i)} \mathbf{S} \mathbf{I}^{(i)}$ and dipole-dipole interaction of vectors of electron $\mu_B g \mathbf{S}$ and nuclear $-\mu_n g_n^{(i)} \mathbf{I}^{(i)}$ magnetic moments. The dipole–dipole interaction can be described by

$$A_{jm}^{(i)dd} = \frac{\mu_B \mu_n}{\left(R^{(i)}\right)^3} g_n^{(i)} \left[\frac{3}{\left(R^{(i)}\right)^2} \left(\sum_{p=x,y,z} g_{jp} R_p^{(i)} \right) \left(\sum_{l=x,y,z} R_l^{(i)} \delta_{lm} \right) - g_{jm} \right] \tag{3}$$

where $\mathbf{R}^{(i)}$ is the vector from paramagnetic impurity to the *i*-th nucleus. Most characteristics in Equation (3) are known: μ_B, μ_n, $g_n^{(i)}$ are tabulated, g_{jm} components of **g**-tensor are determined from EPR measurements. Therefore, comparison of measured angular dependences of ENDOR frequencies with calculated ones on the base of Equations (2) and (3) can be used for determination of $\mathbf{R}^{(i)}$, i.e., the position of the paramagnetic impurity relative to surrounding nuclei.

Nuclei at the same distance from impurity ions are usually called a shell. The first shell of an impurity in a Li site has six nearest Li nuclei off the **z**-axis at the distance $R^{(1)}$ (Figure 5a). Three of them are located above the impurity (the subshell 1a), other three—below the impurity (the sub-shell 1b); if the impurity is shifted from regular Li site then $R^{(1a)} \neq R^{(1b)}$. The second shell consist of six Li nuclei in the **xy** plane of the impurity at the distance $R^{(2)}$ (subshells 2a, 2b).The first shell of an impurity in a Nb site has one Li nucleus on **z**-axis, the second shell has three Li nuclei (the nuclei are labelled 1 and 2 on Figure 5b). As directions from the impurity to the nuclei in a shell are different, their hyperfine interactions are magnetically non-equivalent, i.e., produce different branches in angular dependences of ENDOR spectra.
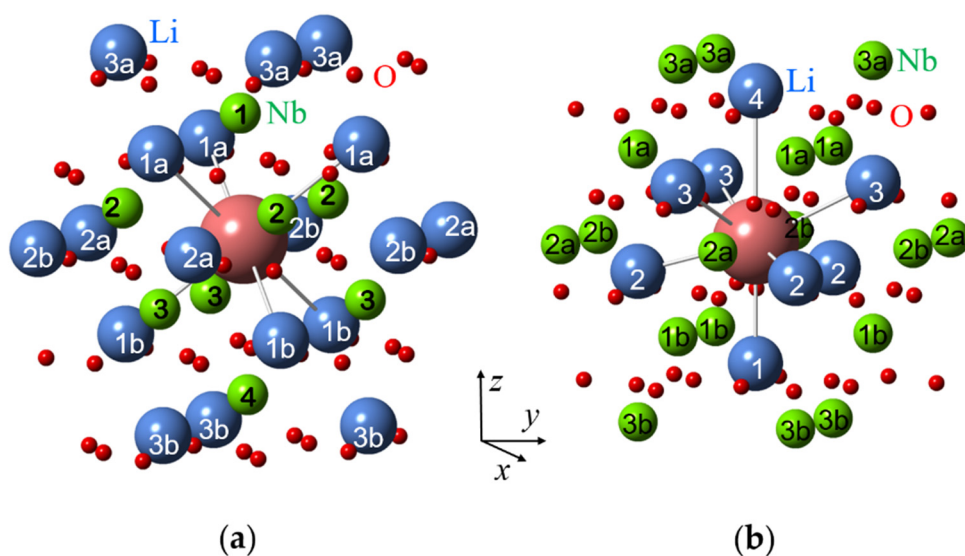

Figure 5. Surroundings of impurity ions substituted for Li (**a**) and Nb (**b**) in LN crystal lattice with corresponding shell numbers. Large blue balls represent Li$^+$ ions, medium green balls—Nb^{5+} ions, small red balls—O^{2-} ions, and the largest magenta ball—the impurity ion.

The simplest way to determine the impurity lattice site is:

- to calculate $A_{jm}^{(i)dd}$ for the several nearest nuclei around the impurity taking lattice distances from X-ray data and g_{jm} from EPR measurements,
- to calculate ENDOR frequencies, to plot patterns of their angular dependencies, and
- to compare the patterns with measured angular dependencies of ENDOR for a definite EPR line [13,38,39].

Due to different surroundings for impurities in the Li and Nb sites, the calculated patterns are completely different (Figure 6). ENDOR frequencies for the first shell of Li nuclei for the Li site vary with rotation of magnetic field in **xy** plane(Figure 6a), whereas for the single Li nucleus of the first shell for Nb site two straight branches should be observed in angular dependence (Figure 6c). As Li nuclei of the all corresponding shells are closer to the impurity ion in the Nb site than in the Li site, the range of angular variation for Nb site is larger than for Li site. The branches of the 2nd and 3rd shells for Li site practically coincide with measured angular dependencies for Nd_1 center (Figure 6b), whereas no branch for Nb site is close to observed one. The branches of the 1st shell for Li substitution also agree with observed ones after small correction due to isotropic hyperfine interaction (Figure 6b). Based on clear agreement of hundred measured values of ENDOR frequencies for the dominant EPR line #1 with calculated frequencies for Li site and obvious disagreement with calculated ones for Nb site, we can definitely conclude that the Nd_1 line in EPR spectra (Figure 2) belongs to Nd^{3+} ion substituted for Li.
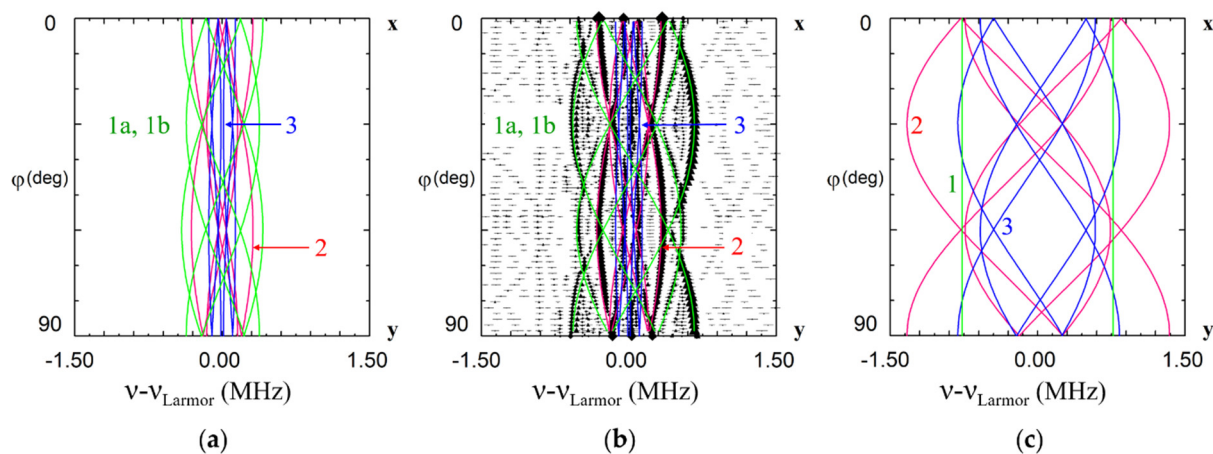
Figure 6. Angular dependence of electron nuclear double resistance (ENDOR) frequencies of Li nuclei in **xy** plane for the $Nd_1{}^{3+}$ center in $LiNbO_3$. The green, red and blue curves—calculated frequencies for Li nuclei of the 1st, 2nd and 3rd shells based on dipole-dipole interaction for $Nd^{3+}{}_{Li}$ (**a**,**b**), and $Nd^{3+}{}_{Nb}$ (**c**). ENDOR frequencies represented on the part (**b**) were measured at magnetic fields corresponding to the position of dominant EPR line #1 on Figure 2 ($B = 820$ mT for $\nu = 34.445$ GHz, rhombs, and $B = 228$ mT for $\nu = 9.500$ GHz, triangles). ν_{Larmor} is Larmor frequency of ^{7}Li nuclei.

The simulation of dipole-dipole interactions for the Li and Nb sites has no fitting parameter. Therefore, the described qualitative and quantitative approach for the determination of impurity positions gives reliable results. Note that hyperfine interactions for Nb/Ta nuclei have additional contributions due to a polarization of inner electron shells of oxygen and niobium ions (transferred hyperfine interaction).

The characteristic of isotropic hyperfine interaction $a^{(i)}$ is related to a density of electron cloud at the location of i-nucleus $\mathbf{R}^{(i)}$. For the isotropic g-factor:

$$a^{(i)} \; = \; \frac{8\pi}{3} g \mu_B g_n^{(i)} \mu_n \left| \psi\left(\mathbf{R}^{(i)}\right) \right|^2 \tag{4}$$

The isotropic hyperfine interaction often (but not always) exponentially decreases with the distance from impurity. The largest value $a^{(i)}/g_n^{(i)}$ should correspond to nuclei nearest

to the impurity. It allows to determine nuclei of the nearest surrounding by comparison of $a^{(i)}/g_n^{(i)}$ for Li and Nb nuclei, and therefore, to find the impurity location. Impurities substituted for Li have Nb nucleus on **z**-axis in the nearest surrounding, whereas ions substituted for Nb have Li nucleus (Figure 6, shell #1).

Another way to use contact and dipole-dipole interactions is:

- to measure the road map of angular dependencies in three perpendicular planes (Figure 4a),
- to determine all components of $\mathbf{A}^{(i)}$ tensors by fitting observed angular dependencies,
- to separate isotropic and anisotropic parts,
- to find principal values of the anisotropic part, and finally,
- to compare these principal values with calculated ones on the base of Equation (3).

3.3. Charge Compensation and Intrinsic Defects

The structure of a center, in which a lattice site is occupied by an extrinsic impurity ion having a charge different from that of the respective lattice ion (in the following labeled "non-isocharged replacement"), depends on the charge of the impurity and the mechanism of charge compensation. Because of non-stoichiometry, the real lattice of conventional congruent LN contains many intrinsic defects, the relative concentrations of which have not yet been determined reliably. The following entities have been considered (their charges with respect to the lattice being given by Kröger-Vink notation in brackets): $Nb^{5+}_{Li}{}^+$ ($Nb_{Li}{}^{4\bullet}$) antisite defect, $v_{Li}{}^+$ ($v_{Li}{}'$) lithium vacancy, $v_{Nb}{}^{5+}$ ($v_{Nb}{}^{5'}$) niobium vacancy, Nb^{5+}_v ($Nb_v{}^{5\bullet}$) niobium on structural vacancy, Li^+_v ($Li_v{}^\bullet$) lithium on structural vacancy, v_O oxygen vacancy. During recent years the existence of the following charge compensated complexes has been postulated most often: $Nb_{Li} + 4v_{Li}$ [90,94,95] (including three-dimensional complexes $3v_{Li} + Nb_{Li} + v_{Li}$ [96,97]), $5Nb_{Li} + 4v_{Nb}$ [98,99], $2Nb_{Li} + 2Nb_v + 3v_{Li} + 3v_{Nb}$ [96] and some others [100]. Some features accompanying the crystal growth (Li_2O evaporation, variation of oxygen deficiency in Nb_2O_{5-x} [101]) and specific changes of some crystal properties after thermal oxidation and/or reduction definitely indicate that the oxygen sub-lattice is not always perfect and stable as well; therefore the oxygen non-stoichiometry has been also discussed for a long time [102–105]. The intrinsic defects by themselves or complexes of them, which are not charge compensated, can furthermore serve as local or distant charge compensators for non-isocharged extrinsic or radiation defects. Due to the high concentration of the intrinsic defects the congruent LN and LT crystals are very tolerant to substitutional or interstitial impurities, including non-controlled ones, because the necessary charge compensators (local or distant) can be easily found among the non-stoichiometric defects. Real crystals often contain H, Cu, Co, Mn, Fe, etc. in concentrations about 0.00X–0.0X.

Non-isovalent cation Me^{n+} (n > 1) substituted for Li^+ requires negative charge compensator like lithium vacancy or interstitial O^{2-}. If Me^{n+} (n < 5) substituted for Nb^{5+} or Ta^{5+} the n − 5 negative charge can be compensated by antisite ions, oxygen vacancies, v_O or interstitial H^+ and Li^+.

In some cases, a self-compensation of impurity charges takes place. For instance, no additional charge is required if two Me^{3+} ions substitute for both Li^+ and Nb^{5+} in nearest neighbor or next neighbor sites (local self-compensation) or even relatively far one from another (distant self-compensation). There are two critical parameters, which stimulate the self-compensation: total concentration of possible charge compensation defects, [D] and the total concentration of Me^{3+} ions in the sample, [Me]. The [D] includes a dominant contribution due to a deviation of the crystal composition from stoichiometry, concentrations of H^+ ions and v_O, as well as contributions due to non-controlled impurities (Mg, C, Si, Cl, . . .), which are always present in real crystal in concentrations about 1–500 ppm. If [D] >> [Me] the isolated centers with additional intrinsic defects are dominating. If [D] << [Me] then the self-compensation is preferable due to lack of charge compensators.

Distant charge compensators produce small distortions of the crystal field at the impurity site, what normally causes EPR line broadening, and an asymmetry of their

shapes, but do not change the center symmetry revealed in the observed positions and splitting of EPR lines. Defects in the immediate neighborhood (local charge compensation) cause strong changes of the center characteristics (**g** and **A** tensors in the case of Nd^{3+}) and lowering of center symmetry.

3.4. Di-Vacancy Models for Trivalent Impurities

Many impurities in LN/LT crystals create a family of paramagnetic centers that includes dominant axial center and several satellite low-symmetry centers with EPR lines of smaller intensities (like presented on Figure 2). It would be reasonable to look for center models which are able to describe the whole family.

Low-symmetry C_1 centers appear in three cases:

1. Impurity ion like Nd^{3+} has an off-axis lattice defect (charge compensator) in the immediate neighborhood.
2. Impurity ion substitutes for O^{2-} (this is very improbable for cations).
3. Impurity ion incorporates into a small tetrahedral void (this is possible, but often unlikely due to larger charge misfit than for Li substitution).

For axial centers, the directions of principal axes of the **g**-tensor are dictated by crystal symmetry: the 3rd axis of the center coincides with the crystal axis and the directions of the 1st and 2nd axes are arbitrary. For low-symmetry centers, there are no symmetry restrictions on the orientation of principal axes. However, if the symmetry lowering is related to an off-axis lattice defect, it is reasonable to expect that directions of the center axes are related to the distortion created by the off-axis defect. The 3rd axis will have some inclination from the **z**-axis to the defect, and projections of the 1st or 2nd axis will be close to the projection of line from the impurity ion to the defect. The distortion should decrease with the distance from the impurity ion to the defect.

ENDOR data for the dominant EPR line have confirmed that Nd^{3+} substitutes for Li^+ and only Li and Nb nuclei were found in the neighborhood. Therefore, intrinsic defects without nuclear spin should be considered for the required 2-charge compensation. The size O^{2-} is comparatively large to be placed into small octahedral or tetrahedral voids. Nearly stoichiometric crystals have significantly reduced concentration of v_{Li}. Nevertheless, their concentration often exceeds the impurity concentration. Sufficient concentration of v_{Li} can be also created in the process of growth of samples with non-isocharged impurities.

A key to the identification of models which describe all varieties of Nd^{3+} centers with minimal assumptions was obtained from the analysis of angular dependencies of the Nd_4 center. The extrema in the **xy** plane and, correspondingly, projections of one principal axis of the **g**-tensor, are close to ϕ values of 15, 45, and 75 degrees (Figure 4b). In the projection of the LN lattice onto the **xy** plane (Figure 7, after [93]) there are no similar values of ϕ from Nd^{3+} to any ion in the lattice: directions from the Nd^{3+} site to all cation sites have azimuthal angles equal to $n \times 30°$. Therefore, the simplest model, that has a single lattice defect, like a Li^+ vacancy, v_{Li}, cannot explain the observed angular dependencies of Nd_4 centers. However, if two Li^+ vacancies are located in the first and second shells of the surroundings of an Nd^{3+} ion substituted for a Li^+, the three defects are organized into a triangle. The longest side of the triangle connected two v_{Li} has a perpendicular oriented in the required direction (Figure 7).

The hypothesis that Nd^{3+} substituted for Li^+ has two v_{Li} as charge compensators allows for consistent models for the whole family of Nd^{3+} centers in LN crystals with a low concentration of neodymium doping. After analysis of principal values and axes of **g**-tensors it was concluded [92,93] that Nd^{3+} centers have lithium vacancies in sites described in Table 1. Some of possible structures are presented on Figures 7 and 8.

The di-vacancy models can explain EPR spectra of many other (but not all) trivalent impurities $Me^{3+}{}_{Li}$.
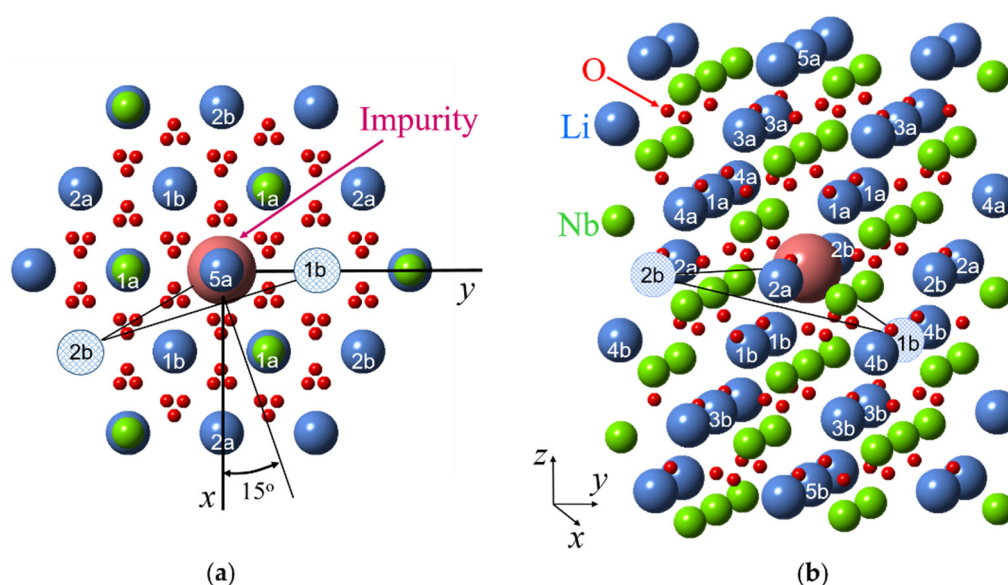
Figure 7. A projection of lithium niobate crystal lattice on **xy** plane (**a**) and 3D model (**b**) with shell numbers for an impurity substituted for Li$^+$ ion (sizes of all ions were artificially changed in order to make clear positions of cation ions). Hatched circles represent two vacancies of Li$^+$ ions for Nd$_4$ center.

Table 1. Sites for lithium vacancies, v_{Li} in the surroundings of Me$^{3+}_{Li}$ centers in LiNbO$_3$.

Center v_{Li} Site	Me$_1$	Me$_2$	Me$_3$	Me$_4$	Me$_5$	Me$_6$	Me$_7$	Me$_8$
First	5a/5b	1a/1b	2a/2b	1a	1b	1a/1b	2a/2b	5a
Second	distant	5a/5b	5b/5b	2a	2b	3a/3b	3a/3b	5b
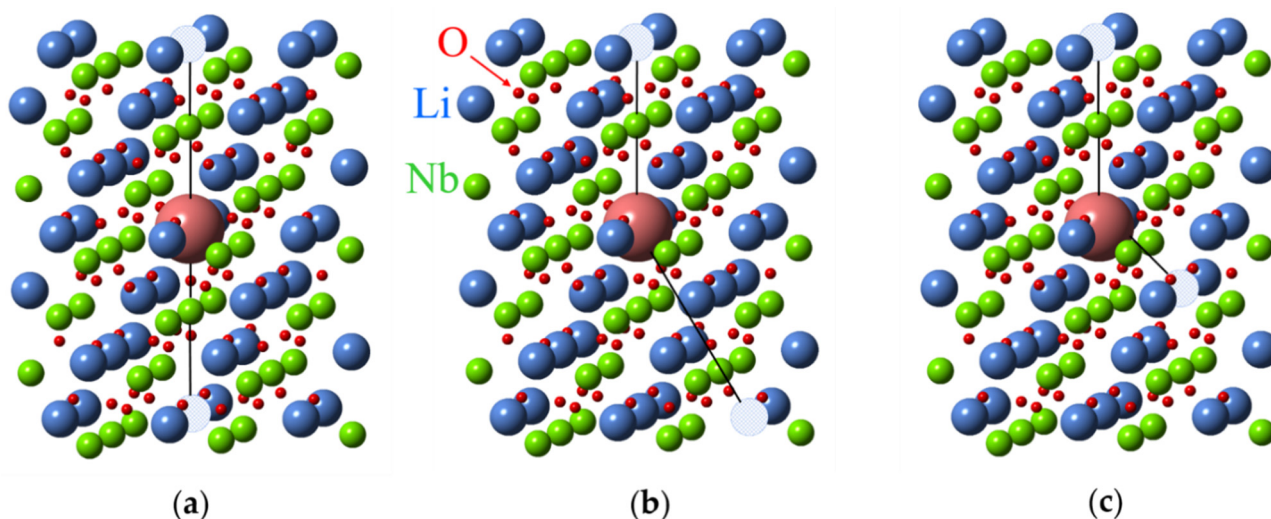
Figure 8. Divacancy models for an impurity substituted for Li$^+$ ion in LN crystal lattice. Hatched circles represent two v_{Li}. (**a**) Axial center, (**b**) nearly axial center, (**c**) low-symmetry center.

4. Structures of Impurity Centers

4.1. Monovalent Cations

The most probable incorporations of Me$^+$ is the substitution for Li$^+$. No charge compensation is required in this case. The Me$_{Li}^+$ center should have axial C$_3$ symmetry.

Proton H$^+$. This is an example of off-site position: protons occupy positions between two oxygen ions in an oxygen plane. The non-paramagnetic OH$^-$ centers were studied by infrared and NMR spectroscopies [80,106–108].

A hydrogen associated paramagnetic center (g = 2.0028, A = 3 mT at 77 K) was identified as an OH^{2-} ion, produced because of an electron capture by a diamagnetic OH$^-$ ion, substituting the O^{2-} ion in LN [109].

Ni$^+$ (3d^9, S = 1/2). Observed EPR spectra of the Ni$^+$ have axial symmetry at room temperature [110,111]. That excludes interstitial position in tetrahedral structural vacancies. However, at low temperatures the Ni$^+$ center has C$_1$ symmetry, as up to six lines were observed at arbitrary orientation of magnetic field (Figure 9a, after [111]).
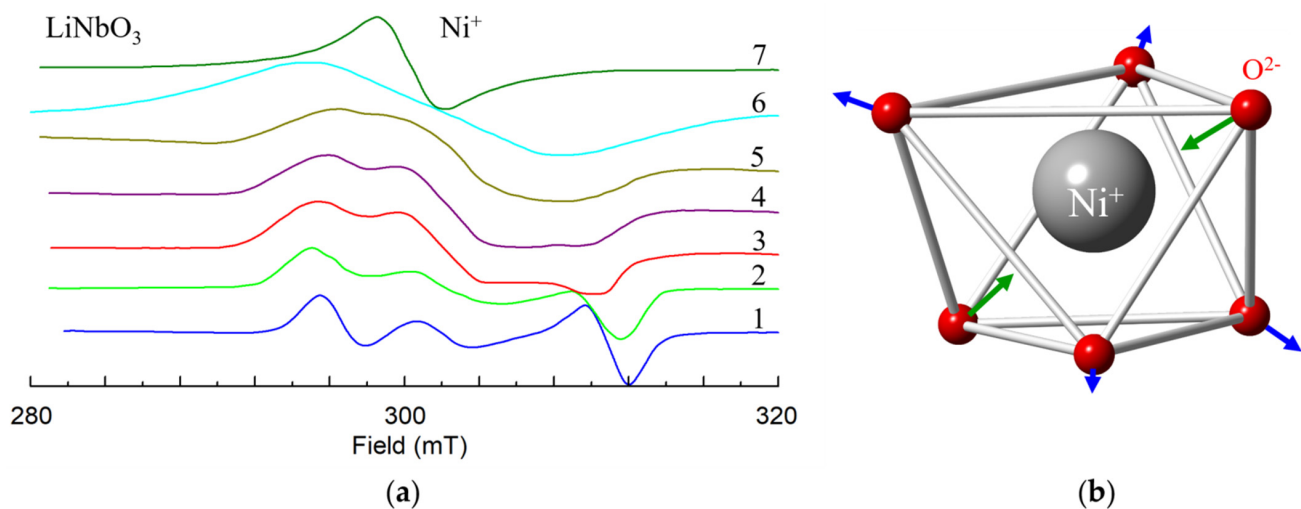
Figure 9. (**a**) X-band EPR spectra of Ni$^+$ in LiNbO$_3$ at θ = 25 deg in **zy** plane at various temperatures *T*: 1–40 K, 2–90 K, 3–151 K, 4–206 K, 5–244 K, 6–300 K. The spectrum 7 was measured at θ = 0 deg, *T* = 300 K. (**b**) Distortion of oxygen octahedron due to the Jahn-Teller effect.

The center was characterized by anisotropic **g**-tensor with principal values g_1 = 2.246, g_2 = 2.217 and g_3 = 2.061; principal axes of the **g**-tensor are rotated with respect to crystallographic axes by Euler angles $\alpha = \gamma \approx 0$, $\beta \approx 55°$. As the 3rd principal axis is directed approximately to one of the nearest oxygen ions, the reason for the low symmetry is a static Jahn-Teller effect for 3d^9 ions in Ni$^+$O$_6^{2-}$ complexes (Figure 9b, [111,112]), and not a presence of an intrinsic defect in the neighborhood. Dynamic averaging due to center reorientation leads to the axial symmetry of observed EPR spectra at room temperatures [111].

Mg$^+$ (3s^1, S = 1/2). Following vacuum reduction at 1000 °C, LN crystals heavily-doped with Mg exhibit an optical absorption spectrum that can be decomposed into two bands peaking near 760 and 1200 nm, and a broad EPR spectrum with g_c = 1.82 [113]. The 1200-nm band and ESR signal are associated with an electron trap (identical to the one produced during the irradiations). This electron trap is suggested to be a Mg$^+$ complex. There is an alternative interpretation of this spectrum [114].

4.2. Divalent Cations

For divalent Me^{2+} impurities a substitution for Li$^+$ ions and incorporation in structural vacancies has essentially less charge misfit than a substitution for Nb^{5+}. Since the Li-Li distance is much larger than Li-Nb or v$_{oct}$-Li, v$_{oct}$-Nb, the Me^{2+}$_{Li}$ + v$_{Li}$ centers should be slightly distorted by the presence of a local charge compensator. For v$_{Li}$ located on C$_3$ axis and for distant cation vacancies (local and distant charge compensation) axial centers should be observed.

Co^{2+} (3d^7, S = 1/2, I = 7/2). Dominant axial Co^{2+} center with $g_\parallel$ = 2.6 and $g_\perp$ = 4.96 ÷ 5.04, $A_\parallel \approx 0$, $|A_\perp|$ = 0.0154 cm^{-1}, as well as low-intensity low-symmetry satellite centers were observed in cLN [115,116] and vLN [117]. Similar **g**- and **A**-values were

reported for LiTaO$_3$:Co^{2+} [116]. The picture agrees with Co^{2+} substitution for Li$^+$ in the dominant axial center (Co$_{Li}$) and excess charge compensation by v$_{Li}$ (the Co^{2+} ⇔ 2Li$^+$ substitution mechanism). A small EPR line of axially symmetric cluster of Co^{2+} ions appeared in sLN [118] (Figure 10a). To explain it the substitution mechanism 4Co^{2+} ⇔ 3Li$^+$ + Nb^{5+} [119] was considered. The four Co^{2+} ions can occupy nearest possible cation sites by occupying one Nb site and three neighbor Li sites, creating a trigonal pyramid with C$_3$ symmetry (Figure 10b).
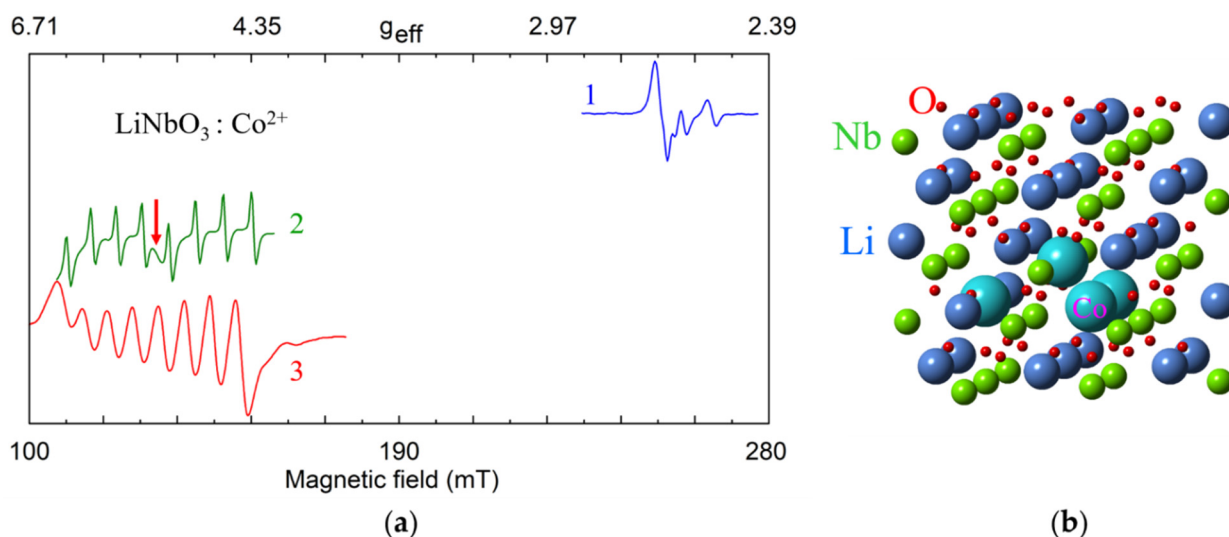
Figure 10. (**a**) Measured EPR spectra of Co^{2+}, X-band, *T* = 5 K. 1—sLN, **B** ∥ **z**; 2—sLN, **B** ∥ **x**; 3—cLN, **B** ∥ **x**. The red arrow indicates an additional line assigned to clusters of Co^{2+} ions. (**b**) Possible model for a cluster of four Co^{2+} ions substituted for one Nb^{5+} and three Li$^+$ ions.

From comparison of measured and calculated characteristics it was found that Co^{2+} does not occupy exactly the host Li$^+$ site but undergoes an off-center displacement 0.006 nm away from the oxygen octahedron center in LiNbO$_3$ (or LiTaO$_3$) [120,121].

Cu^{2+} (3d^9, *S* = 1/2). Copper nuclei have two isotopes ^{63}Cu (*I* = 3/2, g_n = 1.484, natural abundance 69.2%) and ^{65}Cu (*I* = 3/2, g_n = 1.588, 30.8%). Hyperfine interaction of Cu^{2+} electrons with their own nucleus leads to splitting of its single EPR line into a quartet ([110,111], and references there; [122–124]). As magnetic moments of ^{63}Cu and ^{65}Cu are very close, the quartets from the two isotopes overlap in cLN (Figure 11a). The Cu^{2+} center in LN was characterized by anisotropic **g**-tensor (g_1 = 2.095, g_2 = 2.111 and g_3 = 2.428; $\alpha = \gamma \approx 0, \beta \approx 51°$) [111]. At low temperatures a static Jahn-Teller effect for 3d^9 ions in Cu^{2+}O$_6^{2-}$ complexes reduces the center symmetry to C$_1$(Figure 11b). At room temperature, the Cu^{2+} center has axial symmetry due to center reorientation and motional averaging. The EPR parameters of the impurity Ni$^+$, Cu^{2+}, and Ni^{3+} in LiNbO$_3$ were theoretically studied from the perturbation formulas for 3d^9 ions [112,122].

Ni^{2+} (3d^8, *S* = 1). Several additional terms, which describe zero field splitting (ZFS) of energy levels, should be added to the spin-Hamiltonian (1) for paramagnetic centers with *S* > 1/2:

$$H_{ZFS} = \sum_{k=2,4,6} f_k \left[\sum_{q=0}^{k} b_k^q O_k^q(\mathbf{S}) + \sum_{q=1}^{k} c_k^q \Omega_k^q(\mathbf{S}) \right] \qquad (5)$$

Here $f_2 = 1/3, f_4 = 1/60, f_6 = 1/1260$; O_k^q, $\Omega_k^q(\mathbf{S})$—Stevens operators, which are non-zero for $k \geq 2S$. For C$_3$ symmetry only *q* equal to 0, 3, and 6 are allowed. For *S* = 1 only terms with *k* = 2 are present in Equation (5).

The Ni^{2+} centers in LN exhibit the EPR spectra of C$_3$ symmetry. Therefore, the sum in (5) turns into one term $b_2^0 O_2^0/3$. It was found that b_2^0 = −5.31 cm^{-1} and $\Delta g = g_\| - g_\perp$ = 0.04 [115,125]. Since EXAFS data supports Ni^{2+} substitution for Li$^+$ [24], the reasonable

choice for the charge compensator is one v_{Li} that is located on the C_3 axis or very far of Ni^{2+}.

A cluster substitution $4Ni^{2+} \Leftrightarrow Ta^{5+} + 3Li^+$ was considered for LT [126]. Note that an agreement of measured and calculated spin-Hamiltonian parameters [127] was obtained for Ni^{2+} substitution for Nb^{5+} in LN without a charge compensator.

The charge excess of one interstitial Me^{2+} or two Me^{2+}_{Li} could be exactly compensated by an additional O^{2-} ion. However, such a compensation looks unlikely, as the ionic radius of O^{2-} (about 1.4 Å) is larger than the sizes of octahedral or tetrahedral vacancies.
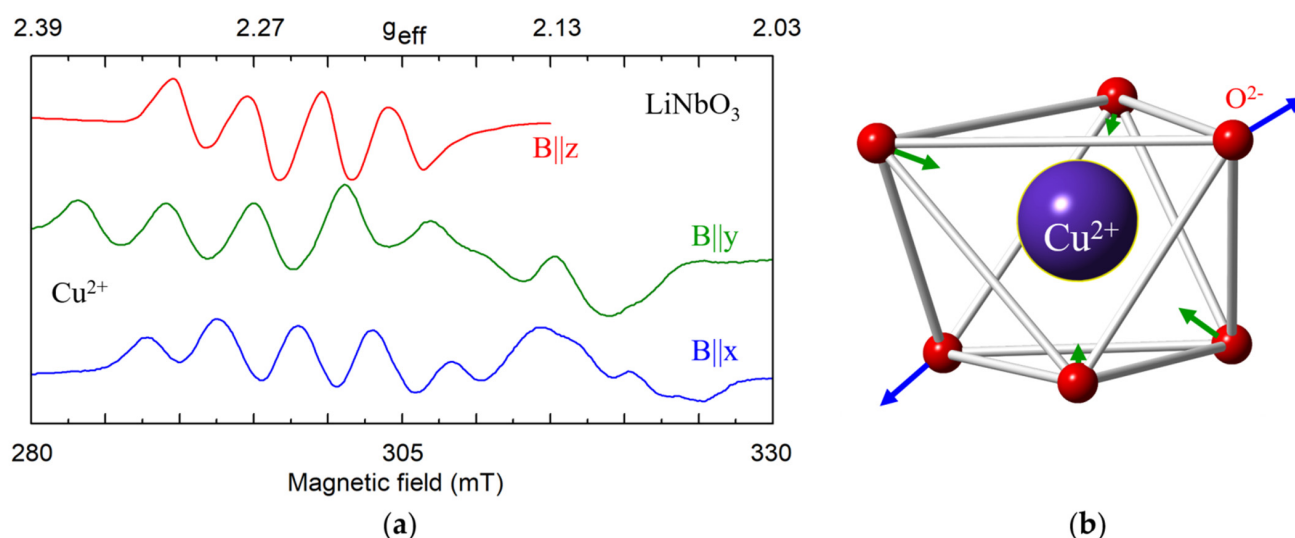
Figure 11. (**a**) Measured EPR spectrum of Cu^{2+} in LN, X-band, $T = 7$ K. (**b**) Distortion of oxygen octahedron due to Jahn-Teller effect.

Mn^{2+} ($3d^5$, $S = 5/2$, $I = 5/2$). For $S = 5/2$ the ZFS causes splitting into $2S = 5$ components of fine structure, each of them additionally splits into $2I + 1 = 6$ lines due to the hyperfine interaction of Mn^{2+} electrons with their own nucleus (Figure 12).
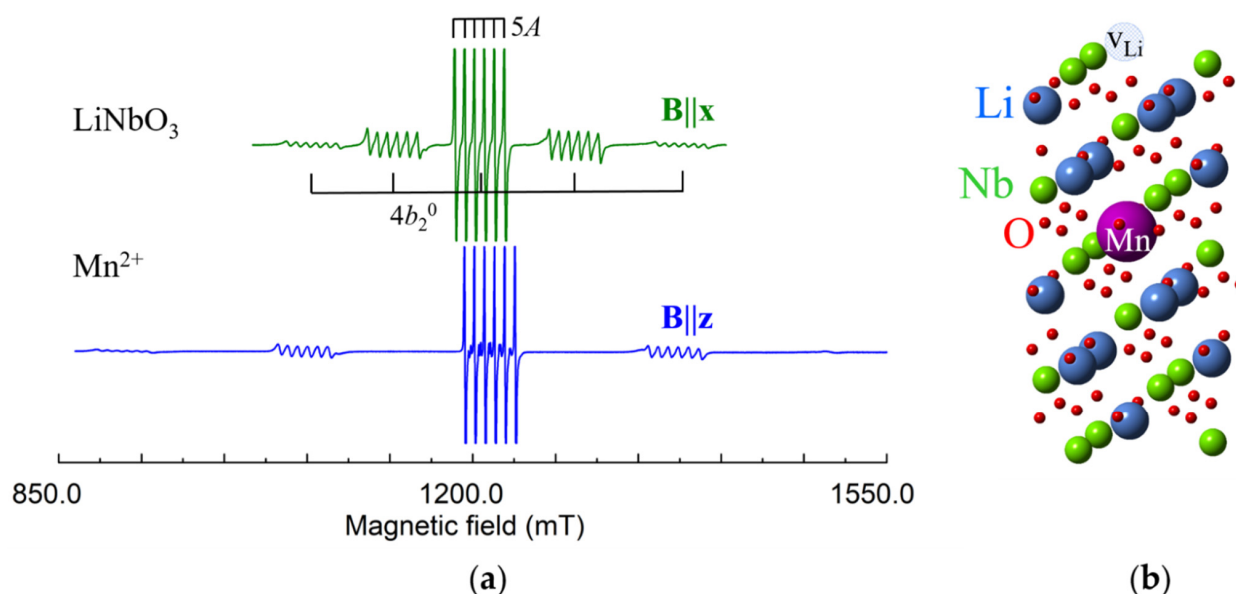
Figure 12. (**a**) Measured EPR spectrum of Mn^{2+} in LN_K, $\nu = 34.45$ GHz. (**b**) Model of axial Mn^{2+}_{Li} center with v_{Li}.

Angular dependences of Mn^{2+} in both LN and LT are described by spin-Hamiltonian of axial symmetry with $g \approx 2.0$, and $A \approx -0.008$, $b_2^0 = 0.0731$ (LN), $b_2^0 = 0.1694$ (LT), all in cm^{-1}, [128–138]. Our spectra (Figure 12) were fitted with $b_2^0 = 0.074$ (LN), $b_2^0 = 0.175$ (LT).

Hyperfine interactions with four Li and two Nb shells of surrounding nuclei were determined by ENDOR study in LN [139]. For isotropic **g**-tensor, the principal values of dipole-dipole interaction (3) can be described by:

$$b_{dd}^{(i)} = \frac{g\mu_B g_n^{(i)} \mu_n}{\left(R^{(i)}\right)^3} \tag{6}$$

Comparison of measured values of $b_{dd}^{(i)}$ with values calculated by Equation (6) for Li and Nb substitution has definitely shown that Mn^{2+} ions occupy Li site [139].

4.3. Trivalent Cations

Most transition metals (including iron, titanium, and chromium) and rare-earth elements enter LN in this valence. If Me^{3+} substitutes Li^+ there are three possibilities to compensate its 2+ excess charge: v_{Li}, v_{Nb} and self-compensation with $Me^{3+}{}_{Nb}{}^{5+}$ in the nearest or distant neighborhood. Every $Me^{3+}{}_{Li}$ can be compensated by two v_{Li}; every five $Me^{3+}{}_{Li}{}^+$ ions—by two niobium vacancies. The positive antisite defect Nb_{Li} can serve as a charge compensator for Me^{3+} replacing Nb^{5+} (but not $Me^{3+}{}_{Li}{}^+$ or $Me^{3+}{}_v$). It is remarkable that one $Nb^{5+}{}_{Li}{}^+$ exactly compensates the excess charge of two $Me^{3+}{}_{Nb}{}^{5+}$ ions. Since $v_{Li}{}^+$ has only one negative charge relative to the ideal lattice, it produces a 4–5 times weaker perturbation of the crystal field than $Nb^{5+}{}_{Li}{}^+$ or $v_{Nb}{}^{5+}$. Therefore the centers with $v_{Li}{}^+$ at distances of about 6 Å should probably are not distinguishable from axial centers with non-local charge compensation.

Interstitial Li^+ ions should be considered as charge compensators for $Me^{3+}{}_{Nb}{}^{5+}$ in Li-rich, VTE treated, and stoichiometric crystals. The association of $Me^{3+}{}_{Nb}{}^{5+}$ with one Li^+ ion in the nearest vacancy (partial local charge compensation) leads to an axial center, the second Li^+ in the next vacancies can decrease symmetry to C_1, if located off center axis and near the impurity. Mg^{2+} or Zn^{2+} ions substituted for Li^+ can be also suitable compensators for $Me^{3+}{}_{Nb}$.

Distances between the replaced ion and shells of possible location of compensators, various configurations of Me and charge compensators, as well as the symmetries of the corresponding complexes are given in References [87,140–142].

Cr^{3+} ($3d^3$, $S = 3/2$). In congruent and Li-rich LN samples, the EPR lines of dominant axial Cr^{3+} center, characterized with ZFS $b_2^0 \approx 0.39$ cm^{-1}, are accompanied with small satellite lines (Figure 13). Initial discussion with plausible but contradictory arguments about Li^+ or Nb^{5+} substitution [134,143–148] should be ended after PIXE [32] and detailed ENDOR [140] studies have shown that Cr^{3+} substitutes for Li^+ and slightly shifted from regular Li site. ENDOR measurements confirmed that Cr^{3+} substitutes for Li^+ also in all satellite centers. Therefore, the whole family of these Cr^{3+} centers can be described as $Cr^{3+}{}_{Li}$ with location of charge compensator on C_3 axis for axial or off it for low-symmetry centers.

The ENDOR measurements [140] found that hyperfine interactions with Nb nuclei of the 2nd and 3rd shells (Figure 5a) are stronger than with Li nuclei (Figure 14, bottom). However, lines of Nb nuclei on the center axis (1st and 4th shells) were not identified. It can be caused by unfortunate conditions of their observation, petal distribution of electron density for the $3d^3$ ion or absence of Nb ion in one of these sites, i.e., v_{Nb}. Two v_{Nb} can serves as the charge compensator for five $Cr^{3+}{}_{Li}$. Although the presence of v_{Nb} in undoped LN looks unlikely, the charge compensation defects in doped crystals (especially, if dopant concentrations exceed 0.X%) can differ from dominant intrinsic defects in undoped LN or LT. During the growth process, the required compensators can organize themselves around impurities or enter from air in order to minimize the creation energy for the impurity center. This is why structures with v_{Nb} were proposed for satellite centers of $Cr^{3+}{}_{Li}$ [87].
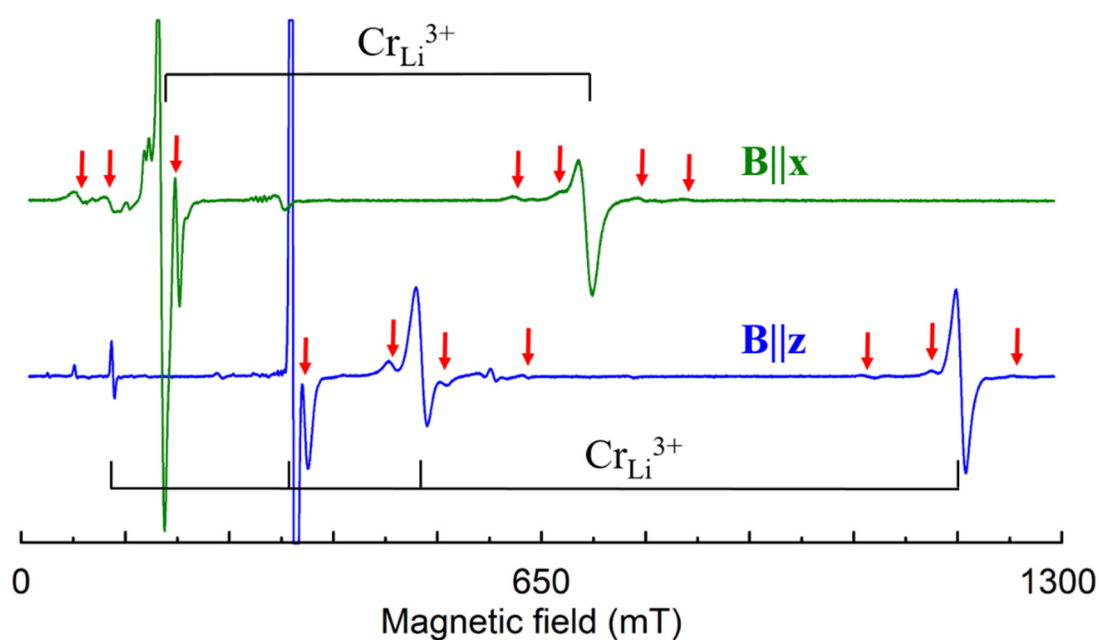
Figure 13. Measured EPR spectrum of Cr^{3+} in LN grown from the melt with $x_m \approx 60\%$ and 0.1 wt.% of Cr (room temperature, $\nu = 9.84$ GHz). Black braces indicate lines of dominant Cr^{3+} center, red arrows—lines of satellite centers.
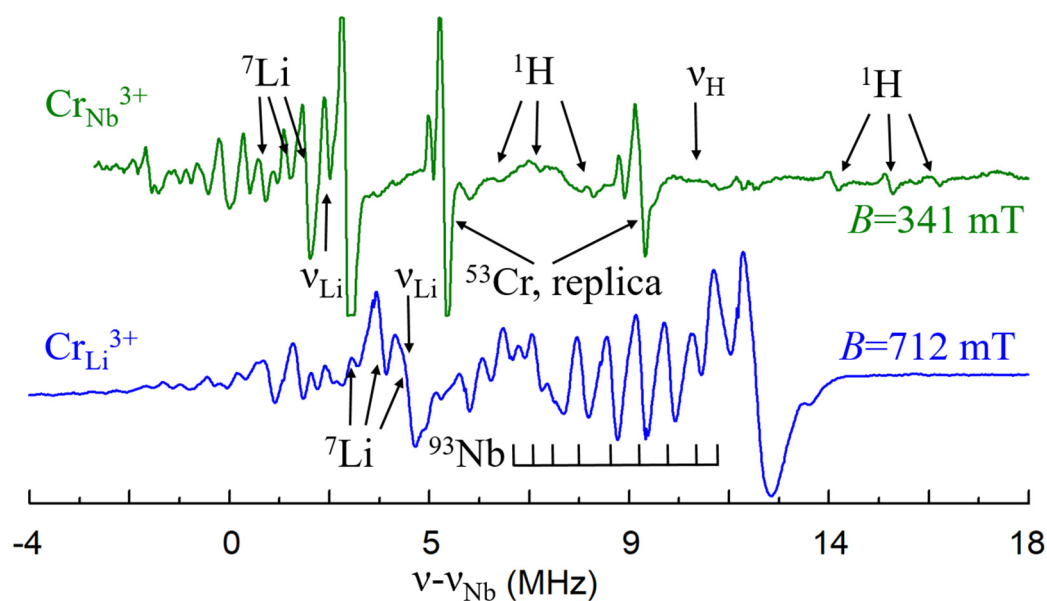
Figure 14. The ENDOR spectra of Cr^{3+}_{Li} (high-field EPR transition) and Cr^{3+}_{Nb} (central EPR transition) at $\mathbf{B} \parallel \mathbf{x}$, $T = 5$ K. To facilitate a comparison of the spectra, they were shifted to the ^{93}Nb Larmor frequencies.

On the other hand, ν_{Li} are considered as dominant intrinsic defects in LN and LT. Angular dependencies of EPR spectra for the dominant (C_3) and satellite (C_1 symmetry) Cr^{3+} centers (Figure 15) are pretty similar to observed patterns for Nd^{3+} (Figure 4). Therefore, two vacancy models for trivalent impurities (Table 1) and structures on Figures 7 and 8 can be viable alternatives for Cr^{3+} family.
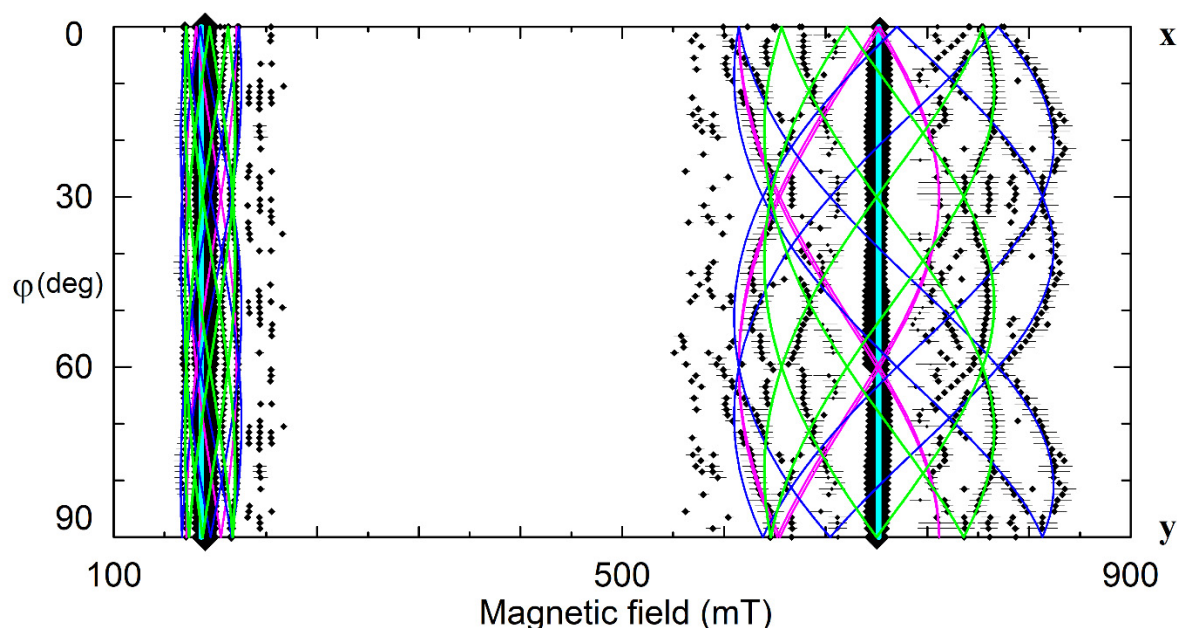
Figure 15. The angular dependencies of EPR spectra in the **xy** plane for LN:Cr^{3+} grown from the melt with $x_m \approx 60\%$, $\nu = 9.26$ GHz. Rhombs represent line positions; their sizes are proportional to line intensities. Horizontal whiskers near rhombs represent line widths. Cyan, lime, fuchsia, and blue curves represent simulated dependencies for axial Cr_1, and low-symmetry Cr_2, Cr_3, and Cr_4 centers, respectively.

A lack of intrinsic defects in stoichiometric samples leads unavoidably to a change of charge compensation mechanism for trivalent impurities, and substitution for Nb^{5+} becomes possible. An axial Cr^{3+} center with significantly smaller ZFS $b_2^0 = 0.0215$ cm^{-1} (Figure 16a) was found in LN_K samples [142]. ENDOR study has shown that hyperfine interactions with Li nuclei significantly larger than with Nb nuclei for this center, i.e., the nearest surrounding consist of Li nuclei. This means that Cr^{3+} substitutes for Nb^{5+} in this center. As lines of protons, H^+, were found in the ENDOR spectra (Figure 14, top), they compensate the negative charge of $Cr^{3+}_{Nb}{}^{5+}$ (Figure 16b).

Exchange interaction $\mathbf{S}^A\mathbf{J}\mathbf{S}^B$ between spins of Cr^{3+} ions ($S^A = S^B = 3/2$) leads to gaps between states with values of total spin $S = S^A + S^B$ equal to 0, 1, 2, and 3. The state with $S = 0$ is non paramagnetic. For pairs at a close distance the gaps can exceed energies of microwave quantum (36 GHz $\approx$ 1.2 cm^{-1}). It was found by magneto-optical study that for Cr^{3+}_{Li}–Cr^{3+}_{Nb} substituted for nearest Li and Nb sites (at the distance about 0.3 nm) the exchange interaction is antiferromagnetic and $J \approx 480$ cm^{-1}. As 1 K $\times$ $k_B \approx$ 0.7 cm^{-1} the upper states of such pairs with non-zero S are not populated even at room temperatures, and the pairs are EPR silent. However, the pairs of the next orders with the isotropic exchange coupling parameter $J \approx 1.5$ cm^{-1} were observed by EPR at relatively low concentration of chromium in LN (less than 0.1 at.%) [87,134,148–150].
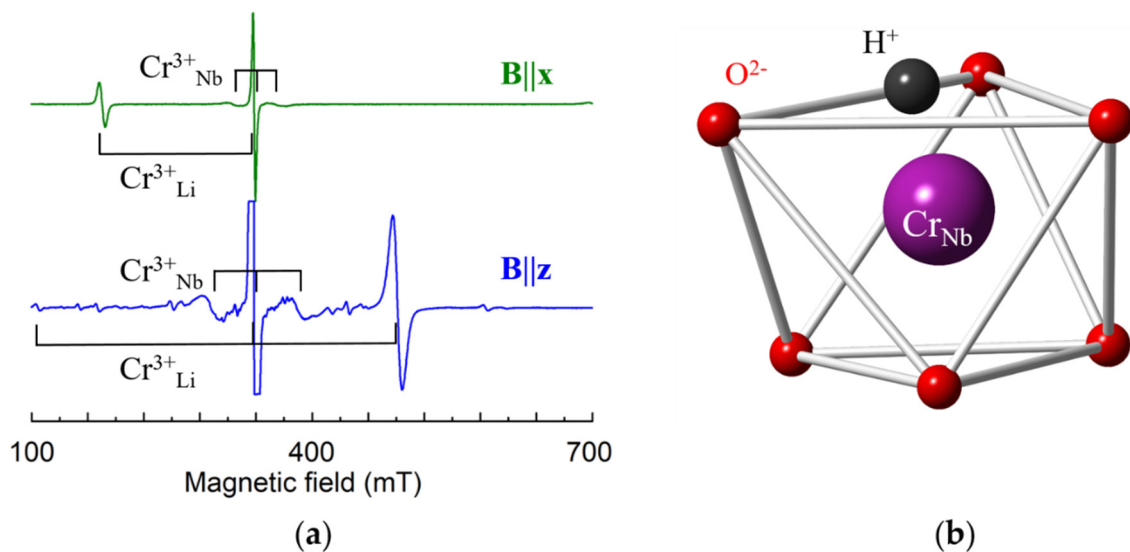
Figure 16. (**a**) Measured EPR spectra of Cr^{3+} in LN grown from the melt with addition of K_2O and 1 wt.% of Cr; room temperature, ν = 9.445 GHz. (**b**) Model of Cr^{3+}_{Nb} center.

PIXE/channeling study [32] revealed that chromium ions occupy both regular cation sites (60% on Li sites and 40% on Nb sites) in congruent LN doped with 0.1 mol.% of Cr. This means that the majority of chromium ions enter cLN as non-paramagnetic pair centers. The EPR observes only a top of iceberg in cLN: dominant Cr^{3+}_{Li} and small signals of non-nearest paramagnetic pairs.

ENDOR study of Cr^{3+} centers in LN heavily doped with Mg and co-doped with Cr has unambiguously shown that Cr^{3+} in the dominant center has ZFS b_2^0 close to zero (nearly isotropic case) and substitute for Nb [151–155]. Measured anisotropic hyperfine interactions of Cr^{3+} with for four Li shells were close to $b_{dd}^{(i)}$ for Nb site. From comparison of data obtained by EPR, ENDOR, optical absorption, fluorescence, fluorescence line narrowing, selective excitation and radiative lifetime measurements [156–162] it has been concluded that the addition of Mg^{2+} ions to LN does not create new Cr^{3+} complexes, but changes the relative concentrations of the Cr^{3+}_{Li} and Cr^{3+}_{Nb} centers.

The measured value of ZFS for dominant Cr^{3+} in cLT $b_2^0 \approx 0.444$ cm^{-1} [144] is very close to the value for Cr^{3+}_{Li} in LN. EPR spectra of this center together with signals of weaker intensities of a second center [163,164] were explained in a supposition that they originate from Cr^{3+} ions located at Li$^+$ sites and that two v_{Li} play the role of a divalent charge compensator for both centers. EPR study of Cr^{3+} in nsLT and superposition model analysis [165] are in good agreement with the Cr^{3+} substitution for Li. The temperature dependence of $b_2{}^0$ term showed a non-monotonic behavior in the region of 40 K.

Finally, a lot of studies were devoted to various properties of Cr^{3+} in LN and LT crystals of different compositions in order to clarify relations of optical characteristics with structures of chromium centers [166–175] etc.

Dy^{3+} (4f^9). The observed Zeeman splitting [143] was described with g-tensor of axial symmetry: $g_{\parallel}$ = 8.7 and $g_{\perp}$ = 1.3. The single EPR line had width about 8–10 mT at **B**||**z** and became broader at **B**⊥**z**. Such a behavior can be related to unresolved splitting due to satellite centers, if Dy^{3+} occupies Li position and its charge is compensated by v_{Li}. Two Dy^{3+} centers with $g_{xx}(1)$ = 2.56(1), $g_{zz}(1)$ = 4.43(1), and $g_{xx}(2)$ = 6.67(1), $g_{zz}(2)$ = 1.23(1) and linewidth about 20 mT were registered in LN after γ-irradiation [176]. Both centers were attributed to Dy$^{3+}_{Li}$. A broad line of the third center with $g_{zz}(3) \approx 1.2$ appeared only at **B** close to the **z**-axis. Weak hyperfine lines due to isotopes ^{161}Dy (natural abundance 19%), ^{163}Dy (2.49%) was observed in single crystal of LN [177].

Er^{3+} (4f^{11}). Due to fast spin-lattice relaxation, the EPR signals of Er^{3+} are observable at low-temperatures only. Earlier studies claimed that Er^{3+} ions in cLN create an axial

center with $g_{\parallel} \approx 15.1$–15.4 and $g_{\perp} \approx 2.1$ [143,178] or $g_{zz} \approx 15.5$ and $g_{xx} \approx g_{yy} \approx 0.8$ [179]. A proposed model with lithium vacancies statistically distributed around Er^{3+}_{Li} [179] supposed that the center with no vacancies in surrounding, i.e., the center with axial C_3 symmetry, should give a dominant (54%) line in the EPR spectra. Note that angular dependences of EPR spectra in **xy**-plane were not measured in these studies. Later measurements in all three principal planes [180–183] have shown that there is no line without angular dependence in the **xy**-plane, i.e., dominant Er^{3+} center in cLN has C_1 symmetry. This does not agree with statistically distributed v_{Li} around Er^{3+}_{Li} [179].

Significant narrowing of EPR lines in LN_K (Figure 17a) allowed us to trace two different Er_1^{3+} and Er_2^{3+} centers with extrema at about 15, 45 and 75 degrees in **xy** plane (Figure 17b) [184,185]. The divacancy model (Figure 7) gives a possible explanation if a shift of Er^{3+}_{Li} from regular Li site is taken into account: RBS, XSW and ion-beam/channeling studies have determined that Er occupies Li sites, but is shifted from the ferroelectric Li position by 0.03 [186], 0.046 [187], and 0.02 nm [188]. In this case, distances from Er_{Li} to the v_{Li} in the 1a and 1b shells (Figures 5a and 7b) are completely different, and these centers have one charge compensating v_{Li} in the nearest neighborhood (the shell 1a for Er_1, and 1b for Er_2), and the second v_{Li} in the next nearest neighborhood (shells 2a, 2b, Figure 7).
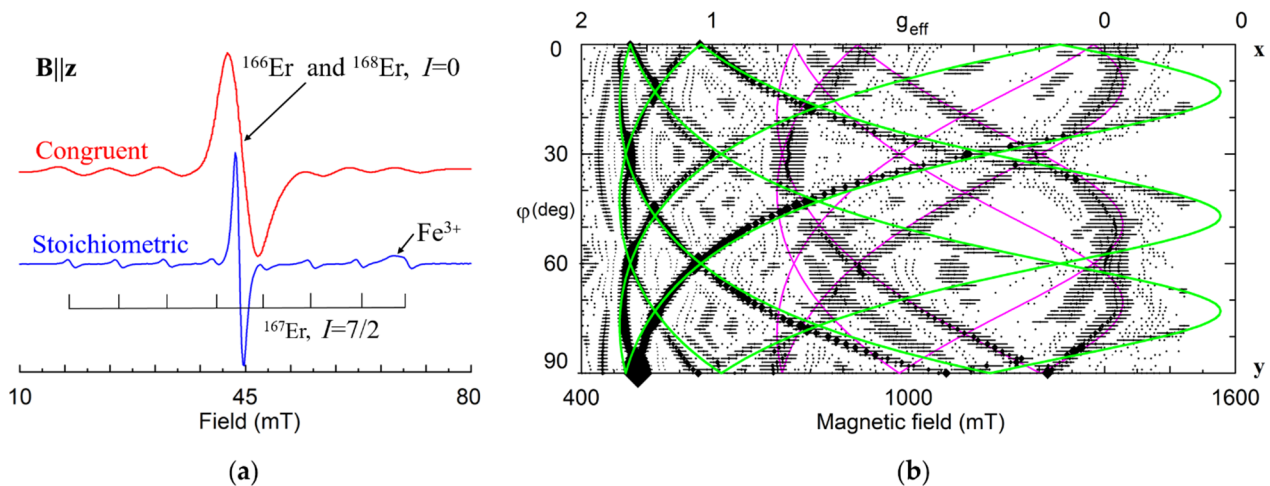
Figure 17. (**a**) EPR spectra of Er^{3+} in congruent and stoichiometric LN at **B** || **z**, X-band. (**b**) Calculated angular dependence of EPR spectra in **xy** plane for the Er_1^{3+} (green lines) and Er_2^{3+} (fuchsia lines) centers in sLN. Symbols with horizontal whiskers represent line position and widths.

Magnetic moments $\mu_B g\mathbf{S}$ for both Er^{3+} centers are very large and strongly anisotropic. At low temperatures their interactions lead to magnetic ordering for Er concentration about 0.5 at.% in sLN [189].

Various models with two v_{Li} were also extensively discussed in papers devoted to site-selective spectroscopy [190–196] and references there. Note that models with one of two v_{Li} on **z**-axis (Figure 8) do not agree with the EPR spectra for dominant lines and hyperfine satellites on Figure 17a. However, such centers can probably be associated with weaker lines or may have no EPR lines at all, if they are non-paramagnetic.

EPR spectra detected in cLN heavily doped with Mg or Zn and co-doped with Er were described with $g_{\parallel}$ = 4.3, $g_{\perp}$ = 7.6 for the Mg-doped samples and $g_{\parallel}$ = 4.26, $g_{\perp}$ = 7.8 for the Zn-doped ones [197]. The spectra can be attributed to Er^{3+} located at the Nb^{5+} site of LN, as they are compared to additional centers observed for some trivalent transition metal ions (particularly Cr^{3+}) in LN: Mg or LN:Zn.

Fe^{3+} ($3d^5$, $S = 5/2$). EPR studies have shown that the dominant iron center, Fe_1 in cLN has axial symmetry with the ZFS b_2^0 about 0.1680 cm^{-1} [131,133,134,198–208]. Calculations of optical and EPR characteristics based on the superposition models or generalized crystal field theory gave a preference for Nb substitution [209], no definite conclusion for Li

or Nb substitution [210–213] or some preference for Li site [214,215]. Mössbauer [33,34] and Raman [35] spectroscopy data, Stark effect [216] were interpreted on the base of Fe substitution for Li. Iron clusters were observed at high Fe concentration [33]. Comparison of calculated dipole-dipole interactions of Fe^{3+} electrons with surrounding Li nuclei for Li and Nb substitution (Equation (6)) with measured ENDOR spectra [38–40] has shown that Fe^{3+} is undoubtedly located in Li site in both cLN and cLT (Figure 5a). Independently, XSW [12,28], EXAFS [21–26], and ion beam/channeling [18,27] confirmed Fe^{3+} substitution for Li^+. It was concluded also that Fe^{3+} ions can be shifted from regular Li-site; however, the obtained values for the shift were very different: 0.006 nm [21] or 0.05 nm from octahedron center [24], less than 0.012 nm [25], about 0.01 nm [26], 0.018 ± 0.007 nm [28], less than 0.005 nm [39]. Fitting observed ENDOR data in LN crystals grown from Li-rich melt ($x_m \approx 55\%$) was obtained with the shift 0.009 nm from Li site [217].

Fe^{3+} center with small ZFS, Fe_2 observed in congruent LN doped with Mg [104,218–222], In [223], and Zn [224] was assigned to $Fe^{3+}{}_{Nb}$.

Comparison of EPR spectra of congruent (Figure 18a, 1), near-stoichiometric grown from Li enriched melts (Figure 18a, 2) and grown from congruent melt with the addition of K_2O, LN_K samples (Figure 18a, 3) shows[a]:

- Lines of allowed transitions in LN_K become symmetric—intensities of left (up) and right (down) wings become equal.
- Lines of forbidden transitions (see yellow box on Figure 18) disappear in LN_K.

In LN_K the EPR lines become narrower (up to dozen times at some magnetic field orientation). The narrowing strongly increases spectral resolution. This allows to register even trace impurities in undoped (nominally pure) LN_K samples (see lines of Fe^{3+} and Mn^{2+} on Figure 18a, 3).
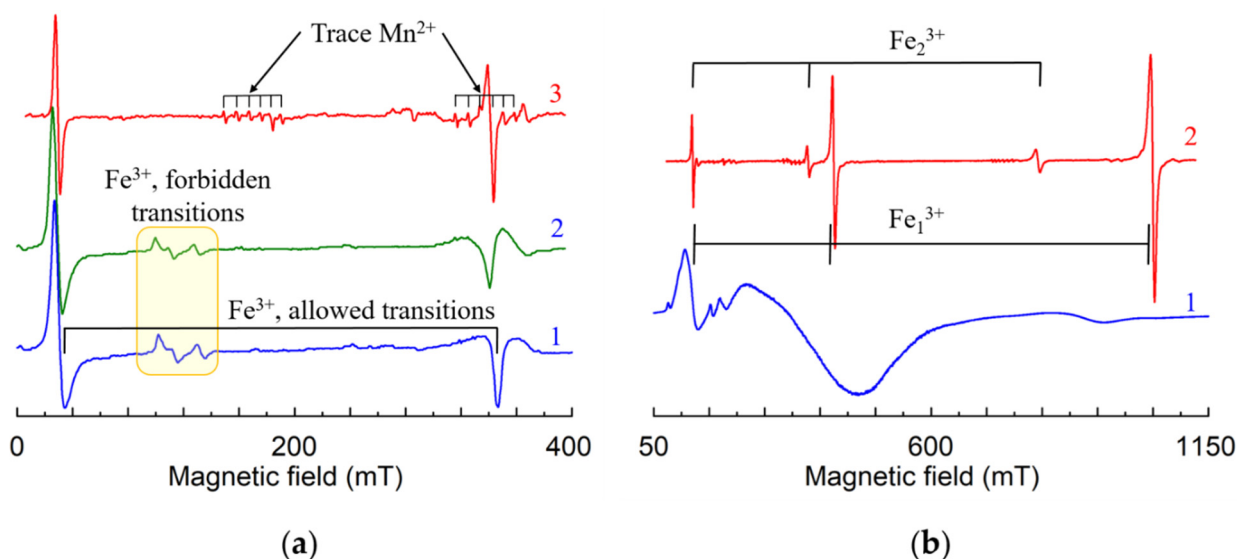
Figure 18. Normalized spectra of Fe^{3+} in LN (**a**) and LT (**b**), X-band. (**a**) Congruent (1), grown with x_m = 0.545 (2), undoped sample grown from congruent the melt with 6 wt% of K_2O (3), **B** ‖ **z**. (**b**) Congruent (1), vapor transport equilibrium (VTE) treated sample (2), **B** ‖ **x**.

[a] A brief glance on history of sLN for curios researchers. Looking for better crystals, G. I. Malovichko asked crystal growers for different samples of LN and LT. Dr. E. P. Kokanyan (at that time, one of the engineers in the group of Dr. V. T. Gabrielyan) was interested to grow crystals under various conditions (melt composition x_m, growth under applied electric field, variation of temperature, etc.). He has prepared for her a set of non-stoichiometric LN samples grown from melts with x_m from 43% to 60%. During her PhD research of LN and LT of different compositions, Malovichko found that EPR lines become narrower and more symmetric in samples grown with larger x_m. Dr. V. G. Grachev has simulated

EPR spectra with random distributions of non-axial components of ZFS, b_2^q ($q \neq 0$) for Cr^{3+} and Fe^{3+} and confirmed that line width and asymmetry, as well as intensities of forbidden transitions are related to intrinsic defects in non-stoichiometric samples [43]. In 1991, on Malovichko's request Dr. Kokanyan has grown several congruent samples with 2, 4, and 6% of K_2O in the melt (LN_K). First EPR measurement has surprisingly shown narrow symmetrical lines in LN_K with traces of Fe^{3+} (Figure 18a, 3). Based on the experience of studies of Li-rich samples, it was concluded that the concentration of intrinsic defects in LN_K is smaller than in LN grown from the melt with $x_m = 60\%$, and that K_2O may serve as a catalyst in electrochemical reaction of crystal growth [56]. As abilities of research techniques in Ukraine were limited, Dr. Malovichko asked Prof. O. F. Schirmer (Osnabrueck University, Germany) for an international collaboration. Prof. Schirmer was very enthusiastic and has quickly managed to involve many of his colleagues in the investigation of LN_K properties. K. Betzler, B. Faust, B. Gather, F. Jermann, S. Klauer, U. Schlarb, M. Wesselmann, M. Woehlecke and others participated in the LN_K study by different techniques resulting in publications [57,69,77].

All these features are the result of significant reduction of intrinsic defects in LN_K samples. Estimations of crystal composition x_C made by different methods [59,68,77,79] have shown that x_C can exceed 49.8–49.9%, i.e., LN_K is really a stoichiometric crystal.

As for other impurities, the lack of intrinsic defects in LN_K:Fe has led to the appearance of centers where impurities substitutes for Nb. Two additional axial Fe^{3+} centers named Fe_3 and Fe_4 were observed in LN_K [69]. Their ZFS are $b_2^0 = 0.0495$ and $b_2^0 = 0.0688$ cm^{-1}. Compared with Fe_2, the Fe_3 and Fe_4 centers were also assigned to Fe^{3+} in Nb sites with different charge compensation. The Fe^{3+} center with $b_2^0 = 0.0656$ cm^{-1} (that is very close to b_2^0 for Fe_4) was observed in VTE treated stoichiometric LN [76]. Therefore, Fe_4, Fe_3, and Fe_2 were attributed to Fe_{Nb} with different charge compensator ions in nearest structural vacancy v_{oct}: Fe_4—non-regular, interstitial Li^+_v (Figure 19a), Fe_3–K^+_v, and Fe_2–Mg^{2+}_v. Two Li^+_v (Figure 19b), or interstitial Mg^{2+}_v or two $Mg^{2+}_{Li}^+$ are required for full charge compensation of $Fe^{3+}_{Nb}{}^{5+}$. Our measurements of EPR in LN:Mg show angular patterns with extrema at 15, 45 and 75 degrees in **xy** plane. It is why we think that models with two differently located $Mg^{2+}_{Li}^+$ (Figure 19c,d) are more suitable for Fe_{Nb} (similar to models with two v_{Li} for Fe_{Li}). ENDOR measurements could confirm some of these reasonable assignments.

Dominant $Fe_1{}^{3+}$ center in cLT has $b_2^0 = 0.33$ cm^{-1} [38,225] (Figure 18b, 1), and according to ENDOR data [38] it is definitely Fe^{3+}_{Li}. Line narrowing in nsLT grown by double crucible Czochralski method from an Li rich melt composition (about 60 mol.% Li_2O) allowed to determined b_2^0 more accurately [226].

The main features of the spectra in sLT obtained by VTE treatment are strong line narrowing, higher resolution, and a clear presence of the second axial $Fe_2{}^{3+}$ center with $b_2^0 = 0.205$ cm^{-1} (Figure 18b, 2) [75]. Comparison of calculated angular dependences of ENDOR frequencies for Li and Nb substitution using Equation (6) with measured ones (Figure 20) obviously shows that in the case of Fe_2 center the Fe^{3+} ion substitutes for Nb. Both Fe_1 and Fe_2 centers in sLT have C_3 symmetry. No foreign nuclei in the nearest neighborhood were detected for Fe_1. As sLT still have some residual concentration of v_{Li}, the charge compensators for Fe_1 centers are one v_{Li} on center axis (shells 5a, 5b on Figure 7) and probably one other distant v_{Li} (any vacancy cannot be directly detected by ENDOR).
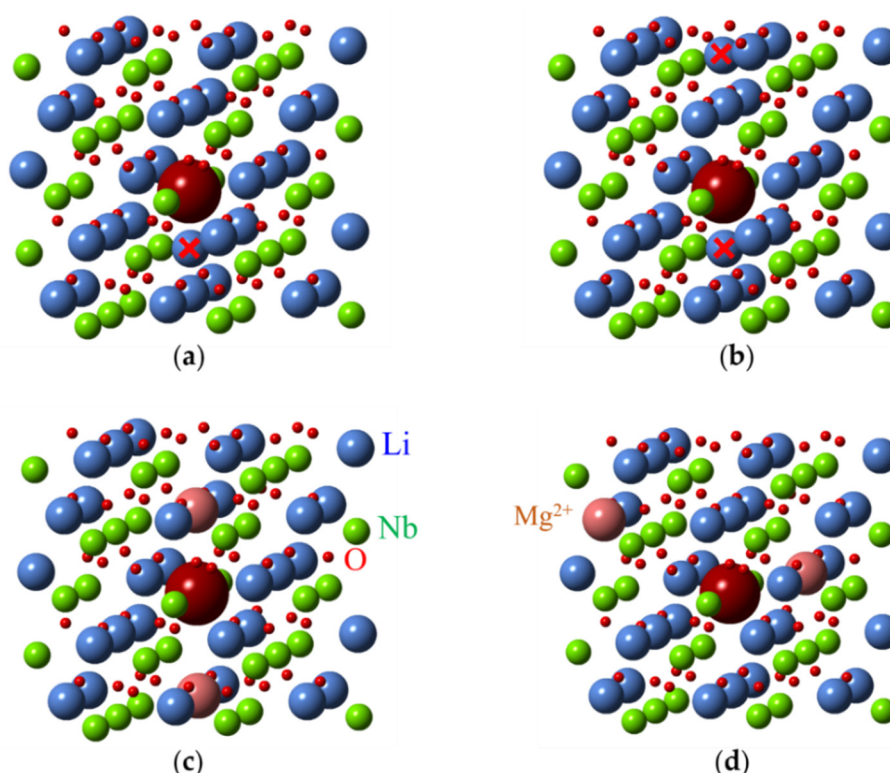
Figure 19. Possible structures of $Me^{3+}_{Nb}{}^{5+}$ (large magenta ball) centers in LN. Structure with one (**a**) and two (**b**) additional Li ions in v_{oct} (marked with red crosses). Axial (**c**) and low-symmetry (**d**) structures with two $Mg^{2+}_{Li}{}^{+}$ ions.
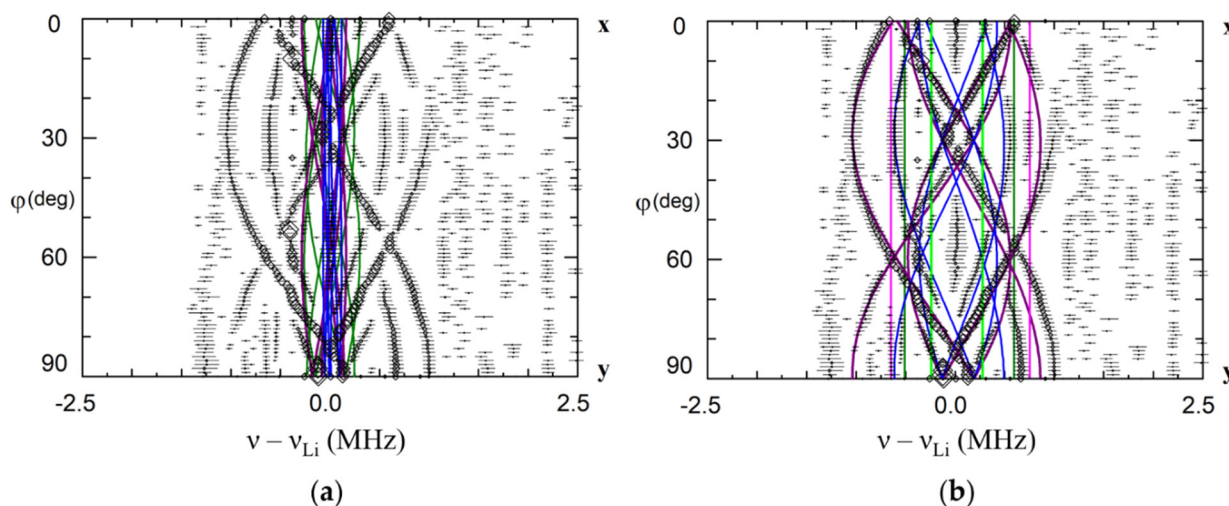
Figure 20. Angular dependence of ENDOR frequencies of Li nuclei in **xy** plane for the $Fe_2{}^{3+}$ center in $LiTaO_3$. The green, magenta, blue and lime curves—calculated frequencies for Li nuclei of the 1st, 2nd, 3rd and 4th shells based on dipole-dipole interaction for Fe^{3+}_{Li} (**a**), and Fe^{3+}_{Nb} (**b**). Fuchsia lines on (**b**)—calculated frequencies for the additional Li nucleus in the nearest v_{oct} on the axis of Fe^{3+}_{Nb} center. ENDOR frequencies represented by rhombs were measured on the EPR line at B = 1162 mT ($\nu \approx 34.5$ GHz).

A pair of ENDOR lines for Fe_2 (fuchsia line on Figure 20b) were attributed to the additional Li^{+}_{v} in the nearest v_{oct} at the distance about 0.277 nm from Fe^{3+}_{Nb}. It is difficult to make a choice between two models on Figure 19a,b as lines of the second Li^{+}_{i} in the next or next-next v_{oct} are not identified yet. The ratio of concentrations of Fe_2 and Fe_1 centers changed from less than 0.2 for Fe concentrations 1.1×10^{19} cm^{-3} to about 1 for 6.7×10^{19} cm^{-3} in the crystals. Therefore, there are three different mechanisms for

excessive charge compensation: distant v_{Li} for small concentrations of $Fe^{3+}_{Li}{}^+$, partial self-compensation of charges of $Fe^{3+}_{Li}{}^+$ by $Fe^{3+}_{Nb}{}^{5+}$ and partial compensation of $Fe^{3+}_{Nb}{}^{5+}$ by Li^+ in v_{oct} for Fe^{3+} concentrations, which exceed the concentration of v_{Li}.

Gd^{3+} ($4f^7$, $S = 7/2$). The EPR spectrum for every Gd^{3+} center consists of $2S + 1 = 8$ strong lines of fine structure and many low intensity lines of so called forbidden transitions due to nearly equal values of Zeeman splitting and ZFS. Results of the first EPR study [227], were interpreted as a presence of two axial Gd_1 and Gd_2 centers with $b_2^0 = 0.118$ and $b_2^0 = 0.126\ cm^{-1}$. From the viewpoint of charge compensation, a preference was given to Gd^{3+} substitution for Nb^{5+}. A small rhombic distortion ($b_2^2 \approx 0.004$) determined for Gd_2 [228] was attributed to an off axis charge compensator, while for Gd_1 the charge compensator may either be absent or must lie on the same threefold axis as Gd^{3+}. However, no decision on whether Gd^{3+} substitutes for Li^+ or Nb^{5+} or for both was made. Similar results with slightly smaller $b_2^2 \approx 0.002$ were also reported [229].

At least four different Gd^{3+} centers were identified in our study of Li-rich LN doped with 1 wt.% Gd_2O_3 in the melt. As patterns for every EPR transition in **xy**-plane (Figure 21) are very similar to presented on Figures 4b and 15, the divacancy model is suitable for Gd^{3+} in LN. Gd^{3+} substitutes for Li^+ in all centers. The dominant axial Gd_1 center and low-symmetry Gd_2, Gd_3, and Gd_4 centers have v_{Li} in positions described in Table 1. This assignment agrees with the Gd substitution for Li found by RBS and PIXE channeling [31].
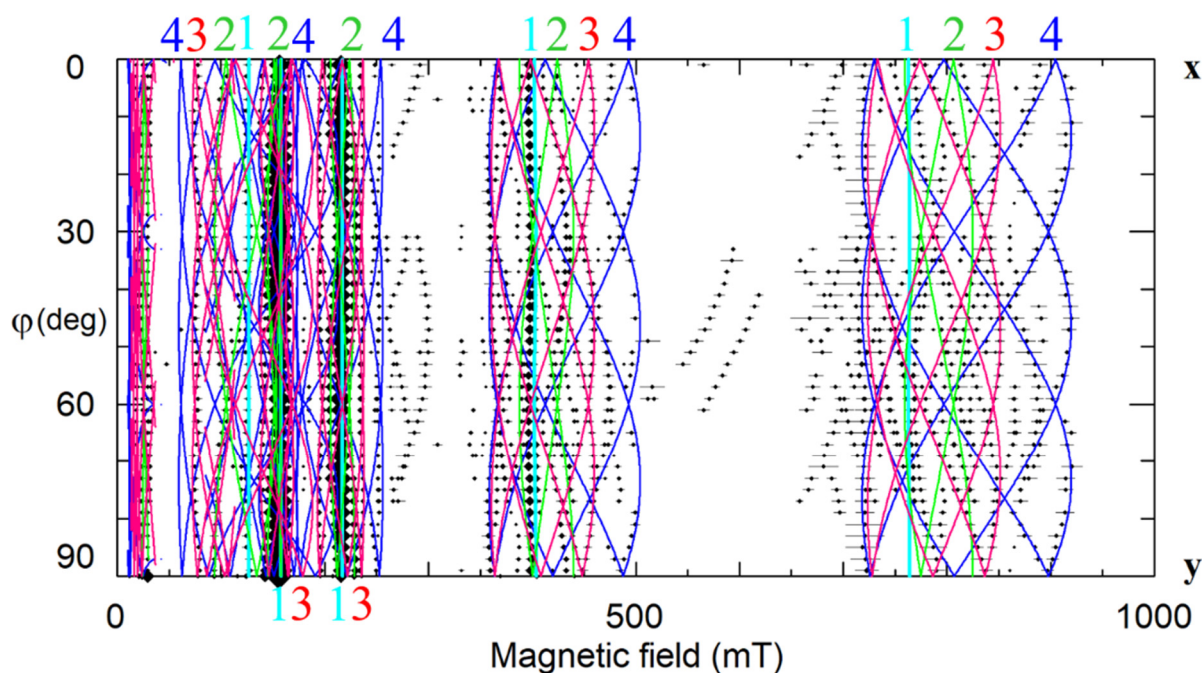
Figure 21. The angular dependencies of EPR spectra in **xy** plane for Li-rich LN:Gd^{3+}, $\nu = 9.26$ GHz. Rhombs represent line positions; horizontal whiskers—line widths. Cyan, lime, fuchsia, and blue curves are simulated dependencies for axial Gd_1, and low-symmetry Gd_2, Gd_3, and Gd_4 centers, respectively.

Nd^{3+} ($4f^3$) First EPR spectra have shown that in cLN Nd^{3+} creates an axial center with $g_\parallel \approx 1.43$ and $g_\perp \approx 2.95$ (Nd_1) [143,144,230] and second center with $g_\parallel \approx 1.33$ and $g_\perp \approx 2.95$ (Nd_2) [143]. EPR/ENDOR studies in sLN [91–93] has established that Nd^{3+} substitutes for Li^+, and resolved eight different Nd^{3+} centers. Divacancy models explain angular dependencies of EPR spectra for the whole family of Nd^{3+} centers [93], and Section 3.1 of this paper.

It is supposed that Nd^{3+} center found in LN:Mg and LN:Zn belong to Nd^{3+} substituted for Nb [231].

Ti^{3+} ($3d^1$, $S = 1/2$) EPR spectrum of Ti^{3+} consist of one line with $g_\parallel \approx 1.961$ and $g_\perp \approx 1.840$ in LN [232–234], and $g_\parallel = 1.948$, and $g_\perp = 1.827$ in reduced LT [235]. An axial

EPR signal observed in vacuum annealed $LiNbO_3$ single crystals doped with 8 mol.% Mg and 0.05 mol.% Ti has $g_\parallel = 1.760$ and $g_\perp = 1.786$ for $T = 5$ K and $g_\parallel = g_\perp = 1.893$ for $T = 74$ K. The signal has been attributed to Ti^{3+} on Nb site [236–240]. The **g** tensor components of these centers were explained by a model calculation involving a dynamic pseudo Jahn-Teller effect. Spin-orbit coupling, lattice vibration, pseudo Jahn-Teller interaction, and the Zeeman term were treated on equal footing. Electron transfer from the observed Ti^{3+}_{Nb} center to lattice niobiums, resulting in Nb^{4+} trapped polarons, has been stimulated by illumination in the near UV region.

Yb^{3+} ($4f^{13}$) The EPR lines of Yb^{3+} in congruent LN are very broad (Figure 22a,c) [241]. The axial center Yb_1 with $g_\parallel \approx 4.7$–4.86 and $g_\perp \approx 2.7$ was observed in cLN with 0.5–1.2 wt.% Yb_2O_3 in the melt [144,230,241]. The second Yb_2^{3+} center with $g_\parallel \approx 1.9$ and $g_\perp \approx 2.8$ was found in LN:Mg [241]. By comparison of these observations with EPR data for Cr^{3+}, Er^{3+}, Fe^{3+}, and Ti^{3+} in LN and LN:Mg the Yb_1 center was tentatively assigned to Yb^{3+}_{Li} and Yb_2 center to Yb^{3+}_{Nb}. A variation of lattice parameters found in cLN:Yb supported Yb^{3+} substitution for Li compensated by Li^+ vacancy [242].

Complicated EPR spectra without 60 deg repetitions in **xy** plane were registered in cLN doped with 1wt.% Yb, and cLN doubly doped with 0.8 wt.% of Yb and 0.1 wt.% of Pr [243–247]. Some of the spectra were attributed to Yb^{3+} pairs with the parameter of isotropic exchange interaction $J = -0.0283$ cm^{-1}.

Our study of LN_K crystals doped with 0.02 wt.% Yb_2O_3 has shown that the broad line observed in cLN belongs in reality to a family of at least 8 different centers (Figure 22b,d) [92,248,249]. Hyperfine structures from isotopes ^{171}Yb ($I = 1/2$, natural abundance 14.4%) and 173 ($I = 5/2$, 16.6%) that are barely distinguished in cLN, were well resolved in LN_K (see Figures 22 and 23). The dominant Yb_1 line that represents even isotopes with $I = 0$ (^{even}Yb, 69%) was described with $g_\parallel = 4.46$, $g_\perp = 2.706$. Intensities of the Yb^{3+} lines were proportional to natural abundances of isotopes and their spins: $\mathcal{I}(even):\mathcal{I}(171):\mathcal{I}(173) = 0.69:0.144/2:0.166/6 = 0.69:0.072:0.028$. It was found for Yb_1 that $^{171}A_\parallel = 0.119$ cm^{-1}, and $^{171}A_\perp = 0.0715$ cm^{-1}. Branches of angular dependencies of the Yb_5 center (fuchsia lines on Figure 22) were described with spin-Hamiltonian for $S = 1$ and anisotropic $S^A J S^B$ interaction ($J_{ik} \approx 0.012$–0.066 cm^{-1}). They were assigned to low-symmetry Yb^{3+}–Yb^{3+} pairs. The presence of additional lines of hyperfine structure with similar angular dependence (indicated by red arrows in Figure 23) supports the assignment, as their intensities are proportional to probabilities to meet two ^{even}Yb, or one ^{even}Yb and one ^{171}Yb, or one ^{even}Yb and one ^{173}Yb in such pairs. A self-compensated pair consisted of Me^{3+}_{Li} and Me^{3+}_{Nb} in the nearest sites (Nb shell 1 at a distance 0.3 nm on the crystal axis, Figure 5a) creates an axial center with rather strong exchange interaction ($J_{iso} > 300$ cm^{-1}). Therefore, the observed low-symmetry pairs were attributed to the Yb^{3+}–Yb^{3+} ions in next neighbor or next-next neighbor positions (shells 2 and 3 on Figure 5a).

One of the satellite centers (Yb_6) has axial symmetry; all others are low-symmetry centers. ENDOR measurements has revealed that Yb^{3+} substitutes for Li: at the first, comparison of measured angular dependencies with calculated ones on the base of dipole-dipole interactions (Equation (3)) gave undisputable preference for Li site, and at the second, the strongest axial hyperfine interaction was found for ^{93}Nb on the **z**-axis (the first shell on Figure 5a). The most reasonable explanation for the existence of the whole family of ytterbium centers is that Yb^{3+}_{Li} is compensated by one or two v_{Li} in different configurations.
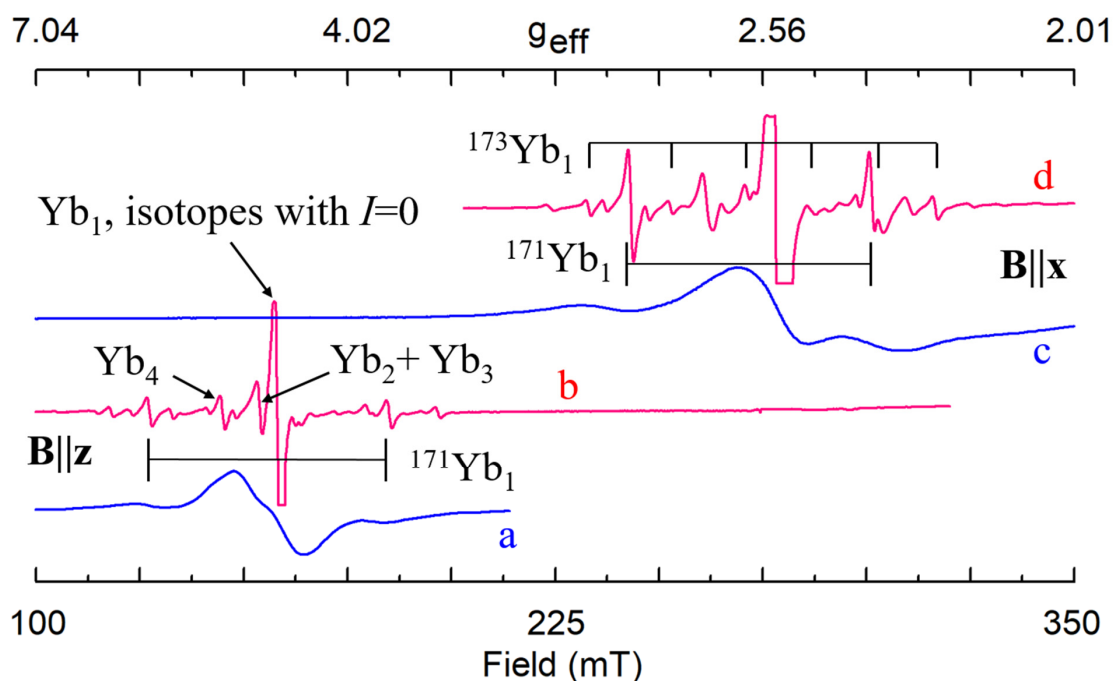
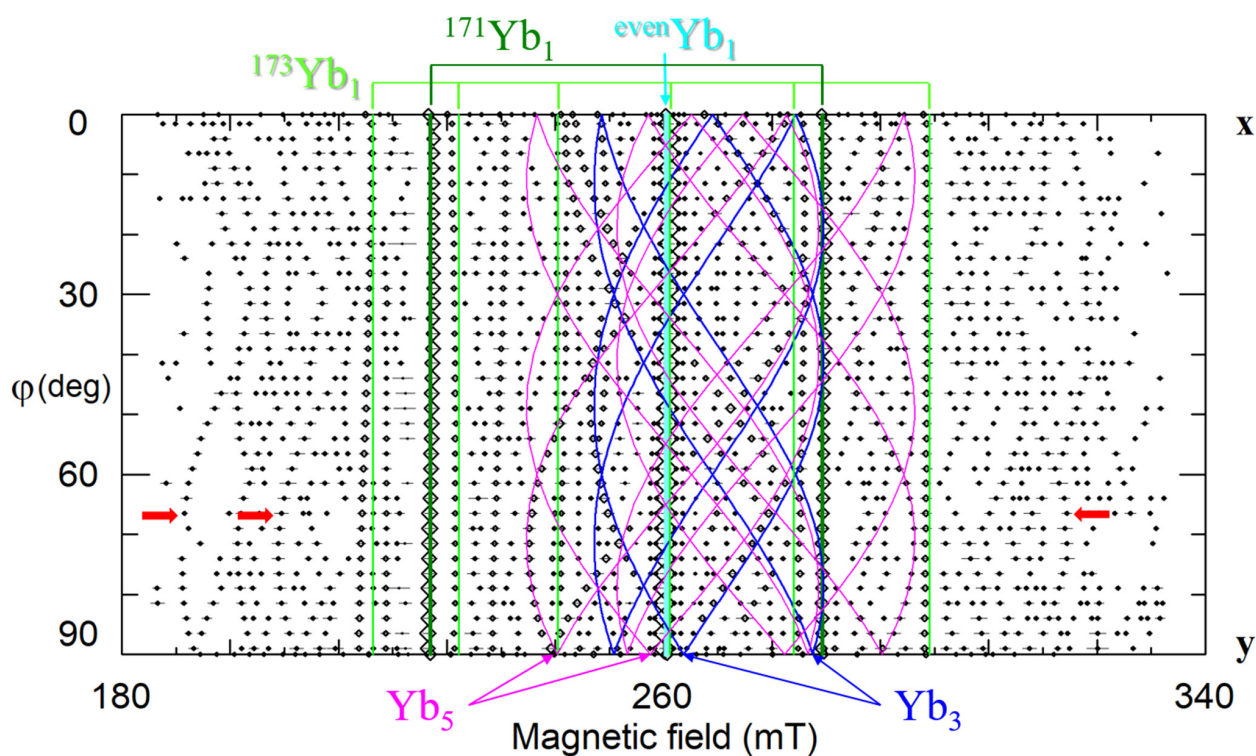**Figure 22.** EPR spectra of Yb^{3+} in congruent (a, c) and stoichiometric (b, d) LN.

Figure 23. Angular dependence of EPR spectra of Yb^{3+} in stoichiometric LN, **xy** plane, $\nu = 9.86$ GHz. Red arrows—lines of hyperfine structure for Yb_5 centers.

4.4. Tetra-, Penta- and Heptavalent Cations

The non-paramagnetic tetravalent impurities (C and Si) are always present in LN in rather high concentrations (about 50–500 ppm). Since determined concentrations of chlorine Cl (50–500 ppm) and manganese Mg (1–100 ppm) have the same order of magnitudes, no other charge compensators are necessary if C or Si substitutes for Nb creating $C^{4+}{}_{Nb}$ – $Cl^-{}_O{}^{2-}$ or $C^{4+}{}_{Nb}$ – $Mg^{2+}{}_{Li}$. The additional possibilities for the charge compensation supply H^+ and $Li^+{}_v$ ions. It is supposed that Ti^{4+} substitutes for Nb^{5+}; however, at present a mechanism of its charge compensation is not well established.

Due to the lithium deficiency of congruent lithium niobate crystals, v_{Li} have been considered as possible charge compensators for $Nb^{5+}{}_{Li}{}^+$ or $Ta^{5+}{}_{Li}{}^+$ antisites for a long time. Models with plane and space configurations of v_{Li} for non-stoichiometric defects were proposed [96,97] and used for calculations of stability of intrinsic defects and defect clusters in LN [250–253] and LN:Mg [254]. The antisites become paramagnetic ions $Nb^{4+}{}_{Li}{}^+$ or $Ta^{4+}{}_{Li}{}^+$ after irradiation (see Section 4.5 below).

The Ta^{5+} substitution for Nb^{5+} in LN causes minor lattice distortions only. The heptavalent ions (Mo, W) probably substitute for Nb^{5+} having lithium vacancies as charge compensators.

$\mathbf{U^{5+}}$ ($5f^1$). EPR spectra of U^{5+} were studied in $LiNbO_3$ powders doped with natural U_3O_8 and $^{233}U_3O_8$. A hyperfine sextet of EPR line for ^{233}U ($I = 5/2$) was described with $A_\parallel = 0.0145$ and $A_\perp = 0.0128$ cm^{-1}. $g_\parallel = 0.71$, $g_\perp = 0.724$ were determined for the line of natural U^{5+} (even isotopes with $I = 0$ have total natural abundance about 99%). It was observed that U^{5+} takes part in photoinduced valence change which is the basic mechanism for photorefraction.

4.5. Radiation and Reduction Defects

A radiation usually recharges of regular lattice, interstitial and impurity ions or produces interstitial ions. Two kinds of recharged defects were observed in LN: electron traps like Nb^{4+} and hole traps like O^- ions [236,255,256].

$\mathbf{Nb^{4+}}$ ($4d^1$). Hyperfine interaction of the unpaired $4d^1$ electron with the ^{93}Nb nuclear spin $I = 9/2$ splits its EPR line into ten components. The ten-line EPR spectrum ($g_\parallel = 1.90$ and $g_\perp = 1.72$) has been described for congruent $LiNbO_3$ after ionizing radiation [257]. Later this spectrum has been reproduced in vacuum-reduced and UV bleached crystals [258–261] (Figure 24, 1) and ascribed to antisite Nb [255]). It is remarkable that at least part of the Nb^{4+} centers has C_1 symmetry [262], although the main possible positions for Nb (regular Nb and Li site, v_{oct}) have C_3 symmetry. It means that compensating defects for Nb^{4+}, most probably lithium vacancies, are located in the nearest neighborhood (Figure 25a,b).

Similar spectra were observed in $LiNbO_3$ doped with 6 mol.% Mg (Figure 24, 2) after X-irradiation or vacuum reduction treatments and were related to Nb^{4+} centers on niobium sites [104,113,114], obviously with nearby defects. The Nb^{4+} center in $LiNbO_3$ doped with 10 mol.% Mg belongs to Nb in regular position, but with $Mg^{2+}{}_{Li}$ in neighborhood (Figure 24, 3) [238,263]. The neighboring Mg^{2+} ion redistributes a cloud of Nb^{4+} electrons and changes the hyperfine splitting.
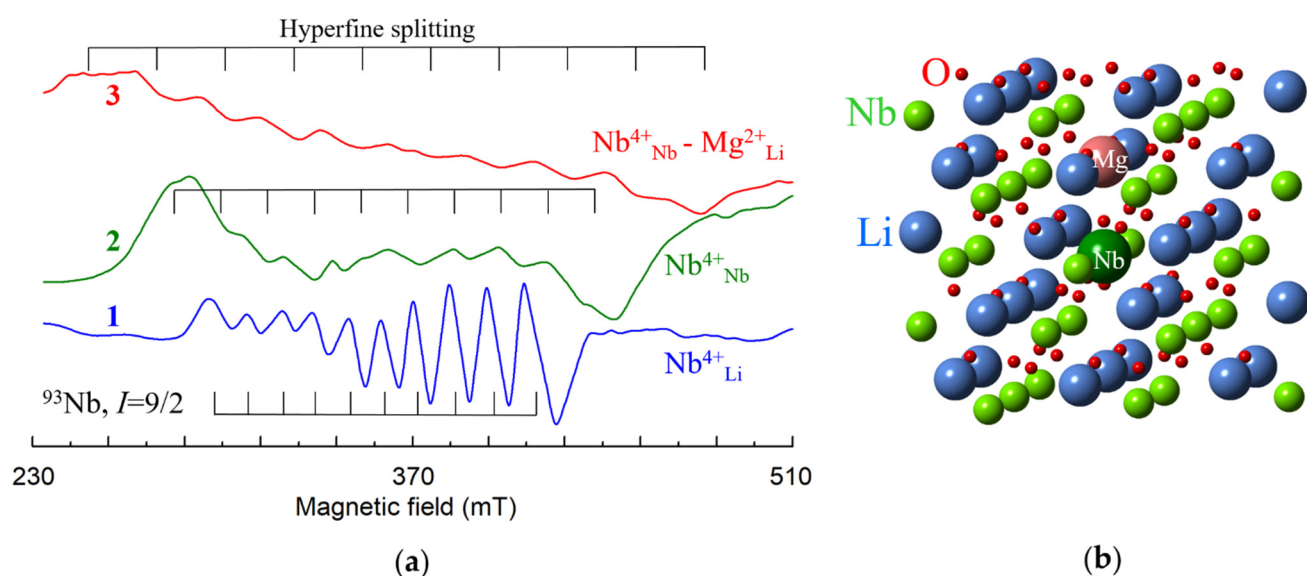
Figure 24. (**a**) EPR spectra of Nb^{4+} centers in cLN (1) and cLN doped with 6 mol.% Mg (2) and 10 mol.% Mg (3), X band. (**b**) Model for axial Nb^{4+}_{Nb} – Mg^{2+}_{Li} center.

Ta^{4+} (5d^1). The isotope ^{181}Ta has $I = 7/2$ and 100% natural abundance. The eight-line axial EPR spectrum with $g_{\parallel} = 1.503$ and $g_{\perp} = 1.172$, $A_{\parallel} = 0.0023$, and $A_{\perp} = 0.0234$ cm^{-1} has been observed in LiTaO$_3$ after reduction in argon and attributed to axial Ta^{4+}_{Li} [257]. Other ways to obtain Ta^{4+} are an irradiation of as-grown crystals with X-rays or optical bleaching of crystals that had been previously reduced [264]. A possible model for axial Ta^{4+} center is similar to the presented on Figure 25a.
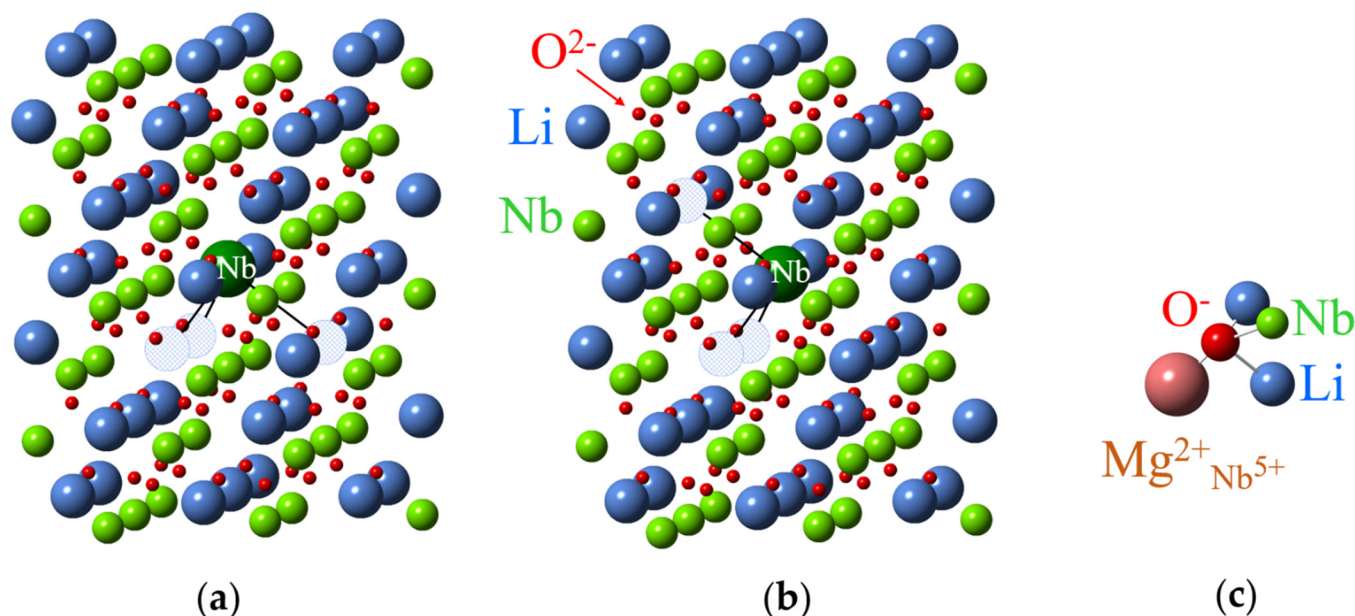
Figure 25. Models for Nb^{4+}_{Li} (large green ball) centers with three v_{Li} in LN. Hatched circles represent lithium vacancies. (**a**) Axial center. (**b**) Low-symmetry center. (**c**) The center with O^- near Mg^{2+} substituted for Nb^{5+}.

Tb^{4+} (4f^7). EPR study at 15 K revealed a signal of $g \approx 2.0$ appearing after UV irradiation with a simultaneous decrease in the Fe^{3+} signal intensity in near-stoichiometric LiNbO$_3$:Tb and LiNbO$_3$:Tb:Fe [265]. This implies that the Fe^{3+} ions act as electron traps. Irradiation by UV light induced an absorption band extending from $\lambda \approx 650$ nm to the absorption edge caused by the charge transfer from UV-sensitive absorption centers to Fe^{3+} ions via the conduction band.

Other electron and hole traps. A trapped-hole center with $S = 1/2$ was produced in $LiNbO_3$ by ionizing radiation [266]. Its ESR spectrum contains at least 26 equally spaced lines with 1.54 mT separation at $\mathbf{B} || \mathbf{z}$. This hyperfine pattern was explained as one "hole" interacting equally with three ^{93}Nb nuclei ($I = 9/2$ and 100% abundant). The hole is equally shared by three equivalent oxygen ions adjacent to a cation vacancy. A center with 25 lines of hyperfine interaction with two ^7Li and two ^{93}Nb nuclei was ascribed to O^- in regular O^{2-} site with unclear stabilizing factor for the hole trap [236].

An OH^{2-} ion was identified in undoped and weakly doped with Mg LN samples after γ-irradiation and subsequent partial UV bleaching [109]. Specific hyperfine structure with ^{93}Nb was observed for a hole trap in LN doped with 6–8 mol.% Mg. The center was attributed to O^- near Mg^{2+} ion substituted for Nb^{5+} (Figure 25c) [263].

5. Impurity Identification

At an investigation of a sample grown from a melt with an addition of a paramagnetic spice in concentration 0.00X–0.X at.%, which warrants that EPR signal significantly exceeds noise, it would be reasonable to expect EPR signal from this spice. Often, studied samples (especially, commercial ones) contain so-called non-controlled or trace impurities like Cr, Mn, Fe, Cu etc. in a slightly smaller or comparable concentration. Fortunately, most paramagnetic impurities are already investigated by EPR/ENDOR techniques and their characteristics—electron and nuclear spins, zero-field splitting, hyperfine and quadrupole interactions, kinds of charge compensators and their locations, i.e., "passports" of the impurities—are known. Comparison of published and observed spectra (see, for instance, figures with EPR spectra and their angular dependencies above) allows to identify the impurities in films, epitaxial layers, and fibers, or to evaluate profile of impurity distribution in bulk samples. Spectra of LN/LT powders and ceramics can be simulated using determined spin-Hamiltonian parameters.

6. Conclusions

Very detailed information about structures of impurity defects (charge state, point symmetry, hyperfine interactions with neighbor nuclei, charge compensation mechanisms etc.) was obtained with the help of EPR and ENDOR.

The necessity of a charge compensation for non-isovalent substitution usually leads to the creation of families of electrically and magnetically non-equivalent impurity centers. The families of satellite centers exist due to the different relative locations of the impurity ion and its charge compensator. Two or more different centers were observed for Co^{2+}, Cr^{3+}, Cu^{2+}, Er^{3+}, Fe^{3+}, Gd^{3+}, Mn^{2+}, Nd^{3+}, Yb^{3+}, and other ions. Since the relative concentrations of satellite centers are comparable with the concentration of the main center, both kinds of centers generally are equally responsible for many of the properties of LN/LT crystals, and they should both be taken into consideration, especially in non-stoichiometric crystals.

Several different mechanisms for a compensation of excessive charge of Me impurity were found:

- the compensation by nonstoichiometric defects (v_{Li}, v_{Nb}) for small concentrations of Me_{Li} in crystals,
- the partial self-compensation of charges of Me_{Li} by Me_{Nb} mainly for the Me_{Li} concentration that exceeds the concentration of v_{Li},
- the partial compensation of Me_{Nb} by interstitial Li^+ in v_{oct},
- the compensation by other impurities (H, co-dopants like Mg, Zn, etc.).

The presence of non-stoichiometric defects is one of the reasons why LN tolerates a strong incorporation of dopants non-isovalent to Li^+ and Nb^{5+}. As long as the impurity concentration [Me] is smaller than $\delta x_C = |50\% - x_C|$, the number of intrinsic defects is large enough to compensate the corresponding charge excess. However, for stoichiometric or nearly stoichiometric samples with high impurity concentrations (when [Me] > δx_C) and with the lack of charge compensators a decrease of the distribution coefficient of impurities is observed in comparison with congruent material. A further increase of the [Me]/δx_C

ratio up to [Me] >> δx_C can result in a change of the charge compensation mechanism. This can reveal itself in the appearance of new impurity centers.

The charge compensation by v_{Li} works well for most of the non-isovalent ions. Vacancies in the nearest neighborhood of Me_{Li} decrease symmetry of centers from C_3 to C_1, whereas distant vacancies cause spectral line broadening. For $Me^{3+}_{Nb/Ta}$ in stoichiometric LN/LT the charge compensation by interstitial H^+ and Li^+_v ions was found. The interstitial Li^+_v should be considered as a concurrent charge compensation mechanism in VTE treated samples. The compensation of Me_{Nb} by Mg_{Li}, Zn_{Li} and other impurities occurs when the co-dopant concentration exceeds some threshold that depends on δx_C. Typically, the threshold is about 6–8% for congruent samples, but it is lower than 1% for nearly stoichiometric samples.

The use of stoichiometric or nearly stoichiometric crystals with $\delta x_C \approx 0$ presents many advantages for the investigation of impurity centers by spectroscopic techniques. The decreased concentration of intrinsic defects causes a tremendous narrowing of the spectral lines. This is accompanied with the increase of spectral resolution and sensitivity, facilitates the analysis of the spectra, and simplifies the interpretation of the data. However, together with the disappearance of intrinsic defects the satellite centers disappear also. For a detailed investigation of such additional centers, the crystals with high $x_C \approx 49.5$–49.85% are more suitable than others: they have more narrow spectral lines than congruent samples, but the satellite centers are still present. Further study of nearly stoichiometric and stoichiometric LN and LT samples should help to eliminate some disagreements in published data and to clarify intimate details of structures of impurity defects in materials, which are important for both physics and applications.

Derived structures and obtained by EPR/ENDOR characteristics of Zeeman and zero-field splitting, quadrupole and hyperfine interactions of impurity electrons with own and surrounding nuclei can be reliable corner stones for modelling of the structures.

Author Contributions: V.G.G.—theorist (yin), and G.I.M.—experimentalist (yang) made inseparable complementary contributions. All authors have read and agreed to the published version of the manuscript.

Institutional Review Board Statement: Not applicable.

Informed Consent Statement: Not applicable.

Data Availability Statement: The data presented in this study are available on request from the corresponding author.

Conflicts of Interest: The authors declare no conflict of interest.

References

1. Räuber, A. Chemistry and Physics of Lithium Niobate. In *Current Topics in Materials Science*, 1st ed.; Kaldis, E., Ed.; North-Holland: Amsterdam, The Netherlands, 1978; Volume 1, pp. 481–601.
2. Volk, T.; Wöhlecke, M. Point defects in LiNbO$_3$. In *Lithium Niobate. Defects, Photorefraction and Ferroelectric Switching*, 1st ed.; Hull, R., Osgood, R.M., Jr., Parisi, J., Warlimont, H., Eds.; Springer Series in Materials Science; Springer: Berlin/Heidelberg, Germany, 2009; Volume 115, pp. 1–50.
3. Ilyenkov, A.V.; Khiznyak, A.I.; Kreminskaya, L.V.; Soskin, M.S.; Vasnetsov, M.V. Birth and evolution of wave-front dislocations in a laser beam passed through a photorefractive LiNbO$_3$: Fe crystal. *Appl. Phys. B* **1996**, *62*, 465–471. [CrossRef]
4. Prokhorov, A.M.; Kuz'minov, Y.S. *Physics and Chemistry of Crystalline Lithium Niobate*; CRC Press: Boca Raton, FL, USA, 1990.
5. Wong, K.K. (Ed.) *Properties of Lithium Niobate*; EMIS Data Review Series No. 5; The Institution of Electrical Engineers, INSPEC: London, UK, 2002.
6. Toney, J.E. *Lithium Niobate Photonics*; Artech House Publishers: London, UK, 2015; pp. 1–265.
7. Streque, J.; Aubert, T.; Kokanyan, N.; Bartoli, F.; Taguett, A.; Polewczyk, V.; Kokanyan, E.; Hage-Ali, S.; Boulet, P.; Elmazria, O. Stoichiometric Lithium Niobate Crystals: Towards Identifiable Wireless Surface Acoustic Wave Sensors Operable up to 600 °C. *IEEE Sens. Lett.* **2019**, *3*, 2501204. [CrossRef]

8. Abrahams, S.C.; Reddy, J.M.; Bernstein, J.L. Ferroelectric lithium niobate. 3. Single crystal X-ray diffraction study at 24 °C. *J. Phys. Chem. Solids* **1966**, *27*, 997–1012. [CrossRef]

9. Peterson, G.E.; Bridenbaugh, P.M.; Green, P. NMR Study of Ferroelectric LiNbO$_3$ and LiTaO$_3$. *J. Chem. Phys.* **1967**, *46*, 4009–4014. [CrossRef]

10. Vianden, R. Hyperfine techniques for defects studies. In *Insulating Materials for Optoelectronics. New Developments*; Agulló-López, F., Ed.; World Scientific Publishing: Singapore; Hackensack, NJ, USA; London, UK; Hong Kong, China, 1995; pp. 125–146.

11. Kling, A.; Soares, J.C.; da Silva, M.F. Channeling Investigation of Oxide materials for Optoelectronic Applications. In *Insulating Materials for Optoelectronics. New Development*; Agulló-López, F., Ed.; World Scientific Publishing: Singapore; Hackensack, NJ, USA; London, UK; Hong Kong, China, 1995; pp. 175–200.

12. Gog, T.; Marerlik, G. X-ray Standing Wave Determination of Lattice Positions of Impurities in Lithium Niobate. In *Insulating Materials for Optoelectronics. New Developments*; Agulló-López, F., Ed.; World Scientific Publishing: Singapore; Hackensack, NJ, USA; London, UK; Hong Kong, China, 1995; pp. 201–220.

13. Spaeth, J.-M.; Niklas, J.R.; Bartram, R.H. *Structural Analysis of Point Defects in Solids: An Introduction to Multiple Magnetic Resonance Spectroscopy*; Springer: Singapore, 1992; pp. 1–367.

14. Prieto, C. Influence of lithium niobate stoichiometry on the lattice position of Nd^{3+} in Nd:LiNbO$_3$. *Opt. Mater.* **1999**, *12*, 135–142. [CrossRef]

15. Lorenzo, A.; Jaffrezic, H.; Roux, B.; Boulon, G.; Garcia-Sole, J. Lattice location of rare-earth ions in LiNbO$_3$. *Appl. Phys. Lett.* **1995**, *67*, 3735–3737. [CrossRef]

16. Lorenzo, A.; Loro, H.; Muñoz Santiuste, J.E.; Terrile, M.C.; Boulon, G.; Bausa, L.E.; Garcia Sole, J. RBS/channeling to locate active ions in laser materials: Application to rare earth activated LiNbO$_3$. *Opt. Mater.* **1997**, *8*, 55–63. [CrossRef]

17. Rebouta, L.; Smulders, P.J.M.; Boerma, D.O.; Agullo-Lopez, F.; da Silva, M.F.; Soares, J.C. Ion-beam channeling yields of host and impurity atoms in LiNbO$_3$: Computer simulations. *Phys. Rev. B* **1993**, *48*, 3600–3610. [CrossRef]

18. Rebouta, L.; da Silva, M.F.; Soares, J.C.; Santos, M.T.; Dieguez, E.; Agulló-López, F. Ion-beam/channeling characterization of LiNbO$_3$: Interaction between impurity sites. *Opt. Mater.* **1995**, *4*, 174–178. [CrossRef]

19. Garcia Sole, J.; Petith, T.; Jaffrez, H.; Boulon, G. Lattice Location of the Non-Equivalent Nd^{3+} Ions in LiNbO$_3$: Nd and LiNbO$_3$: MgO:Nd. *Europhys. Lett.* **1993**, *24*, 719–724. [CrossRef]

20. Vila, M.; de Bernabe, A.; Prieto, C. EXAFS determination of the Nd lattice position in Nd:LiNbO$_3$: Influence of lithium niobate stoichiometry and Mg and Zn co-doping. *J. Alloys Compd.* **2001**, *323–324*, 331–335. [CrossRef]

21. Catlow, C.R.A.; Chadwick, A.V.; Cole, M.; Tomlinson, S.M. An EXAFS study of dopant substitution in LiNbO$_3$ and LiTaO$_3$. *Radiat. Eff. Defects Solids* **1991**, *119–121*, 565–570. [CrossRef]

22. Bush, T.S.; Catlow, C.R.A.; Chadwick, A.V.; Cole, M.; Geatches, R.M.; Greaves, G.N.; Tomlinson, S.M. Studies of cation dopant sites in metal oxides by EXAFS and computer-simulation techniques. *J. Mater. Chem.* **1992**, *2*, 309–316. [CrossRef]

23. Prieto, C.; Zaldo, C. Determination of the lattice site of Fe in photorefractive LiNbO$_3$. *Solid State Commun.* **1992**, *83*, 819–821. [CrossRef]

24. Zaldo, C.; Prieto, C. Lattice site of transition metal and rare-earth impurities in LiNbO$_3$ single crystals: An exafs study. *Ferroelectrics* **1992**, *134*, 47–51. [CrossRef]

25. Corradi, G.; Chadwick, A.V.; West, A.R.; Cruickshankand, K.; Paul, M. On the substitution site of Cr and Fe in LiNbO$_3$: An exafs study. *Radiat. Eff. Defects Solids* **1995**, *134*, 219–222. [CrossRef]

26. Sanson, A.; Zaltron, A.; Argiolas, N.; Sada, C.; Bazzan, M.; Schmidt, W.G.; Sanna, S. Polaronic deformation at the Fe$^{2+/3+}$ impurity site in Fe:LiNbO$_3$ crystals. *Phys. Rev. B* **2015**, *91*, 094109. [CrossRef]

27. Rebouta, L.; da Silva, M.F.; Soares, J.C.; Hage-Ali, M.; Stoquert, J.P.; Siffert, P.; Sanz-García, J.A.; Diéguez, E.; Agulló-López, F. Lattice Site of Iron in LiNbO$_3$(Fe^{3+}) by the PIXE/Channelling Technique. *Europhys. Lett.* **1991**, *14*, 557–561. [CrossRef]

28. Gog, T.; Schotters, P.; Falta, J.; Materlik, G.; Grodzicki, M. The lattice position of Fe in Fe-doped LiNbO$_3$. *J. Phys. Condens. Matter* **1995**, *7*, 6971–6980. [CrossRef]

29. Marques, J.G.; Kling, A.; Soares, J.C.; Rebouta, L.; da Silva, M.F.; Diéguez, E.; Agulló-López, F. Lattice site location of Hf in LiNbO$_3$: Influence of dopant concentration and crystal stoichiometry. *Nucl. Instrum. Methods Phys. Res. B* **1998**, *136–138*, 431–435. [CrossRef]

30. Mignotte, C. Determination of lattice site locations of erbium ions implanted into LiNbO$_3$ single crystals after annealing at moderate and high temperature. *Appl. Surf. Sci.* **2001**, *185*, 11–26. [CrossRef]

31. Kovacs, L.; Rebouta, L.; Soaresh, J.C.; da Silva, M.F.; Hage-Ali, M.; Stoquert, J.P.; Siffert, P.; Sanz-Garcia, J.A.; Corradi, G.; Szaller, Z. On the lattice site of trivalent dopants and the structure of Mg^{2+}-OH$^-$-M^{3+} defects in LiNbO$_3$:Mg crystals. *J. Phys. Condens. Matter* **1993**, *5*, 781–794. [CrossRef]

32. Kling, A.; Soares, J.C.; da Silva, M.F.; Sanz-Garcia, J.A.; Dieguez, E.; Agullo-Lopez, F. Lattice site determination of Cr in low doped lithium niobate single crystals using PIXE/channeling. *Nucl. Instrum. Methods Phys. Res. B* **1998**, *136–138*, 426–430. [CrossRef]

33. Engelmann, H.; Mouahid, F.; Dezsi, I.; Molnar, B.; Gonser, U.; Siebert, D.; Dahlem, J.; Tuczek, F. Mössbauer and ESR study of LiNbO$_3$-Fe$_2$O$_3$ for low Fe$_2$O$_3$ concentrations. *Appl. Phys. A* **1989**, *48*, 211–217. [CrossRef]

34. Tomov, T.; Engelmann, H.; Dezci, I.; Gonser, U. Investigation of the ferroelectric phase transition in LiNbO$_3$: Fe by Mössbauer spectroscopy. *Solid State Commun.* **1989**, *69*, 41–44. [CrossRef]
35. Mignoni, S.; Fontana, M.D.; Bazzan, M.; Ciampolillo, M.V.; Zaltron, A.M.; Argiolas, N.; Sada, C. Micro-Raman analysis of Fe-diffused lithium niobate waveguides. *Appl. Phys. B* **2010**, *101*, 541. [CrossRef]
36. Kamińska, A.; Suchocki, A.; Kobyakov, S.; Arizmendi, L.; Potemski, M.; Teran, F.J. High-pressure and magneto-optical studies of Cr-related defects in the lithium-rich LiNbO$_3$:Cr, Mg crystal. *Phys. Rev. B* **2007**, *76*, 144117. [CrossRef]
37. Basun, S.; Kaplyanskii, A.; Kutsenko, A.; Dierolf, V.; Troester, T.; Kapphan, S.E.; Polgar, K. Optical characterization of Cr^{3+} centers in LiNbO$_3$. *Appl. Phys. B* **2001**, *73*, 453–461. [CrossRef]
38. Sothe, H.; Rowan, L.G.; Spaeth, J.-M. Sites of Fe^{3+} impurities in a congruent LiTaO$_3$ crystal. *J. Phys. Condens. Matter* **1989**, *1*, 3591–3600. [CrossRef]
39. Sothe, H.; Spaeth, J.-M. The site and local environment of Fe^{3+} in LiNbO$_3$ investigated with ENDOR. *J. Phys. Condens. Matter* **1992**, *4*, 9901–9906. [CrossRef]
40. Spaeth, J.-M. Determination of atomic positions of point defects in solids by ENDOR. *Appl. Magn. Reson.* **1992**, *3*, 257–281. [CrossRef]
41. Lerner, P.; Legras, C.; Dumas, J.P. Stoechiometrie des monocristaux de metaniobate de lithium. *J. Cryst. Growth* **1968**, *3*, 231–235. [CrossRef]
42. Byer, R.L.; Young, J.F.; Feigelson, R.S. Growth of High-Quality LiNbO$_3$ Crystals from the Congruent Melt. *J. Appl. Phys.* **1970**, *41*, 2320–2325. [CrossRef]
43. Malovichko, G.I.; Grachev, V.G.; Gabrielyan, V.T.; Kokanyan, E.P. Widths and intensities of ESR lines of iron-group impurities in nonstoichiometric lithium niobate crystals. *Sov. Phys. Solid State* **1986**, *28*, 1453–1458.
44. Iyi, N.; Kitamura, K.; Izumi, F.; Yamamoto, J.; Hayashi, T.; Asano, H.; Kimura, S. Comparative of defect structures in lithium niobate with different compositions. *J. Solid State Chem.* **1992**, *101*, 340–352. [CrossRef]
45. Holman, R.L. *Processing of Crystalline Ceramics*; Palmour, H., Davis, R.F., Eds.; Plenum: New York, NY, USA, 1978; p. 343.
46. Jundt, D.H.; Fejer, M.M.; Byer, R.L. Optical properties of lithium-rich lithium niobate fabricated by vapor transport equilibration. *IEEE J. Quantum Electron.* **1990**, *26*, 135–138. [CrossRef]
47. Bordui, P.F.; Norwood, R.G.; Bird, C.D.; Calvert, G.D. Compositional uniformity in growth and poling of large-diameter lithium niobate crystals. *J. Cryst. Growth* **1991**, *113*, 61–68. [CrossRef]
48. Bordui, P.F.; Norwood, R.G.; Jundt, D.H.; Fejer, M.M. Preparation and characterization of off-congruent lithium niobate crystals. *J. Appl. Phys.* **1992**, *71*, 875–879. [CrossRef]
49. Jundt, D.H.; Fejer, M.M.; Norwood, R.G.; Bordui, P.F. Composition dependence of lithium diffusivity in lithium niobate at high temperature. *J. Appl. Phys.* **1992**, *72*, 3468–3473. [CrossRef]
50. Fischer, C.; Kapphan, S.; Feng, X.-Q.; Cheng, N. Sharp R-lines in absorption and emission of Cr^{3+} in stoichiometric (VTE) LiNbO$_3$. *Radiat. Eff. Defects Solids* **1995**, *135*, 199–202. [CrossRef]
51. Furukawa, Y.; Sato, M.; Kitamura, K.; Yajima, Y.; Minakata, M. Optical damage resistance and crystal quality of LiNbO$_3$ single crystals with various [Li]/[Nb] ratios. *J. Appl. Phys.* **1992**, *72*, 3250–3254. [CrossRef]
52. Kitamura, K.; Yamamoto, J.; Iyi, N.; Kirnura, S.; Hayashi, T. Stoichiometric LiNbO$_3$ single crystal growth by double crucible Czochralski method using automatic powder supply system. *J. Cryst. Growth* **1992**, *116*, 327–332. [CrossRef]
53. Kitamura, K.; Furukawa, Y.; Iyi, N. Progress in single crystal growth of LiNbO$_3$ using double crucible Czochralski method. *Ferroelectrics* **1997**, *202*, 21–28. [CrossRef]
54. Kitamura, K.; Furukawa, Y.; Ji, Y.; Zgonik, M.; Medrano, C.; Montemezzani, G.; Guenter, P. Photorefractive effect in LiNbO$_3$ crystals enhanced by stoichiometry control. *J. Appl. Phys.* **1997**, *82*, 1006–1009. [CrossRef]
55. Furukawa, Y.; Kitamura, K.; Suzuki, E.; Niwa, K. Stoichiometric LiTaO$_3$ single crystal growth by double crucible Czochralski method using automatic powder supply system. *J. Cryst. Growth* **1999**, *197*, 889–895. [CrossRef]
56. Malovichko, G.I.; Grachev, V.G.; Yurchenko, L.P.; Proshko, V.Y.; Kokanyan, E.P.; Gabrielyan, V.T. Improvement of LiNbO$_3$ microstructure by crystal growth with potassium. *Phys. Status Solidi (a)* **1992**, *133*, K29–K33. [CrossRef]
57. Malovichko, G.I.; Grachev, V.G.; Kokanyan, E.; Schirmer, O.F.; Betzler, K.; Gather, B.; Jermann, F.; Klauer, S.; Schlarb, U. Characterization of stoichiometric LiNbO$_3$ grown from melts containing K$_2$O. *Appl. Phys. A* **1993**, *56*, 103–108. [CrossRef]
58. Bermudez, V.; Dutta, P.S.; Serrano, M.D.; Dieguez, E. The effect of native defects on the domain structures of Fe—A case study by means of the addition of MgO and K$_2$O to the congruent melt. *J. Phys. Condens. Matter* **1997**, *9*, 6097–6101. [CrossRef]
59. Polgar, K.; Peter, A.; Kovacs, L.; Corradi, G.; Szaller, Z. Growth of stoichiometric LiNbO$_3$ single crystals by top seeded solution growth method. *J. Cryst. Growth* **1997**, *177*, 211–216. [CrossRef]
60. Balasanyan, R.N.; Vartanyan, E.S.; Gabrielyan, V.T.; Kazaryan, L.M. Method for Growing Lithium Niobate Single Crystals. Patent SU 845506 A1, 29 March 1979. Available online: https://www.elibrary.ru/item.asp?id=41087794 (accessed on 27 February 2000).
61. Serrano, M.D.; Bermudez, V.; Arizmendi, L.; Dieguez, E. Determination of the Li/Nb ratio in LiNbO$_3$ crystals grown by Czochralski method with K$_2$O added to the melt. *J. Cryst. Growth* **2000**, *210*, 670–675. [CrossRef]
62. Kokanyan, E.; Dieguez, E. New perspectives of lithium niobate crystals. *J. Optoelectron. Adv. Mater.* **2000**, *2*, 205–214.

63. Polgar, K.; Peter, A.; Foldvari, I.; Szaller, Z. Structural defects in flux-grown stoichiometric LiNbO$_3$ single crystals. *J. Cryst. Growth* **2000**, *218*, 327–333. [CrossRef]

64. Polgár, K.; Péter, Á.; Földvári, I. Crystal growth and stoichiometry of LiNbO$_3$ prepared by the flux method. *Opt. Mater.* **2002**, *19*, 7–11. [CrossRef]

65. Polgár, K.; Péter, Á.; Pöppl, L.; Ferriol, M.; Földvári, I. Chemical and thermal conditions for the formation of stoichiometric LiNbO$_3$. *J. Crystal Growth* **2002**, *237–239*, 682–686. [CrossRef]

66. Grunskij, O.S.; Denisov, A.V.; Badmaev, T.V. A Method for Growing Doped Crystals of Lithium Niobate with a Composition close to Stoichiometric, and a Device for Its Implementation. Patent RU 2367730 C2, 29 November 2007. Available online: https://www.elibrary.ru/item.asp?id=37690005 (accessed on 20 September 2009).

67. Lengyel, K.; Péter, Á.; Kovács, L.; Corradi, G.; Pálfalvi, L.; Hebling, J.; Unferdorben, M.; Dravecz, G.; Hajdara, I.; Szaller, Z.; et al. Growth, defect structure, and THz application of stoichiometric lithium niobate. *Appl. Phys. Rev.* **2015**, *2*, 040601. [CrossRef]

68. Malovichko, G.; Grachev, V.; Schirmer, O. Interrelation of intrinsic and extrinsic defects—Congruent, stoichiometric, and regularly ordered lithium niobate. *Appl. Phys. B* **1999**, *68*, 785–793. [CrossRef]

69. Malovichko, G.I.; Grachev, V.G.; Schirmer, O.F.; Faust, B. New axial Fe^{3+} centers in stoichiometric lithium niobate crystals. *J. Phys. Condens. Matter* **1993**, *5*, 3971–3976. [CrossRef]

70. de Bernabe, A.; Prieto, C.; de Andres, A. Effect of stoichiometry on the dynamic mechanical properties of LiNbO$_3$. *J. Appl. Phys.* **1995**, *79*, 143–148. [CrossRef]

71. Garret, M.H.; Mnushkina, I.; Furukawa, Y.; Kitamura, K.; Halliburton, L.E.; Giles, N.C.; Setzler, S.D. Photorefractive Properties of Iron-Doped Congruent Lithium Niobate, and Iron-Doped K$_2$O Flux Grown Stoichiometric Lithium Niobate. Proceedings of 1997 Topical Meeting on Photorefractive Materials, Effects and Devices, Chiba, Japan, 11–13 June 1997.

72. Abdi, F.; Aillerie, M.; Bourson, P.; Fontana, M.D.; Polgar, K. Electro-optic properties in pure LiNbO$_3$ crystals from the congruent to the stoichiometric composition. *J. Appl. Phys.* **1998**, *84*, 2251–2254. [CrossRef]

73. Choi, Y.N.; Choh, S.H.; Park, I.W.; Koh, E.K.; Kim, S.S. Characterization of Stoichiometry of LiNbO$_3$ Crystals by EPR and Raman Scattering Measurements. *J. Korean Phys. Soc.* **1998**, *32*, S643.

74. Malovichko, G. Nonstoichiometry as a powerful tool for photorefractive material optimization. Lithium Niobate Crystals. In *Advances in Photorefractive Materials, Effects and Devices*; Andersen, P.E., Johansen, P.M., Pedersen, H.C., Petersen, P.M., Saffman, M., Eds.; Trends in Optics and Photonics; Optical Society of America: Washington, DC, USA, 1999; Volume 27. [CrossRef]

75. Malovichko, G.; Petersen, R.; Bäuman, C.; Grachev, V. Second axial Fe^{3+} center in stoichiometric lithium tantalate. *J. Appl. Phys.* **2006**, *100*, 023911. [CrossRef]

76. Razdobarin, A.G.; Basun, S.A.; Bursian, V.É.; Sochava, L.S.; Evans, D.R. A Fe[Nb]-Li center in stoichiometric LiNbO$_3$ crystals: Mechanism of formation. *Phys. Solid State* **2010**, *52*, 706–711. [CrossRef]

77. Schlarb, U.; Klauer, S.; Wesselmann, M.; Betzler, K. Determination of the Li/Nb ratio in lithium niobate by means of birefringence and Raman measurements. *Appl. Phys. A* **1993**, *56*, 311–315. [CrossRef]

78. Kling, A.; Marques, J.G.; Correia, J.G.; da Silva, M.F.; Dieguez, E.; Agullo-Lopez, F.; Soares, J.C. Study of structural differences between stoichiometric and congruent lithium niobate. *Nucl. Instrum. Methods Phys. Res. B* **1996**, *113*, 293–295. [CrossRef]

79. Kovacs, L.; Ruschhaupt, G.; Polgar, K.; Corradi, G.; Woehlecke, M. Composition dependence of the ultraviolet absorption edge in lithium niobate. *Appl. Phys. Lett.* **1997**, *70*, 2801–2803. [CrossRef]

80. Dravecz, G.; Kovács, L. Determination of the crystal composition from the OH$^-$ vibrational spectrum in lithium niobate. *Appl. Phys. B* **2007**, *88*, 305–307. [CrossRef]

81. Grachev, V.G. Visual EPR, Visual ENDOR Packages, Version 20.11. Available online: www.visual-epr.com (accessed on 1 June 2013).

82. *CrystalMaker Program, Version 2.7.7*; CrystalMaker Software Ltd.: Oxford, UK; Available online: www.crystalmaker.com (accessed on 31 December 2011).

83. Boysen, H.; Altorfer, F. A neutron powder investigation of the high-temperature structure and phase transition in LiNbO$_3$. *Acta Crystallogr. B* **1994**, *50*, 405–414. [CrossRef]

84. Hsu, R.; Maslen, E.N.; du Boulay, D.; Ishizawa, N. Synchrotron X-ray Studies of LiNbO$_3$ and LiTaO$_3$. *Acta Crystallogr. B* **1997**, *53*, 420–428. [CrossRef]

85. Malovichko, G.; Cerclier, O.; Estienne, J.; Grachev, V.; Kokanyan, E.; Boulesteix, C. Lattice constants of K- and Mg-doped LiNbO$_3$. Comparison with nonstoichiometric lithium niobate. *J. Phys. Chem. Sol.* **1995**, *56*, 1285–1289. [CrossRef]

86. Lehnen, H.; Boysen, H.; Frey, F.; Hewat, A.; Radaelli, P. A neutron powder investigation of the high-temperature structure and phase transition in stoichiometric LiNbO$_3$. *Zeitschrift für Kristallographie* **1997**, *212*, 712–719. [CrossRef]

87. Malovichko, G.; Grachev, V.; Kokanyan, E.; Schirmer, O. Axial and low-symmetry centers of trivalent impurities in lithium niobate. Chromium in congruent and stoichiometric crystals. *Phys. Rev. B* **1999**, *59*, 9113–9125. [CrossRef]

88. Abrahams, S.C.; Hamilton, W.C.; Reddy, J.M. Ferroelectric lithium niobate. 4. Single crystal neutron diffraction study at 24 °C. *J. Phys. Chem. Solids* **1966**, *27*, 1013–1018. [CrossRef]

89. Megaw, H.D. A note on the structure of lithium niobate, LiNbO$_3$. *Acta Crystallogr. A* **1968**, *24*, 583–588. [CrossRef]

90. Abrahams, S.C.; Levinstein, H.J.; Reddy, J.M. Ferroelectric lithium niobate. 5. Polycrystal X-ray diffraction study between 24° and 1200 °C. *J. Phys. Chem. Solids* **1966**, *27*, 1019–1026. [CrossRef]

91. Malovichko, G.; Grachev, V.; Okulov, S.; Kokanyan, E.; Henecker, F.; Hofstaetter, A.; Schirmer, O. EPR of Nd^{3+} in congruent and nearly stoichiometric lithium niobate. *Phys. Status Solidi (b)* **2005**, *243*, 1–7. [CrossRef]

92. Malovichko, G.; Bratus, V.; Munro, M.; Kokanyan, E.; Okulov, S.; Grachev, V. Multifrequency spectroscopy of laser active centers Nd^{3+} and Yb^{3+} in nearly stoichiometric $LiNbO_3$. *Phys. Status Solidi (c)* **2007**, *4*, 1346–1351. [CrossRef]

93. Grachev, V.; Munro, M.; Kokanyan, E.; Malovichko, G. Determination of g-tensors of low-symmetry Nd^{3+} centers in $LiNbO_3$ by rectification of angular dependence of electron paramagnetic resonance spectra. *J. Appl. Phys.* **2015**, *118*, 044103. [CrossRef]

94. Blümel, J.; Born, E.; Metzger, T. Solid state NMR study supporting the lithium vacancy defect model in congruent lithium niobate. *J. Phys. Chem. Solids* **1994**, *55*, 589–593. [CrossRef]

95. Zotov, N.; Boysen, H.; Frey, F.; Metzger, T.; Born, E. Cation substitution models of congruent $LiNbO_3$ investigated by X-ray and neutron powder diffraction. *J. Phys. Chem. Solids* **1994**, *55*, 145–152. [CrossRef]

96. Leroux, C.; Nihoul, G.; Malovichko, G.; Grachev, V.; Boulesteix, C. High resolution electron microscopy investigation of correlated defects in non-stoichiometric lithium niobate. *J. Phys. Chem. Solids* **1998**, *59*, 311–319. [CrossRef]

97. Kim, S.; Gopalan, V.; Kitamura, K.; Furukawa, Y. Domain reversal and nonstoichiometry in lithium tantalate. *J. Appl. Phys.* **2001**, *90*, 2949–2963. [CrossRef]

98. Abrahams, S.C.; Marsh, P. Defect structure dependence on composition in lithium niobate. *Acta Crystallogr. B* **1986**, *42*, 61–68. [CrossRef]

99. Peterson, G.E.; Carnevale, A. ^{93}Nb NMR linewidths in nonstoichiometric lithium niobate. *J. Chem. Phys.* **1972**, *56*, 4648–4851. [CrossRef]

100. Araujo, R.M.; dos Santos Mattos, E.F.; Valerio, M.E.G.; Jackson, R.A. Computer Simulation of the Incorporation of V^{2+}, V^{3+}, V^{4+}, V^{5+} and Mo^{3+}, Mo^{4+}, Mo^{5+}, Mo^{6+} Dopants in $LiNbO_3$. *Crystals* **2020**, *10*, 457. [CrossRef]

101. Kuzminov, Y.; Osiko, V.V. Disorder of stoichiometry in lithium niobate crystals. *Cryst. Rep.* **1994**, *39*, 471–476.

102. Fay, H.; Alford, W.J.; Dess, H.M. Temperature in $LiNbO_3$ Crystals on Melt Composition. *Appl. Phys. Lett.* **1968**, *12*, 89. [CrossRef]

103. Suzuki, T. Oxygen partial pressure dependence of optical absorption in lithium niobate. *J. Cryst. Growth* **1996**, *163*, 403–410. [CrossRef]

104. Sweeney, K.L.; Halliburton, L.E.; Bryan, D.A.; Rice, R.R.; Gerson, R.; Tomaschke, H.E. Point defects in Mg-doped lithium niobate. *J. Appl. Phys.* **1985**, *57*, 1036–1044. [CrossRef]

105. Erdei, S.; Ainger, F.W. Trends in the growth of stoichiometric single crystals. *J. Cryst. Growth* **1997**, *174*, 293–300. [CrossRef]

106. Kovács, L.; Wohlecke, M.; Jovanović, A.; Polgár, K.; Kapphan, S. Infrared absorption study of the OH vibrational band in $LiNbO_3$ crystals. *J. Phys. Chem. Solids* **1991**, *52*, 797–803. [CrossRef]

107. Engelsberg, M.; de Souza, R.E.; Pacobahyba, L.H.; do Nascimento, G.C. Structural determination of hydrogen site occupation in proton-exchanged $LiNbO_3$ by nuclear magnetic resonance. *Appl. Phys. Lett.* **1995**, *67*, 359–361. [CrossRef]

108. Yevdokimov, S.V.; Yatsenko, A.V. Investigation of the Localization of H^+ Ions in Stoichiometric $LiNbO_3$. *Crystallogr. Rep.* **2003**, *48*, 542–546. [CrossRef]

109. Rakitina, L.G.; Zaritskii, I.M.; Polgar, K. New hydrogen associated paramagnetic centre in $LiNbO_3$. *Appl. Magn. Reson.* **1990**, *1*, 149–154. [CrossRef]

110. Rosa, J.; Polak, K.; Kubatova, J. ESR and optical studies of impurity centres in γ- and X-irradiated $LiNbO_3$. *Phys. Status Solidi (b)* **1982**, *111*, K85–K87. [CrossRef]

111. Corradi, G.; Polgar, K.; Bugai, A.A.; Grachev, V.G.; Deryugina, N.I.; Rakitina, L.M.; Zaritskii, I.M. Models of Ni^+ and Cu^{2+} impurity centers in $LiNbO_3$. *Sov. Phys. Solid State* **1986**, *28*, 739–748.

112. Zhang, H.-M.; Xiao, W.-B. Investigations on the EPR parameters and defect structures due to Jahn-Teller effect for the Cu^{2+} and Ni^+ centers in $LiNbO_3$. *J. Alloys Compd.* **2018**, *745*, 586–591. [CrossRef]

113. Zaritskii, I.M.; Rakitina, L.G.; Polgar, K. Annealing and gamma irradiation effects on the ESR in $LiNbO_3$:Mg crystals. *Sov. Phys. State Solid* **1995**, *37*, 1073–1978.

114. Faust, B.; Müller, H.; Schirmer, O.F. Free small polarons in $LiNbO_3$. *Ferroelectrics* **1994**, *153*, 297–302. [CrossRef]

115. Mirzakhanyan, A.A.; Petrosyan, A.K. EPR and optical absorption of Co^{2+} impurity ions in single crystal α-$LiIO_3$ and $LiNbO_3$. *Sov. Phys. Solid State* **1986**, *904–906*, 1593–1595.

116. Donnerberg, H.J.; Shirmer, O.F. The paramagnetic properties of Co^{2+} in $LiNbO_3$ and $LiTaO_3$. *Solid State Commun.* **1987**, *63*, 29–32. [CrossRef]

117. Choi, Y.N.; Park, I.-W.; Kim, S.S.; Park, S.S.; Choh, S.H. Electron paramagnetic resonance studies of Co^{2+} ions in congruent and nearly stoichiometric $LiNbO_3$ single crystals. *J. Phys. Condens. Matter* **1999**, *11*, 4723–4730. [CrossRef]

118. Grachev, V.G.; Hansen, K.; Meyer, M.; Kokanyan, E.P.; Malovichko, G.I. Substitution mechanisms and location of Co^{2+} ions in congruent and stoichiometric lithium niobate crystals derived from electron paramagnetic resonance data. *Mater. Res. Express* **2017**, *4*, 036204. [CrossRef]

119. Paul, M.; Tabuchi, M.; Weast, A.R. Defect Structure of Ni, Co-doped $LiNbO_3$ and $LiTaO_3$. *Chem. Mater.* **1997**, *9*, 3206–3214. [CrossRef]

120. Mei, Y.; Wu, X.-X.; Zheng, W.-C. EPR parameters and defect structures for the Co^{2+} ions in $LiNbO_3$ and $LiTaO_3$ crystals. *Spectrochim. Acta Part A Mol. Biomol. Spectrosc.* **2008**, *71*, 714–719. [CrossRef]

121. Wu, S.-Y.; Lu, G.D.; Zhang, Z.H.; Wei, L.H.; Hu, Y.-X. Theoretical investigations of the local structures and spin Hamiltonian parameters for the trigonal Co^{2+} centers in $LiNbO_3$ and $LiTaO_3$. *J. Alloys Compd.* **2009**, *1–2*, 1–5. [CrossRef]

122. Setser, G.G. An Investigation by Electron Paramagnetic Resonance of the Jahn-Teller Effect in $LiNbO_3:Ni^{3+}$ and $LiNbO_3:Cu^{2+}$. Ph.D. Thesis, Rice University, Houston, TX, USA, 1974; pp. 1–237.

123. Palatnikov, M.N.; Sidorov, N.V.; Skiba, V.I.; Biryukova, I.V.; Serebryakov, Y.A.; Kravchenko, O.E.; Balabanov, Y.I.; Kalinnikov, V.T. Effects of nonstoichiometry and doping on the curie temperature and defect structure of lithium niobate. *Inorg. Mater.* **2000**, *36*, 489–493. [CrossRef]

124. Pape, M.; Reyher, H.-J.; Schirmer, O.F. Optically detected magnetic resonance of Cu, Fe and Mn defects in $LiNbO_3$. *J. Phys. Condens. Matter* **2005**, *17*, 6835–6847. [CrossRef]

125. Mirzakhanyan, A.A. Zero-field splitting of energy levels of Ni^{2+} ground state in α-$LiIO_3$ and $LiNbO_3$. *Sov. Phys. State Solid* **1981**, *23*, 2452.

126. Khalil, A.; Masaif, N.; Jennane, A.; Maaider, K. Substitution Mechanism of $Ni:LiTaO_3$. *J. Mater. Environ. Sci.* **2011**, *2*, 196–200.

127. Yang, Z.Y.; Rudowicz, C.; Yeung, Y.Y. Microscopic spin-Hamiltonian parameters and crystal field energy levels for the low C_3 symmetry Ni^{2+} centre in $LiNbO_3$ crystals. *Physica B* **2004**, *348*, 151–159. [CrossRef]

128. Petrov, M.P. Spectrum of Electron Paramagnetic Resonance of Mn^{2+} in ferroelectric $LiNbO_3$. *Sov. Phys. Solid State* **1968**, *10*, 2574.

129. Takeda, T.; Watanabe, A.; Sugihara, K. Spacing of the hyperfine sextet in Mn^{2+} ESR in $LiNbO_3$. *Phys. Lett. A* **1968**, *27*, 114–115. [CrossRef]

130. Danner, J.C.; Ranon, U.; Stamires, D.N. ESR of Mn^{2+} in ferroelectric $LiTaO_3$ and $LiNbO_3$ single crystals. *Chem. Phys. Lett.* **1968**, *2*, 605–606. [CrossRef]

131. Herrington, J.B.; Dischler, B.; Schneider, J. An EPR investigation of Fe^{3+} and Mn^{2+} in $LiNbO_3$. *Solid State Commun.* **1972**, *10*, 509–511. [CrossRef]

132. Rexford, D.J.; Kim, Y.M. Electron-Spin Resonance Studies of Crystal Field Parameters in $Mn^{2+}:LiNbO_3$. *J. Chem. Phys.* **1972**, *57*, 3094–3098. [CrossRef]

133. Malovichko, G.I.; Grachev, V.G. Use of nuclear quadrupole splitting in determination of positions of iron group impurities in ferroelectric $LiNbO_3$. *Sov. Phys. Solid. State* **1985**, *27*, 1678–1679.

134. Malovichko, G.I.; Grachev, V.G.; Lukin, S.N. EPR of axial and low symmetry Cr^{3+}, Fe^{3+}, and Mn^{2+} centers in $LiNbO_3$. *Sov. Phys. Solid State* **1986**, *28*, 553–557.

135. Malovichko, G.I.; Karmazin, A.A.; Bykov, I.P.; Laguta, V.V.; Yarunichev, V.P. Electron spin resonance investigation of the temperature dependence of the axial crystal field parameters in Mn^{2+} and Cr^{3+} doped $LiNbO_3$. *Sov. Phys. Solid State* **1983**, *25*, 2038–2041.

136. Park, I.W.; Choh, S.H.; Song, K.J. The hyperfine structure of Mn^{2+} in $LiNbO_3$ and the sign of the second-order axial zero-field splitting. *J. Korean Phys. Soc.* **1993**, *26*, 77–80.

137. Park, I.-W. Three-fold Symmetry Effect on Mn^{2+} Centers in a $LiNbO_3$ Crystal. *J. Korean Magn. Res. Soc.* **2008**, *12*, 103–110. [CrossRef]

138. Yeom, T.H.; Lee, S.H. Temperature Dependence of Mn^{2+} Paramagnetic Ion in a Stoichiometric $LiNbO_3$ Single Crystal. *J. Magn.* **2013**, *18*, 221–224. [CrossRef]

139. Corradi, G.; Söthe, H.; Spaeth, J.-M.; Polgar, K. Mn^{2+} defects in $LiNbO_3$: An electron nuclear double resonance (ENDOR) investigation of the Mn^{2+} site and the local disorder. *J. Phys. Condens. Matter.* **1990**, *2*, 6603–6618. [CrossRef]

140. Malovichko, G.; Grachev, V.; Hofstaetter, A.; Kokanyan, E.; Scharmann, A.; Schirmer, O. ENDOR study of Cr^{3+} centers substituting for lithium in lithium niobate. *Phys. Rev. B* **2002**, *65*, 224116. [CrossRef]

141. Grachev, V.; Malovichko, G. EPR, ENDOR, and optical-absorption study of Cr^{3+} centers substituting for niobium in Li-rich lithium niobate crystals. *Phys. Rev. B* **2000**, *62*, 7779–7790. [CrossRef]

142. Grachev, V.; Malovichko, G.; Schirmer, O. Structures of point defects in lithium niobate. *Ukr. J. Phys.* **2004**, *49*, 438–448.

143. Evlanova, N.F.; Kornienko, L.S.; Rashkovich, L.N.; Rybaltovskii, A.O. EPR of some rare-earth ions and Cr^{3+} in $LiNbO_3$. *Sov. JETP* **1967**, *53*, 1920–1926.

144. Burns, G.; O'Kane, D.F.; Title, R.S. Optical and Electron-Spin-Resonance Spectra of **Yb^{3+}**, **Nd^{3+}**, and **Cr^{3+}** in $LiNbO_3$ and $LiTaO_3$. *Phys. Rev.* **1968**, *167*, 314–318. [CrossRef]

145. Rexford, D.J.; Kim, Y.M.; Story, H.S. Electron-Spin resonance studies of Cr^{3+} in $LiNbO_3$. *J. Chem. Phys.* **1970**, *52*, 860–863. [CrossRef]

146. Choh, S.H.; Kim, H.T.; Choh, H.K.; Han, C.S.; Choi, D.; Kim, J.N. Characterization of Stoichiometry of $LiNbO_3$ Crystals by EPR and Raman Scattering Measurements. *Bull. Magn. Res.* **1989**, *11*, 371.

147. Salley, G.M.; Basun, S.A.; Imbusch, G.F.; Kaplyanskii, A.A.; Kapphan, S.; Meltzer, R.S.; Happek, U. Chromium centers in $LiNbO_3$ revisited. *J. Luminescence* **1999**, *83–84*, 423–427. [CrossRef]

148. Grachev, V.; Malovichko, G.; Schirmer, O. Single, dimer and trimer chromium centers in lithium niobate. *Ferroelectrics* **1996**, *185*, 5–8. [CrossRef]

149. Grachev, V.G.; Malovichko, G.I.; Troitskii, V.V. Investigation of the charge compensation mechanisms of Cr^{3+} ions in $LiNbO_3$ by EPR and ENDOR methods. *Sov. Phys. Solid State* **1987**, *29*, 349–350.

150. Siu, G.G.; Zhao, M.-G. Electron-spin-resonance studies of Cr-ion pairs in $LiNbO_3$: Cr^{3+}. *Phys. Rev. B* **1991**, *43*, 13575–13578. [CrossRef] [PubMed]

151. Corradi, G.; Sothe, H.; Spaeth, J.-M.; Polgar, K. Electron spin resonance and electron-nuclear double-resonance investigation of a new Cr^{3+} defect on an Nb site in $LiNbO_3$:Mg:Cr. *J. Phys. Condens. Matter* **1991**, *3*, 1901–1908. [CrossRef]

152. Corradi, G.; Sothe, H.; Spaeth, J.-M.; Polgar, K. ENDOR for characterizing transition metal centres in $LiNbO_3$. *Radiat. Eff. Defects Solids* **1991**, *119–121*, 583–587. [CrossRef]

153. Corradi, G.; Söthe, H.; Spaeth, J.-M.; Polgar, K. Local environment of Mn^{2+} and Cr^{3+} centres in $LiNbO_3$: Discussion of recent ENDOR results. *Ferroelectrics* **1992**, *125*, 295–299. [CrossRef]

154. Diazcaro, J.; Garcia-Sole, J.; Bravo, D.; Han, T.P.J.; Jaque, F.; Henderson, B. EPR and infrared absorption study in MgO Co-Doped $LiNbO_3$ crystals. *Ferroelectr. Lett. Sect.* **1997**, *23*, 27–35. [CrossRef]

155. Thiemann, O.; Corradi, G.; Reyher, H.-J. ODMR-investigations of transition metals in $LiNbO_3$. *Ferroelectrics* **1992**, *125*, 283–288. [CrossRef]

156. Camarillo, E.; Garcia-Sole, J.; Cusso, F.; Agullo-Lopez, F.; Sanz-Garcia, J.A.; Han, T.P.J.; Jaque, F.H.; Henderson, B. Polarization spectroscopy of Cr^{3+} ions in $LiNbO_3$ single crystals: Effect of Mg^{2+} ions. *Chem. Phys. Lett.* **1991**, *185*, 505–510. [CrossRef]

157. Camarillo, E.; Tocho, J.; Vergara, I.; Dieguez, E.; Garcia-Sole, J.; Jaque, F. Optical bands of Cr^{3+} induced by Mg^{2+} ions in $LiNbO_3$:Cr,Mg. *Phys. Rev. B* **1992**, *45*, 4600–4604. [CrossRef]

158. Martin, A.; Lopez, F.J.; Agullo-Lopez, F. Cr^{3+} in pure and Mg-doped $LiNbO_3$: Analysis of the EPR and optical spectra. *J. Phys. Condens. Matter* **1992**, *4*, 847–853. [CrossRef]

159. Macfarlane, P.I.; Holliday, K.; Nicholls, J.F.H.; Henderson, B. Characterization of Cr^{3+} centres in $LiNbO_3$ using fluorescence line narrowing. *J. Phys. Condens. Matter.* **1995**, *7*, 9643–9656. [CrossRef]

160. Diaz-Caro, J.; Garcia-Sole, J.; Bravo, D.; Sanz-Garcia, J.A.; Lopez, F.J.; Jaque, F. MgO codoping-induced change in the site distribution of Cr^{3+} ions in $LiNbO_3$. *Phys. Rev. B* **1996**, *54*, 13042–13046. [CrossRef] [PubMed]

161. Diaz-Caro, J.; Garcia-Sole, J.; Martinez, J.L.; Henderson, B.; Jaque, F.; Han, T.P.J. Redistribution of Cr^{3+} defect centres in $LiNbO_3$ crystals: The MgO effect. *Opt. Mater.* **1998**, *10*, 69–77. [CrossRef]

162. Torchia, G.A.; Martinez Matos, O.; Vaveliuk, P.; Tocho, J.O. Influence of the electron-lattice coupling for Cr^{3+} ions in Nb^{5+} site into congruent co-doped $LiNbO_3$: Cr^{3+}: ZnO crystal. *Solid State Commun.* **2003**, *127*, 535–539. [CrossRef]

163. Ahn, S.W.; Rudowicz, C.; Choh, S.H.; Han, S.Y. EPR study of two Cr^{3+} defect centers in $LiTaO_3$ single crystals. *J. Korean Phys. Soc.* **1997**, *30*, 99–102.

164. Ahn, S.W.; Kim, J.S.; Choh, S.H.; Yeom, T.H. An Induced Cr^{3+} Center in gamma-Irradiated $LiTaO_3$. *J. Korean Phys. Soc.* **1994**, *27*, 535–538.

165. Loyo-Menoyo, M.; Keeble, D.J.; Furukawa, Y.; Kitamura, K. Electron paramagnetic resonance of Cr^{3+} in near-stoichiometric $LiTaO_3$. *J. Appl. Phys.* **2005**, *97*, 123905. [CrossRef]

166. Bourson, P.; Malovichko, G.; Ridah, A.; Kokanyan, E. Effect of chromium concentration on site selective luminescence in nearly stoichiometric lithium niobate crystals. *Ferroelectrics* **1996**, *155*, 273–276. [CrossRef]

167. Lhomme, F.; Bourson, P.; Fontana, M.D.; Malovichko, G.; Aillerie, M.; Kokanyan, E. Luminescence of Cr^{3+} in lithium niobate: Influence of the chromium concentration and crystal composition. *J. Phys. Condens. Matter* **1998**, *10*, 1137–1146. [CrossRef]

168. Lhomme, F.; Bourson, P.; Moncorge, R.; Burlot, R.; Fontana, M.D.; Aillerie, M.; Boulon, G.; Malovichko, G. New study of the 720–750 nm range in the emission spectra of $LiNbO_3$:Cr^{3+} crystals with different compositions. *Radiat. Eff. Defects Solids* **1999**, *150*, 259–263. [CrossRef]

169. Kaminska, A.; Suchocki, A.; Grinberg, M.; Garcia-Sole, J.; Jaque, F.; Arizmendi, L. High-pressure spectroscopy of $LiNbO_3$:MgO, Cr^{3+} crystals. *J. Lumin.* **2000**, *87–89*, 571–573. [CrossRef]

170. Salley, G.M.; Basun, S.A.; Kaplyanskii, A.A.; Meltzer, R.S.; Polgar, K.; Happek, U. Chromium centers in stoichiometric $LiNbO_3$. *J. Lumin* **2000**, *87–89*, 1133–1135. [CrossRef]

171. Dierolf, V.; Kaplyanskii, A.A.; Kapphan, S.; Kutsenko, A.B. The fine structure of spectral response of Cr^{3+} sites in $LiNbO_3$. In *Radiat. Eff. Defects Solids*; 2001; Volume 155, pp. 241–246. [CrossRef]

172. Basun, S.A.; Salley, G.M.; Kaplyanskii, A.A.; Gallagher, H.G.; Polgar, K.; Lu, L.; Happek, U. A novel luminescent center in $LiNbO_3$:Cr:Mg crystals. *J. Lumin.* **1999**, *83–84*, 435–439. [CrossRef]

173. Lhomme, F.; Bourson, P.; Boulon, G.; Guyot, Y.; Fontana, M.D. Comparative analysis of the Cr^{3+} centre spectroscopic properties in $LiNbO_3$ crystals from congruent to nearly stoichiometric compositions. *Eur. Phys. J. AP* **2002**, *20*, 29–40. [CrossRef]

174. Han, T.P.J.; Jaque, F.; Bermudez, V.; Dieguez, E. Luminescence of the Cr^{3+} R-lines in pure and MgO co-doped near stoichiometric $LiNbO_3$:Cr crystals. *Chem. Phys. Lett.* **2003**, *369*, 519–524. [CrossRef]

175. Han, T.P.J.; Jaque, F. Optical stability of the Cr^{3+} centres in codoped stoichiometric and congruent $LiNbO_3$:Cr:Mg. *Opt. Mater.* **2007**, *29*, 1041–1043. [CrossRef]

176. Kaczmarek, S.M.; Lukasiewicz, T.; Pracka, I.; Jablonski, R.; Boulon, G.; Kaczmarek, B.; Warchol, S. Radiation defects in Dy^{3+} doped $LiNbO_3$ single crystals. *J. Alloys Compd.* **1998**, *275–277*, 105–108. [CrossRef]

177. Jablonski, R.; Pracka, I.; Swirkowicz, M. Electron spin resonance spectra of Nd^{3+}, Dy^{3+}, Er^{3+} and Yb^{3+} in $LiNbO_3$. In *Solid State Crystals: Growth and Characterization, Proceedings of the XII Conference on Solid State Crystals: Materials Science and Applications, Zakopane, Poland, 7–11 October 1996*; SPIE: Bellingham, WA, USA, 1997. [CrossRef]

178. Milori, D.M.B.P.; Moraes, I.J.; Hernandes, A.C.; de Souza, R.R.; Li, M.S.; Terrile, M.C.; Barberis, G.E. Optical and ESR study of Er^{3+} in $LiNbO_3$. *Phys. Rev. B* **1995**, *51*, 3206—3209. [CrossRef] [PubMed]

179. Nolte, T.; Pawlik, T.; Spaeth, J.-M. EPR study of Er^{3+} in congruent $LiNbO_3$. *Solid State Commun.* **1997**, *104*, 535–539. [CrossRef]

180. Bodziony, T.; Kaczmarek, S.M. EPR study of low symmetry Er centers in congruent lithium niobate. *Phys. Status Solidi (b)* **2008**, *245*, 998–1002. [CrossRef]

181. Kaczmarek, S.M.; Bodziony, T. Low symmetry centers in $LiNbO_3$ doped with Yb and Er. *J. Non-Cryst. Solids* **2008**, *354*, 4202–4210. [CrossRef]

182. Bodziony, T.; Kaczmarek, S.M. Temperature dependence of the EPR spectra and optical measurements of $LiNbO_3$: Er, Tm single crystal. *J. Alloys Compd.* **2009**, *468*, 581–585. [CrossRef]

183. Bodziony, T.; Kaczmarek, S.M.; Kruk, R. Low temperature magnetic measurements of $LiNbO_3$ single crystal weakly doped with Er and codoped with Tm ions. *J. Spectrosc. Dyn.* **2011**, *1*, 1–8.

184. Vrable, I.; Malovichko, G.; Grachev, V.; Meyer, M. EPR/ENDOR Studies of Erbium Centers in Stoichiometric Lithium Niobate Crystals. In Proceedings of the 49th Rocky Mountain Conference on Analytical Chemistry, Breckenridge, CO, USA, 22–26 July 2007; Abstract C 143. p. 71. Available online: http://rockychem.com/links/past-conferences.html (accessed on 1 March 2007).

185. Malovichko, G.; Grachev, V.; Jorgensen, J.; Meyer, M.; Munro, M.; Todt, B.; Vrable, I.; Kokanyan, E.; Bratus, V.; Okulov, S. Magnetic resonance study of non-equivalent centers created by 4f-ions in congruent and stoichiometric lithium niobate. *MRS Online Proc. Libr.* **2008**, *1111*, 103. [CrossRef]

186. Mackova, A.; Groetzschel, R.; Eichhorn, F.; Nekvindova, P.; Spirkova, J. Characterization of Er:$LiNbO_3$ and APE:Er:$LiNbO_3$ by RBS–channeling and XRD techniques. *Surf. Interface Anal.* **2004**, *36*, 949–951. [CrossRef]

187. Gog, T.; Griebenow, M.; Materlik, G. X-ray standing wave determination of the lattice location of Er diffused into $LiNbO_3$. *Phys. Lett. A* **1993**, *181*, 417–420. [CrossRef]

188. Rebouta, L.; da Silva, M.F.; Soares, J.C.; Serrano, D.; Diéguez, E.; Agulló-López, F.; Tornero, J. Nonaxial sites for Er in $LiNbO_3$. *J. Appl. Phys. Lett.* **1997**, *70*, 1070–1072. [CrossRef]

189. Malovichko, G.; Vrable, I.; Meyer, M.; Kokanyan, E.; Grachev, V. Ordering magnetic moments of Er^{3+} in ferroelectric lithium niobate. In Proceedings of the International Conference "Oxide Materials for Electronic Engineering—Fabrication, Properties and applica$tion" (OMEE-2014), Lviv, Ukraine, 26–30 May 2014; pp. 35–36.

190. Gill, D.M.; Wright, J.C.; McCaughan, L. Site characterization of rare-earth-doped $LiNbO_3$ using total site selective spectroscopy. *J. Appl. Phys. Lett.* **1994**, *64*, 2483–2485. [CrossRef]

191. Gill, D.M.; McCaughan, L.; Wright, J.C. Spectroscopic site determinations in erbium-doped lithium niobate. *Phys. Rev. B* **1996**, *53*, 2334–2344. [CrossRef] [PubMed]

192. Muntoz, J.A.; Cantelar, E.; Sanz-garcia, J.A.; Duchowicz, R.; Serrano, D.; Dieguez, E.; Lifante, G.; Cusso, F. Site-selective spectroscopy of Er^{3+} and Er^{3+} Yb^{3+} doped stoichiometric and congruent lithium niobate. *Radiat. Eff. Defects Solids* **1999**, *150*, 221–225. [CrossRef]

193. Dierolf, V.; Koerdt, M. Combined excitation-emission spectroscopy of Er^{3+} ions in stoichiometric $LiNbO_3$: The site selectivity of direct and up conversion excitation processes. *Phys. Rev. B* **2000**, *61*, 8043–8048. [CrossRef]

194. Dierolf, V.; Kutsenko, A.B.; Ostendorf, A.; von der Osten, W.; Sohler, W.; Suche, H. Site-selective spectroscopy of Er^{3+}:Ti:$LiNbO_3$ waveguides. *Appl. Phys. B* **2001**, *72*, 803–810. [CrossRef]

195. Dierolf, V.; Kutsenko, A.B.; Sandmann, C.; Troester, T.; Corradi, G. High-resolution site selective optical spectroscopy of rare earth and transition metal defects in insulators. *J. Lumin.* **2000**, *87–89*, 989–991. [CrossRef]

196. Dierolf, V.; Sandmann, C. Combined excitation emission spectroscopy of defects for site-selective probing of ferroelectric domain inversion in lithium niobate. *J. Lumin.* **2007**, *125*, 67–79. [CrossRef]

197. Bravo, D.; Martin, A.; Lopez, F.J. A new centre of Er^{3+} in MgO or ZnO co-doped $LiNbO_3$ single crystals. *Solid State Commun.* **1999**, *112*, 541–544. [CrossRef]

198. Mehran, F.; Scott, B.A. Electron paramagnetic resonance of $LiNbO_3$: Fe^{3+}. *Solid State Commun.* **1972**, *11*, 15–19. [CrossRef]

199. Towner, H.H.; Kim, Y.M.; Story, H.S. EPR studies of crystal field parameters in Fe^{3+}: $LiNbO_3$. *J. Chem. Phys.* **1972**, *56*, 3676–3679. [CrossRef]

200. Dikantova, Z. EPR study of impurities centers in $LiNbO_3$. *Acta Phys. Slov.* **1973**, *23*, 245–250.

201. Keune, W.; Date, S.K.; Gonser, U.; Bunzel, H. Mossbauer effect study of Fe^{57} doped $LiNbO_3$ and $LiTaO_3$. *Ferroelectrics* **1976**, *13*, 443–445. [CrossRef]

202. Kurz, H.; Krätzig, E.; Keune, W.; Engelmann, H.; Gonser, U.; Dischler, B.; Räuber, A. Photorefractive centers in $LiNbO_3$, studied by optical-, Mössbauer- and EPR-methods. *Appl. Phys.* **1977**, *12*, 355–368. [CrossRef]

203. Grachev, V.G.; Malovichko, G.I. Determination of the point symmetry of defects in crystals exhibiting structural phase transitions, using the temperature dependencies of the EPR spectra. Impurities in $LiNbO_3$. *Sov. Phys. Solid State* **1985**, *27*, 686–689.

204. Pfannes, H.D.; Putzka, A.; Sampaio, J.F. Electronic structure and spin relaxation of Fe(III) in $LiNbO_3$. *Hyperfine Interact.* **1986**, *28*, 785–788. [CrossRef]

205. Jablonski, R.; Kaczmarek, S.M.; Praska, I.; Surma, B.; Swirkowicz, M.; Lukasiewicz, T. ESR and optical measurements of $LiNbO_3$ and $LiTaO_3$ single crystals doped with ions of the first transition series. *Spectrochim. Acta A* **1998**, *54*, 1701–1709. [CrossRef]

206. Yeom, T.H.; Choh, S.H. Magnetic Resonance Investigations of $LiNbO_3$ and $LiTaO_3$ Single Crystals. *J. Korea Phys. Soc.* **1998**, *32*, S672–S674.

207. Santana, R.C.; Terrile, M.C.; Hernandes, A.C.; Andreeta, M.R.B.; Barberis, G.E. Electron spin resonance study of Fe^{3+} in $LiNbO_3$ single crystals: Bulk and fibres. *Solid State Commun.* **1997**, *103*, 61–64. [CrossRef]

208. Keeble, D.J.; Loyo-Menoyo, M.; Furukawa, Y.; Kitamura, K. Electron paramagnetic resonance of **Fe^{3+}** in **$LiNbO_3$**. *Phys. Rev. B* **2005**, *71*, 224111. [CrossRef]

209. Agullò-López, F.; Müller, K.A. Superposition Model Calculations for Fe^{3+} in $LiNbO_3$. *Cryst. Latt. Def. Amorph. Mater.* **1987**, *15*, 89.

210. Zhao, M.G.; Chiu, M. Substitution site of the Fe^{3+} impurity in crystalline $LiNbO_3$. *Phys. Rev. B* **1994**, *49*, 12556–12558. [CrossRef]

211. Wang, H.; Kuang, X.Y.; Die, D.; Tan, X.-M.; Yang, X. EPR spectra and local lattice structure of Fe^{3+} impurity ions in ferroelectric $LiNbO_3$. *Chem. Phys.* **2006**, *330*, 212–215. [CrossRef]

212. Wang, H.; Kuang, X.Y.; Die, D.; Yang, X.; Zhou, K.-W. EPR investigation of substitution position for Fe^{3+} in $LiNbO_3:Fe^{3+}$ system. *Physica B* **2005**, *367*, 53–60. [CrossRef]

213. Yeom, T.H.; Chang, Y.M.; Choh, S.H.; Rudowicz, C. Experimental and Theoretical Investigation of Spin-Hamiltonian Parameters for the Low Symmetry Fe^{3+} Centre in $LiNbO_3$. *Phys. Status Solidi (b)* **1994**, *185*, 409–415. [CrossRef]

214. Xue, D.; He, X. Dopant occupancy and structural stability of doped lithium niobate crystals. *Phys. Rev. B* **2006**, *73*, 064113. [CrossRef]

215. Zhang, Z.; Xue, D. Local Lattice Structure and Dopant Occupancy Of Doped Lithium Niobate Crystals. *Mod. Phys. Lett. B* **2009**, *23*, 3687–3694. [CrossRef]

216. Basun, S.A.; Bursian, V.E.; Evans, D.R.; Kaplyanskii, A.A.; Razdobarin, A.G.; Sochava, L.S. Ferroelectric-Specific Stark Effect in Stoichiometric $LiNbO_3:Fe$ at Room Temperature. *Phys. Rev. Lett.* **2008**, *100*, 057602. [CrossRef]

217. Grachev, V.G.; Petersen, R.T.; Kokanyan, E.P.; Schirmer, O.F.; Malovichko, G.I. Structural analysis of the dominant axial Fe^{3+} center in $LiNbO_3$ crystal by electron nuclear double resonance. *J. Appl. Phys.* **2016**, *120*, 193901. [CrossRef]

218. Boker, A.; Donnerberg, H.; Schirmer, O.F.; Feng, X. Two sites of Fe^{3+} in highly Mg-doped $LiNBO_3$. *J. Phys. Condens. Matter* **1990**, *2*, 6865–6868. [CrossRef]

219. Volk, T.R.; Rubinina, N.M.; Pryalkin, V.I.; Krasnikov, V.V.; Volkov, V.V. Optical and non-linear optical investigations in $LiNbO_3:Mg$ and $LiNbO_3:Zn$. *Ferroelectrics* **1990**, *109*, 345–350. [CrossRef]

220. Yeom, T.H.; Lee, S.H.; Choh, S.H.; Choi, D. Electron paramagnetic resonance study of Fe^{3+} in $LiNbO_3:Mg:Fe$ crystal. *J. Korean Phys. Soc.* **1998**, *32*, S647.

221. Malovichko, G.I.; Grachov, V.G.; Kokanyan, E.P. Low-symmetry Fe-Mg complexes in $LiNbO_3:Mg$. *Ferroelectrics* **1992**, *125*, 289–294. [CrossRef]

222. Grachev, V.; Malovichko, G.; Kokanyan, E. Optimization of lithium niobate for advanced applications by variation of extrinsic and intrinsic defect subsystems. *Ferroelectrics* **2001**, *258*, 131–140. [CrossRef]

223. Volk, T.; Wöhlecke, M.; Rubinina, N.; Razumovskii, N.V.; Jermann, F.; Fischer, C.; Böwer, R. $LiNbO_3$ with the damage-resistant impurity indium. *Appl. Phys. A* **1995**, *60*, 217–225. [CrossRef]

224. Volk, T.R.; Rubinina, N.M. Non photorefractive impurities in lithium niobate: Magnesium and zinc. *Sov. Phys. Solid State* **1991**, *33*, 674–680.

225. Vazhenin, V.A.; Guseva, V.B.; Artyomov, M.Y.; Route, R.K.; Fejer, M.M.; Byer, R.L. Fine structure of the electron paramagnetic resonance spectrum of Fe^{3+} centres in $LiTaO_3$. *J. Phys. Condens. Matter* **2003**, *15*, 275–280. [CrossRef]

226. Loyo-Menoyo, M.; Keeble, D.J.; Furukawa, Y.; Kitamura, K. Electron paramagnetic resonance of Fe^{3+} in near-stoichiometric $LiTaO_3$. *J. Phys. Condens. Matter* **2004**, *16*, 9047–9057. [CrossRef]

227. McDonald, P.F.; Tam, C.P.; Mok, Y.W. EPR Gd^{3+} in $LiNbO_3$. *J. Chem. Phys.* **1972**, *56*, 1007–1008. [CrossRef]

228. Dischler, B.; Herrington, J.R.; Räuber, A.; Schneider, J.; Urban, W. An EPR study of different Gd^{3+} centers in $LiNbO_3$. *Solid State Communs.* **1973**, *12*, 737–740. [CrossRef]

229. Park, I.-W.; Kim, M.; Choh, S.H.; Kim, J.N. EPR study of Gd^{3+} Paramagnetic Centers in Congruent $LiNbO_3$ Single Crystal. *New Phys. (Korean Phys. Soc.)* **1994**, *34*, 464–469.

230. Bonardi, C.; Carvalho, R.A.; Basso, H.C.; Terrile, M.C.; Cruz, G.K.; Bausa, L.E.; Sole, J.G. Magnetic circular dichroism of Nd^{3+} and Yb^{3+} ions in $LiNbO_3$ crystals. *J. Chem. Phys.* **1999**, *111*, 6042–6046. [CrossRef]

231. Camarillo, E.; Hernandez, J.; Garcia Sole, J.; Caldino, U.; Munoz Santiuste, J.E.; Loro, H.; Voda, M.; Jaque, F.; Murrieta, H. Nd^{3+} centres induced by ZnO or MgO codoping $LiNbO_3$. *J. Phys. Condens. Matter* **1995**, *7*, 96359641. [CrossRef]

232. Ziling, K.K.; Nadolinnii, V.A.; Shashkin, V.V. *Sov.:* Reports of AS of USSR. *Inorg. Mater.* **1980**, *16*, 701.

233. Juppe, S.; Schirmer, O.F. EPR Ti^{3+} in $LiNbO_3$. *Phys. Lett. A* **1986**, *117*, 150–155. [CrossRef]

234. Rakitina, L.G.; Zaritskii, I.M.; Corradi, G.; Polgar, K. Mechanisms of broadening of ESR lines of polaron centers in $LiNbO_3$: Ti subjected to irradiation and heat treatments. *Sov. Phys. Solid State* **1990**, *32*, 654–660.

235. Thiemann, O.; Donnerberg, G.H.; Wöhlecke, M.; Schirmer, O. Vibronic structure, energy level, and incorporation mechanism of Ti^{3+} in $LiNbO_3$ and $LiTaO_3$. *Phys. Rev. B* **1994**, *49*, 5845–5851. [CrossRef]

236. Corradi, G.; Polgar, K.; Zaritskii, I.M.; Rakitina, L.G.; Deryugina, N.I. Defect formation under γ-irradiation and heat treatment in pure and doped LiNbO₃ monocrystals. *Sov. Phys. State Solid* **1989**, *31*, 115–122.

237. Corradi, G.; Zaritskii, I.M.; Hofstaetter, A.; Polgar, K.; Rakitina, L.G. Ti³⁺ on Nb site: A paramagnetic Jahn-Teller center in vacuum-reduced LiNbO₃:Mg:Ti single crystals. *Phys. Rev. B* **1998**, *58*, 8329–8337. [CrossRef]

238. Corradi, G. Nb⁴⁺ Polaron and Ti³⁺ Shallow Donor Jahn-Teller Centers in LiNbO₃ Systems. In *Defects and Surface-Induced Effects in Advanced Perovskites*; Borstel, G., Krumins, A., Millers, D., Eds.; NATO Science Series (Series 3. High Technology); Springer: Dordrecht, The Netherlands; Boston, MA, USA; London, UK, 2000; Volume 77, pp. 89–100. [CrossRef]

239. Corradi, G.; Meyer, M.; Kovács, L.; Polgar, K. Gap levels of Ti³⁺ on Nb or Li sites in LiNbO₃:(Mg):Ti crystals and their effect on charge transfer processes. *Appl. Phys. B* **2004**, *78*, 607–614. [CrossRef]

240. Corradi, G.; Meyer, M.; Polgár, K. Bipolarons localised by Ti dopants in reduced LiNbO₃ crystals double-doped by Ti and Mg. *Phys. Status Solidi (c)* **2005**, *2*, 132–135. [CrossRef]

241. Bonardi, C.; Magon, C.J.; Vidoto, E.A.; Terrile, M.C.; Bausa, L.E.; Montoya, E.; Bravo, D.; Martin, A.; Lopez, F.J. EPR spectroscopy of Yb³⁺ in LiNbO₃ and Mg:LiNbO₃. *J. Alloys Compd.* **2001**, *323*, 340–343. [CrossRef]

242. Dohnke, I.; Trusch, B.; Klimm, D.; Hulliger, J. A study of influence of ytterbium and impurities on lattice parameters and phase transition temperature of Czochralski grown LiNbO₃. *J. Phys. Chem. Solids* **2004**, *65*, 1297–1305. [CrossRef]

243. Bodziony, T.; Kaczmarek, S.M. New low symmetry centres of Yb³⁺ impurities in lithium niobate single crystal. *Opt. Mater.* **2007**, *29*, 1440–1446. [CrossRef]

244. Bodziony, T.; Kaczmarek, S.M. EPR and optical study of coupled Yb³⁺ ion pairs in weakly doped LiNbO₃:Yb single crystal. *Res. Chem. Intermed.* **2007**, *33*, 885–899. [CrossRef]

245. Bodziony, T.; Kaczmarek, S.M.; Rudowicz, C. Temperature dependence of the EPR lines in weakly doped LiNbO₃:Yb—Possible evidence of Yb3+ ion pairs formation. *Physica B* **2008**, *403*, 207–218. [CrossRef]

246. Bodziony, T.; Kaczmarek, S.M.; Hanuza, J. EPR and optical studies of LiNbO₃:Yb and LiNbO₃:Yb, Pr single crystals. *J. Alloys Compd.* **2008**, *451*, 240–247. [CrossRef]

247. Bodziony, T.; Kaczmarek, S.M.; Kruk, R. Magnetic properties of LiNbO₃ single crystals weakly doped by Yb and/or codoped by Pr. *Rev. Adv. Mater. Sci.* **2010**, *23*, 1–7.

248. Malovichko, G.; Grachev, V.; Kokanyan, E.; Schirmer, O. EPR, NMR and ENDOR study of intrinsic and extrinsic defects in disordered and regularly ordered lithium niobate crystals. *Ferroelectrics* **2000**, *239*, 357–366. [CrossRef]

249. Malovichko, G.; Bratus, V.; Grachev, V.; Kokanyan, E. Electron paramagnetic resonance and electron-nuclear double resonance study of nonequivalent Yb³⁺ centers in congruent and nearly stoichiometric lithium niobate. *Phys. Status Solidi (b)* **2009**, *246*, 215–225. [CrossRef]

250. Xu, H.; Lee, D.; He, J.; Sinnott, S.B.; Gopalan, V.; Dierolf, V.; Phillpot, S.R. Stability of intrinsic defects and defect clusters in LiNbO₃ from density functional theory calculations. *Phys. Rev. B* **2008**, *78*, 174103. [CrossRef]

251. Xu, H.; Chernatynskiy, A.; Lee, D.; Sinnott, S.B.; Gopalan, V.; Dierolf, V.; Phillpot, S.R. Stability and charge transfer levels of extrinsic defects in LiNbO₃. *Phys. Rev. B* **2010**, *82*, 184109. [CrossRef]

252. Xu, H.; Lee, D.; Sinnott, S.B.; Dierolf, V.; Gopalan, V.; Phillpot, S.R. Structure and diffusion of intrinsic defect complexes in LiNbO₃ from density functional theory calculations. *J. Phys. Condens. Matter* **2010**, *22*, 135002. [CrossRef]

253. Vyalikh, A.; Zschornak, M.; Köhler, T.; Nentwich, M.; Weigel, T.; Hanzing, J.; Zaripov, R.; Vavilova, E.; Gemming, S.; Brendler, E.; et al. Analysis of the defect clusters in congruent lithium tantalate. *Phys. Rev. Mater.* **2018**, *2*, 013804. [CrossRef]

254. Zhang, Q.-R.; Feng, X.-Q. Defect structures and the MgO-doping-level-threshold effect on the optical absorption of reduced MgO-doped lithium niobate. *Phys. Rev. B* **1991**, *43*, 12019–12024. [CrossRef] [PubMed]

255. Schirmer, O.F.; Thiemann, O.; Wohlecke, M. Defects in LiNbO₃—I. experimental aspects. *J. Phys. Chem. Solids* **1991**, *52*, 185–200. [CrossRef]

256. Schirmer, O.F.; Imlau, M.; Merschjann, C.; Schoke, B. Electron small polarons and bipolarons in LiNbO₃. *J. Phys. Condens. Matter* **2009**, *21*, 123201. [CrossRef] [PubMed]

257. Schirmer, O.F.; von der Linde, D. Two photon and x-ray induced Nb⁴⁺ and O⁻ small polarons in LiNbO₃. *Appl. Phys. Lett.* **1978**, *33*, 35–38. [CrossRef]

258. Ketchum, J.L.; Sweeney, K.L.; Halliburton, L.E.; Armington, A.F. Vacuum annealing effects in lithium niobate. *Phys. Lett. A* **1983**, *94*, 450–453. [CrossRef]

259. Sweeney, K.L.; Halliburton, L.E. Oxygen vacancies in lithium niobate. *Appl. Phys. Lett.* **1983**, *43*, 336–338. [CrossRef]

260. Halliburton, L.E.; Sweeney, K.L.; Chen, C.Y. Electron spin resonance and optical studies of point defects in lithium niobate. *Nucl. Instrum. Methods Phys. Res. B* **1984**, *1*, 344–347. [CrossRef]

261. Dutt, D.A.; Feigl, F.J.; DeLeo, G.G. Optical absorption and electron paramagnetic resonance studies of chemically reduced congruent lithium niobate. *J. Phys. Chem. Solids* **1990**, *51*, 407–415. [CrossRef]

262. Müller, H.; Schirmer, O.F. Microscopic structure of Nb_Li related defects in reduced undoped LiNbO₃. *Ferroelectrics* **1992**, *125*, 319–324. [CrossRef]

263. Zaritskii, I.M.; Rakitina, L.G.; Corradi, G.; Polgar, K.; Bugai, A.A. A new trapped-hole radiation defect in heavily Mg-doped LiNbO₃. *J. Phys. Condens. Matter* **1991**, *3*, 8457–8465. [CrossRef]

264. Halliburton, L.E.; Sweeney, K.L.; Kappers, L.A. Self-trapped electrons in lithium tantalate. *Phys. Lett. A* **1986**, *116*, 81–84. [CrossRef]

265. Lee, M.; Gyoo Kim, I.; Takekawa, S.; Furukawa, Y.; Uchida, Y.; Kitamura, K.; Hatano, H. Electron paramagnetic resonance investigation of the photochromic effect in near-stoichiometric **LiNbO₃** with applications to holographic storage. *J. Appl. Phys.* **2001**, *89*, 5311. [CrossRef]
266. Miki, T.; Hantehzadeh, M.R.; Halliburton, L.E. A new trapped-hole center in irradiated LiNbO₃. *J. Phys. Chem. Solids* **1989**, *50*, 1003–1007. [CrossRef]